九州大学学術情報リポジトリ
Kyushu University Institutional Repository

TENSILE PROPERTIES OF NEWLY DESIGNED UNIDIRECTIONALLY ARRAYED CHOPPED STRANDS LAMINATES

李, 航

https://doi.org/10.15017/1441238

出版情報：九州大学, 2013, 博士（工学）, 課程博士
バージョン：
権利関係：全文ファイル公表済

Tensile Properties of Newly Designed Unidirectionally Arrayed Chopped Strands Laminates

by

HANG LI

A Dissertation Presented to

Department of Aeronautics and Astronautics
Graduate School of Engineering
Kyushu University

December 2013

ABSTRACT

In this dissertation, new designs of unidirectionally arrayed chopped strands (UACS) are proposed to improve existing UACS laminates with continuous angled slits by introducing discontinuous angled slits into a unidirectional prepreg. Two slit patterns of staggered angled slits and bi-angled slits are designed. A paper cutter is employed to introduce regular slits into the prepreg. Quasi-isotropic UACS laminates with new slit patterns and existing continuous angled slits together with the conventional carbon fiber reinforced polymer (CFRP) without slits are fabricated for tensile test. Tensile test results reveal that compared with existing UACS laminates, staggered and bi-angled UACS enhance the strength by about 10% and 15% respectively when the longitudinal modulus value present at the same level with conventional CFRP laminate. Additionally, flowability test results perform that newly designed UACS laminas possess better flowability than existing UACS laminate.

A multiscale damage progression analysis model based on the commercial finite element method (FEM) software is developed to investigate the damage progression in UACS laminates with different slit patterns. The multiscale analysis includes a homogenization analysis and a damage progression analysis of a microscopic region and a macroscopic region. The elastic constants of the laminas used in the macroscopic region are calculated by the homogenization analysis. Cohesive interface elements and maximum stress criterion are employed for the simulation of the progression of

delamination and other failure modes in the UACS laminates, respectively. Results of damage progression analysis indicate that discontinuous slits in the newly designed UACS laminates suppress the delamination growth in the outside regions around the ends of discontinuous slits efficiently. UACS laminate with bi-angled slit distribution performs best material properties including the stiffness, strength and formability among the three kinds of UACS laminates.

Tensile tests and damage progression analysis in the above three kinds of UACS laminates with different widths are investigated to reveal the size effects. The results indicate that the test strength increases accompanied with the specimen width increasing. High interlaminar stresses are performed near the free edge of the UACS laminates under tension, which inclined to form large area of delamination in these regions easily.

CONTENTS

CHAPTER 1 Introduction 1

1.1 General background 2

1.2 Introduction of the first UACS laminates 6

1.3 Main works in improving the strength of UACS 11

1.3.1 Interlaminar toughening of UACS laminates 12

1.3.2 UACS with continuous and angled slits 16

1.4 Objective and outline 19

Bibliography 22

CHAPTER 2 Fabrication, tensile and flowability experiments of newly designed UACS laminates 27

2.1 Introduction 28

2.2 Fabrication of UACS laminates 28

2.2.1 Material 28

2.2.2 Introducing the slits into the prepreg 28

2.2.3 Fabrication of the UACS laminates 33

2.3 Tensile experiment of UACS laminates 38

2.4 Experimental results and discussions 40

2.5 Flowability test of UACS lamina 50

2.5.1 Flowability test procedures 50

2.5.2 Flowability tests results 52

2.6 Summary 54

Bibliography 56

CHAPTER 3 Multiscale analysis of damage progression in newly designed UACS laminates 57

3.1 Introduction 58

3.2 Multiscale FEM models of UACS laminates for damage progression analysis 59

3.3 Homogenization analysis 63

3.3.1 Formulation of homogenization analysis 63

3.3.2 Homogenization analysis of UACS laminas 75

3.4 Analysis of damage progression in the UACS laminates 76

3.4.1 Bilinear constitutive model for the cohesive interface elements 78

3.4.2 Maximum stress criterion 84

3.4.3 Damage progression analysis 85

3.5 Results and discussion 87

3.6 Summary 100

Bibliography 102

CHAPTER 4 Size effects in tensile properties of newly designed UACS laminates 105

4.1 Introduction 106

4.2 Tensile experiment of UACS laminates with different widths 108

4.2.1 Fabrication and tensile experiment 108

4.2.2 Experimental results 109

4.3 Multiscale analysis of damage progression in UACS laminates with different widths 116

4.3.1 Multiscale FEM models 116

4.3.2 Numerical results 118

4.4 Summary 129

Bibliography 131

CHAPTER 5 Conclusions and future works 133

5.1 Conclusions..... 134

5.2 Future work..... 135

LIST OF FIGURES 137

LIST OF TABLES..... 143

LIST OF PUBLICATIONS 145

ACKNOWLEDGEMENTS..... 147

CHAPTER 1

Introduction

This chapter describes the development of the short carbon fiber reinforced polymers (CFRP), the origination of unidirectionally arrayed chopped strands (UACS), and the previous main works in improving the mechanical properties of UACS, as well as the main objective and outline of this study.

1.1 General background

Advanced composite material represents a new generation of materials made by either of carbon fiber, aramid fiber, advanced glass fiber, and ceramics fiber, or by their hybrid reinforced polymer matrix, or metal matrix, or ceramic matrix, and so on. Compared to conventional materials such as various metals, glass, and plastics, composites are composed of at least two different solid media in order to combine the best properties of the constituents or to create new properties, which neither of the components itself possesses. For example, the strengths of many fibers such as glass fiber, carbon fiber, ceramics fiber are much higher than original bulk materials. When such fibers are embedded in a matrix such as polymer, metal, and ceramics, the resulting composites present strength comparable with conventional high strength materials but at much lower density. Additionally, other properties that can be improved by combining two or more materials are: stiffness, fatigue strength, corrosion resistance, wear resistance etc. This makes composite materials very attractive for the applications of weight sensitive structures such as aircraft [1-5], automotive [6-10], wind energy structures [11-13], civil engineering [14-16], and sporting goods [17].

In recent years, research on the application of CFRP to various transportation vehicles has attracted more and more attention with the increasing requirements of energy saving vehicles and clean living environment. As the evidence of great progress, CFRP has been successfully applied to primary structures of airplanes, such as the Airbus A380 and the Boeing 787 (Fig. 1-1). Now, more and more researchers and automobile manufacturers are concerned with the application of CFRP to mass-produced automobiles due to the rapid increase of fuel prices and the increasing world-wide requirements of clean-air

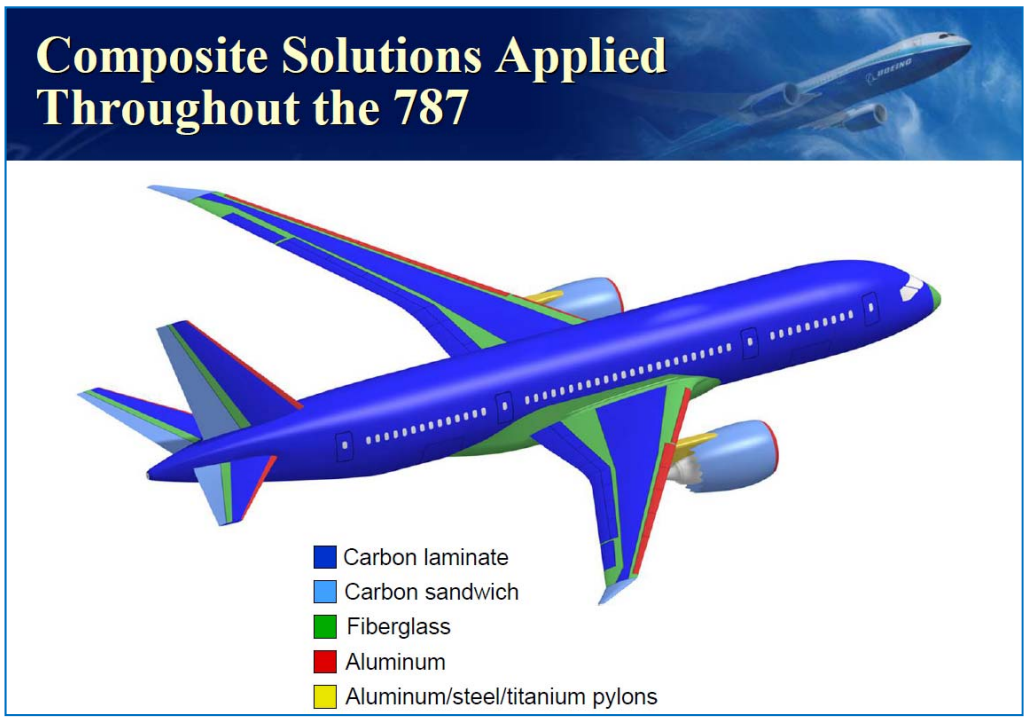

Nelson T. 787 systems and performance, 2005.

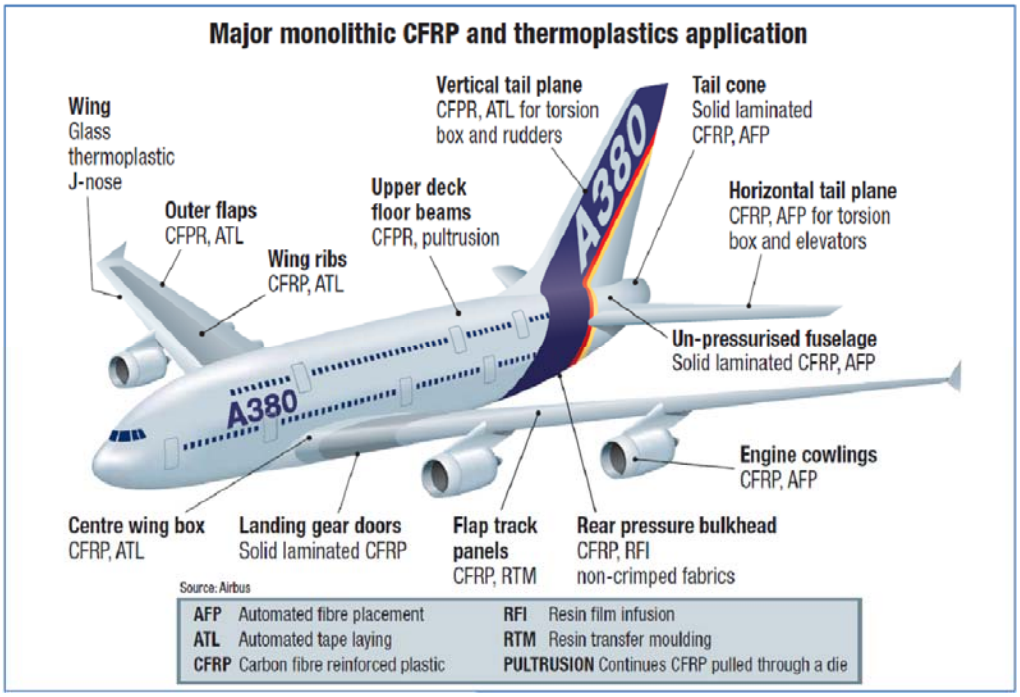

From MACHINERY February 2004

Figure 1-1: Overview of material application in the Boeing 787 and the Airbus A380.

environment. On the other hand, the application of CFRP to automobiles must consider different requirements compared to aircraft applications because the structural components of automobiles are relatively small and their geometries are more complicated. It is relatively easy to apply CFRP with continuous fibers to large and nearly flat or straight structural components. In contrast, it is not so simple to apply such CFRP to automobile structural components with various complicated geometries due to the poor flowability of CFRP prepreg in the fiber direction.

For this reason, injection molding and sheet molding compound (SMC) are widely used in fabricating structural components in complex shapes owing to its excellent formability and relatively low cost [18-24]. However, the fibers are distributed randomly in the composites and the fiber volume fraction (equal to or less than 40%) is much lower than that (about 60%) of continuous fiber reinforced plastics due to the limitation of these two fabrication methods. As a result, random distribution of fibers and relatively low fiber volume fraction lead to quite low stiffness and strength compared to conventional CFRP with continuous fibers and nearly 60% fiber volume fraction. These shortages limit the application of traditional short fiber reinforced composites in few secondary structural components of automobiles.

To enhance the strength and stiffness of short fiber reinforced polymers for the application to the primary structural components, many efforts [25-33] have been carried out at the enhancement of fiber volume fraction and the high alignment of fibers. Highly aligned discontinuous fiber yarn and prepreg with highly aligned unidirectional short fibers were developed in [25, 26] using the technology of stretch-broken carbon fibers. This technology can fabricate short fiber composites with highly aligned fibers and high

fiber volume fraction. On the other hand, it seems difficult to control the fiber length by this technology. A different approach was studied using random chopped strands made by cutting the conventional CFRP prepreg with continuous carbon fibers in [27, 28]. This approach can fabricate short fiber composites with high fiber volume fraction which is near the original composites with continues fibers, but the chopped strands are randomly distributed in the composites. This material is suitable for fabricating complex structures with low manufacturing cost and is used in fabricating the window frame of Boeing 787 (Fig. 1-2). Nevertheless, high porosity and random distribution of chopped strands result in much lower strength than conventional CFRP.

Figure 1-2: Window frame of the Boeing 787 [28].

Being different from the above mentioned approaches, recently, a new short fiber reinforced polymer made by unidirectionally arrayed chopped strands (UACS) has been developed [29-33]. The UACS is made by introducing specific slits into a conventional prepreg with continuous carbon fibers, which has superior formability and is suitable to

fabricate structural components in complex geometries since the fibers are cut into short ones. The experimental results indicated that the UACS laminates have higher strength and modulus than conventional short fiber reinforced polymers due to the high aligned fibers and high fiber volume fraction. In the early research on the UACS laminates, two kinds of UACS prepregs are studied [29-31], as described in the next subsection. The first kind of UACS prepreg has staggered short slits perpendicular to the fibers [29], and the second one has continuous slits with a small angle to the fiber direction [31]. Much higher strength is obtained for the second kind of UACS laminates than the first kind.

1.2 Introduction of the first UACS laminates

The development of early UACS laminates is described in this subsection. UACS is made by introducing regular slits into prepregs before curing. The schematic diagram of the first designed UACS is shown in Fig. 1-3, developed in [29]. The regular and discontinuous slits of 12.5 mm in length at an interval of 25 mm are introduced into the prepreg. All the slits are perpendicular to the fiber direction and all the fiber are cut into 25 mm in length in the UACS prepreg. As mentioned here, the UACS is a sheet-like molding material made of regularly and unidirectionally arrayed discontinuous fiber strands impregnated with unsaturated thermoset resin. This constitution allows the fiber strands flowing smoothly during molding while the stress concentration is minimized by isolating the mutual position of the strands-ends. Thus, complexly shaped components such as rib structures can be fabricated by UACS plies. The UACS laminates can be stacked by multiple UACS plies according to the design of the layer sequence. The stacked laminate is then cured at 3MPa pressure and 150 ^{o}C for 30 minutes by hot

pressing. Compared with previous short fiber reinforced polymers made by SMC and injection molding technologies, the layer structure and the high fiber volume (about 60%) of conventional CFRP laminates are maintained and the fiber directions are uniform in a single ply of UACS laminates.

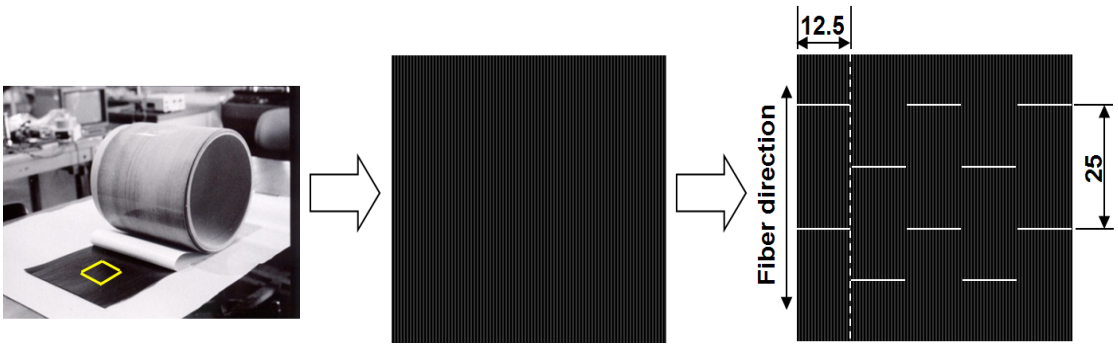

Figure 1-3: Schematic of the first UACS created by introducing slits in arrayed continuous fibers of prepreg.

In order to investigate the mechanical properties of UACS laminates in [29], the UACS plies are stacked into the quasi-isotropic lamination of $[45/0/-45/90]_{2S}$ and tensile experiment was conducted. Fig. 1-4 presents the experiment results of the tensile modulus and strength of the quasi-isotropic laminate stacked by UACS plies together with those of SMC and conventional CFRP laminate without slits for a comparison. The strength of UACS laminate was twice of SMC and the scatter range was much narrower similar to that of the conventional laminate. In addition, the tensile modulus, which is close to that of conventional CFRP laminate, was much higher than that of SMC.

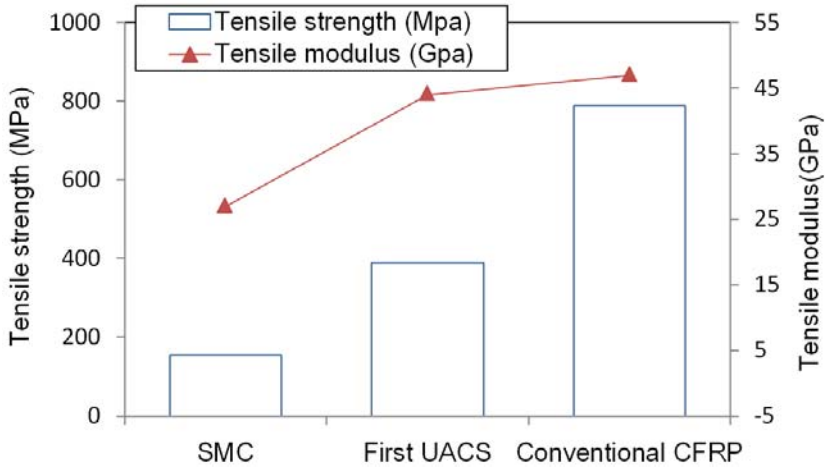

Figure 1-4: Comparison of modulus and strength between SMC, the first UACS and conventional CFRP.

The photographs of the cross-sections and the fractured specimens obtained from the SMC, UACS and conventional CFRP laminates are presented in Fig. 1-5. In the case of SMC, the chopped strands are crimped in the thickness direction, and several resin-rich regions are seen. In contrast, UACS laminate does not include any resin-rich regions, except for just around the slits. This is the main reason for the high modulus of the UACS laminate. Additionally, observed from the fractured of various specimens, SMC is seen to have a zigzag fracture plane, implying that the crack generated in the resin-rich regions grows in the coupon, avoiding the chopped strands, and causes the final failure. In contrast, a large delamination is generated in the initial UACS laminate, in spite of matrix cracking observed before the delamination. Delamination was assumed to be induced only by the shear stress concentration around the slits, without the matrix cracking effect. No fiber breakage occurs even near the slits in the UACS laminate. It concluded that the interlaminar delamination caused the final failure of the UACS.

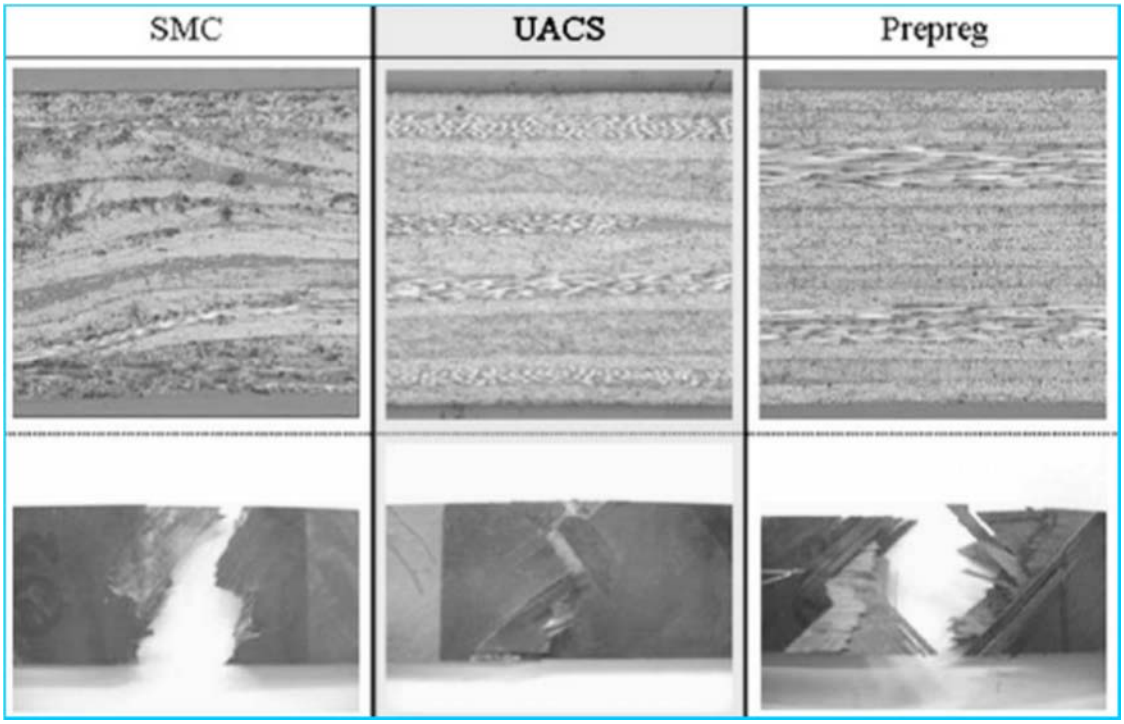

Figure 1-5: Comparison of cross-sections and fractured coupons of SMC, the first UACS and conventional CFRP [29].

On the other hand, in the application of CFRP laminates, flowability is quite important since many structures of mass-produced cars have various complex shapes. Therefore, discontinuous carbon fiber reinforced polymers are much preferred over continuous fiber reinforced fiber reinforced polymers for achieving better formability. Although it is revealed that the first UACS laminate has better mechanical properties than the injection molding and SMC, the flowability of the UACS laminate should also be clarified.

In order to clarify the flowability of the UACS laminate, a stretched UACS laminate with 31% area increase, compared to original UACS ply before hot pressing, was fabricated by hot pressing at 3 MPa pressure and 150 ^{o}C for 30 minutes, as shown in Fig.

1-6. The UACS prepreg was cut into sheets of 250 mm × 250 mm and these sheets are stacked in the laminate configuration of $[45/0/-45/90]_{2S}$. Then, the stacked UACS plies are set in the mold cavity of 300 mm × 300 mm and cured at 3 MPa pressure and 150 ^{o}C for 30 minutes. As a result, the area of the UACS laminate increased by 31% after hot pressing, compared to the original UACS ply before hot pressing. This fact demonstrated that this UACS laminate has the same excellent flowability as SMC.

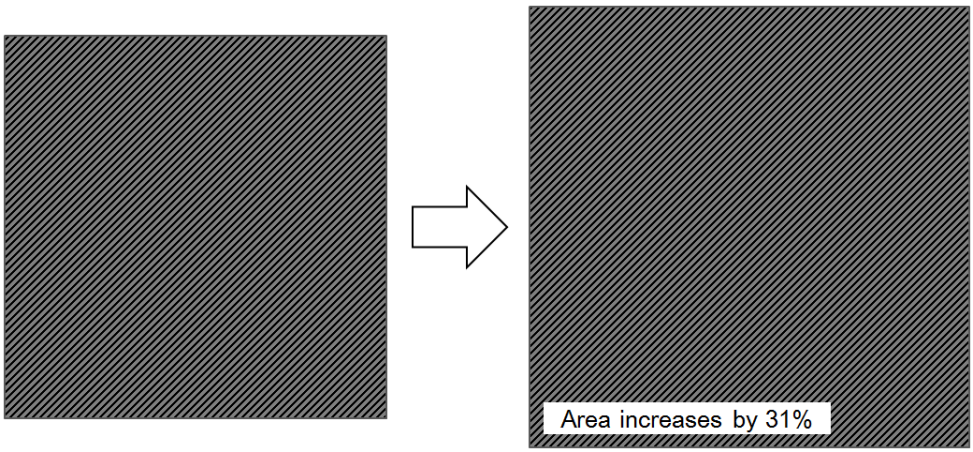

Figure 1-6: Compression moldings of a quasi-isotropic UACS stack into a flat plate laminate.

Furthermore, in order to investigate the layer structure of the UACS laminated component, T-shaped rib components with present UACS prepreg and conventional prepreg without slits are fabricated, as shown in Fig. 1-7. Large resin-rich region is seen in the case of rib component fabricated by conventional prepreg. In contrast, no such resin-rich region is observed in the case of the component fabricated by present UACS prepreg and the layer structure of UACS plies is still maintained even in the rib part.

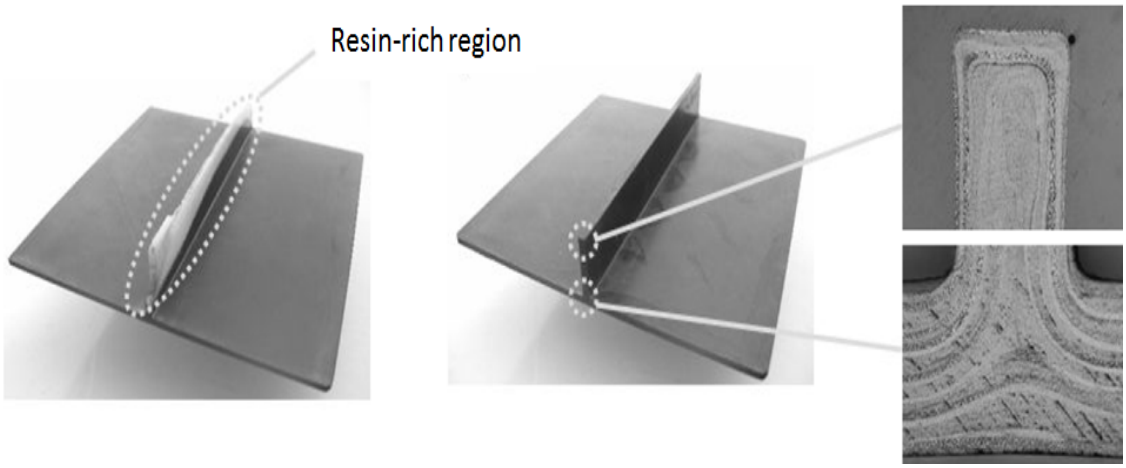

Figure 1-7: A T-shaped rib structure made from quasi-isotropic stacks of conventional prepreg (left) and the first UACS prepreg (right) [29].

1.3 Main works in improving the strength of UACS

As mentioned in previous subsection, initial UACS is a sheet-like molding material made of regularly and unidirectionally arrayed discontinuous fiber strands impregnated with unsaturated thermoset resin. This constitution allows the fiber strands flowing smoothly during molding while the stress concentration is minimized by isolating the mutual position of the strands-ends. Additionally, it demonstrated that complexly shaped components such as rib structures can be fabricated by stacking initial UACS plies. Moreover, the layer structure is maintained after processing and only few resin-rich regions are observed.

Initial UACS laminates performs higher strength compared with previous short carbon fiber reinforced polymers. But the strength of the early UACS is relatively low compared to conventional CFRP laminate due to that delamination is the principal cause of the final failure, subsequently, the early UACS only can be fabricated as the no-

bearing structures and secondary-bearing structures. In order to improve the strength of UACS without reducing the flowability, many researches are conducted. The main works in improving the strength of UACS include interlaminar toughening and adjusting of the slit angle (the angle between the slits and fiber direction).

1.3.1 Interlaminar toughening of UACS laminates

Based on the consideration of inhibiting the delamination in the UACS laminate, the following three interlaminar toughening methods are tried [30]: (1) Toughening the matrix resin itself; (2) Inserting a toughened interlaminar layer into the plies; (3) Localizing the toughened layer only around the ends of the chopped strands.

(1) Toughening the matrix resin

In the first trial of interlaminar toughening, the matrix of the UACS itself was exchanged for toughened resin. A fresh prepreg of P3252S-15 (Toray Industries), made of carbon fiber T700S and epoxy resin #2521R is used for fabricating UACS laminate. It has an areal weight of carbon fiber of 150 g/m^2, fiber volume fraction of 58%, longitudinal modulus of 130 GPa, Poisson's ratio of 0.34, and longitudinal tensile strength of 2760 MPa. In the same way as in the previous subsection, 12.5 mm-wide slits were introduced into the prepreg at intervals of 25 mm. Those UACS plies were then stacked and cured to obtain a UACS laminate with a quasi-isotropic lamination of $[45/0/-45/90]_{2S}$. Tensile tests were conducted. The UACS laminate with the toughened matrix #2521R improves the strength by 14%. It is noted that a conventional CFRP laminate with #2521R also improved the strength by 9%. On contrary, the fracture morphologies of the first UACS laminate and the UACS laminate with #2521R closely resemble. This

demonstrates that the strength of UACS is strongly dependent on the damage progress due to the delamination.

(2) Inserting a toughened interlaminar layer into plies

Toughened interlaminar layers are widely used in real applications of composite materials. For the most prominent example, T800S/#3900-2B prepreg (Toray Industries), which includes inter-layers with fine thermoplastic particles, has already been applied in the primary structure of the Boeing 777. The purpose of a toughened interlaminar layer is to suppress the progress of interlaminar delamination, caused primarily by out-of-plane impact, and to maintain the compression strength of the laminates.

In order to improve the interlaminar toughness, the thermoplastic non-woven fabric is used as the toughened interleaves. This fabric is tougher than the matrix resin of early UACS laminate. To ensure compatibility between fabric and matrix at the hot pressing temperature (150ºC), several low-melting thermoplastic non-woven fabrics were prepared as follows: polyamide non-woven fabrics (melting temperature T_m = 150 ^{o}C) in different areal weights (10 g/m^2, 20 g/m^2, and 30 g/m^2), polyamide non-woven fabric (T_m = 120 ^{o}C) in an areal weight of 30 g/m^2, and polyolefin non-woven fabric (T_m = 150 ^{o}C) in an areal weight of 30 g/m^2. UACS plies were prepared in the same way as described in previous subsection. The UACS plies and the thermoplastic non-woven fabrics were alternately stacked and cured to obtain UACS laminate with a quasi-isotropic lamination of $[45/0/-45/90]_{2S}$. In particular, thermoplastic non-woven fabrics were also stacked on both surfaces of the UACS laminate.

The tensile modulus and strength were evaluated in Fig. 1-8. Inserting polyamide non-woven fabrics improves the strength by up to 17%. The UACS laminate with polyamide

non-woven fabrics in an areal weight of 30 g/m^2 has less strength than that in an areal weight of 20 g/m^2. Thus, an optimized interlaminar thickness for the toughened layer with regard to tensile strength seems to exist. In contrast, inserting polyolefin non-woven fabrics reduces the strength. It decreases the interlaminar toughness because polyolefin has poor adhesion to carbon fibers and the epoxy resin matrix. Consequently, it was concluded through this study that inserting appropriately toughened interleaves into UACS plies can improve the tensile strength. This study also verified that delamination was still the principle damage which caused the final failure of the UACS laminate. However, the tensile modulus is significantly reduced. For example, inserting polyamide non-woven fabric in 20 g/m^2 improved the strength by 17%, but reduced the modulus by 18%. This is because the toughened interleaves decreased the volume fraction of fiber of the UACS laminate.

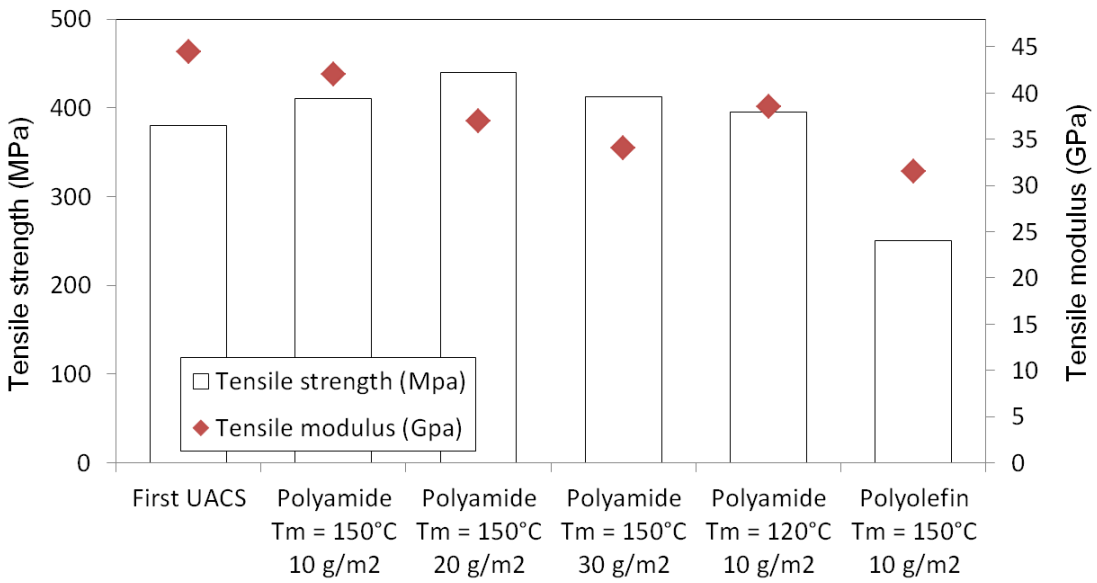

Figure 1-8: Comparison of tensile modulus and strength of quasi-isotropic laminates including different toughened interlaminar layers.

(3) Localizing toughened layer around the ends of chopped strands

As the final trial, instead of inserting the toughened interleaf into every interface between the UACS plies, this trail tried a locally toughening method only around the ends of the slits, as shown schematically in Fig. 1-9.

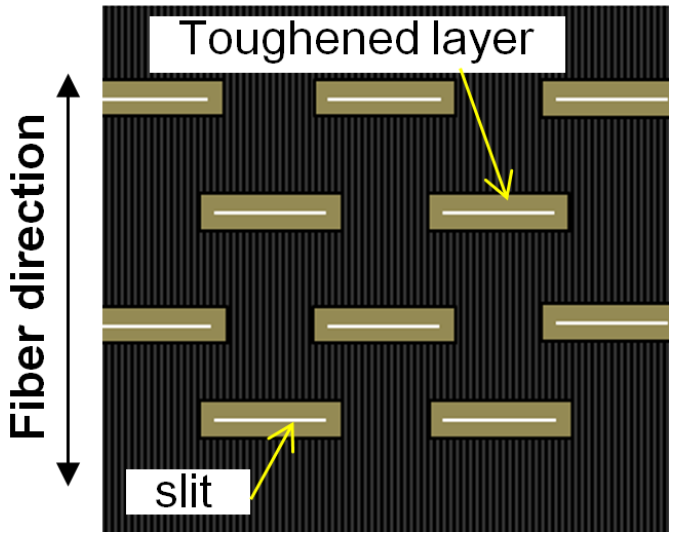

Figure 1-9: Schematic diagram of UACS with interlaminar toughened layers only around the slits.

The polyamide non-woven fabric (T_m = 120 °C) in an areal weight of 30 g/m2 was used as toughened interleaf and it is cut into pieces (3 × 15 mm). In the same way as described in above subsections, 12.5 mm-wide slits at intervals of 25 mm were introduced into the prepreg to make the UACS prepreg, and then the UACS prepreg was cut into sheets (300 × 300 mm) as 0° plies. The pieces of the toughened interleaves were stuck by hand onto the 12.5 mm-width slits from both faces of the UACS 0° ply. In addition, ordinary prepreg without slits was cut into sheets (300 × 300 mm) for the 45°, 90° and -45° plies. The 0° UACS plies and 45°, 90°, and -45° ordinary prepreg plies are

stacked and cured to obtain a UACS laminate with a quasi-isotropic lamination of [45/0/-45/90]$_{2S}$.

As summarized in Fig. 1-10, the tensile strength of UACS is improved by 21%, and the tensile modulus was reduced by only 10%, using locally toughening method. Although a locally toughened interleaf can only suppress the onset of delamination, it directly and positively affects the strength. In addition, the relatively small amount of toughened interleaf layer inserted minimizes the decline in the fiber volume fraction and the modulus of the UACS laminate.

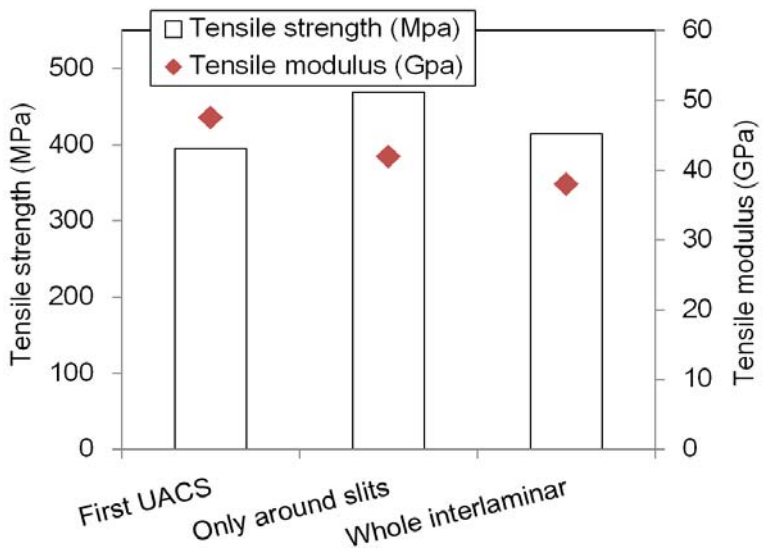

Figure 1-10: Comparison of tensile modulus and strength of quasi-isotropic laminates with different areas of toughened layers.

1.3.2 UACS with continuous and angled slits

From above subsections, it is seen that the slits are still perpendicular to the fibers. That is, the problem of high stress concentration around the tips of slits in the UACS laminate is still unsolved. To reduce the stress concentration around the tips of slits in the UACS laminate and to further improve the strength of early UACS laminates, Takeda et

al. [31] propose a second design of UACS ply by introducing continuous and angled into the prepreg. The optical image of the second designed UACS ply and the schematics of the relative UACS laminate are given in Fig. 1-11. The angle between the fiber direction and the slit is about 11-degree and the fiber length are 25 mm in length which is as same as the early UACS ply.

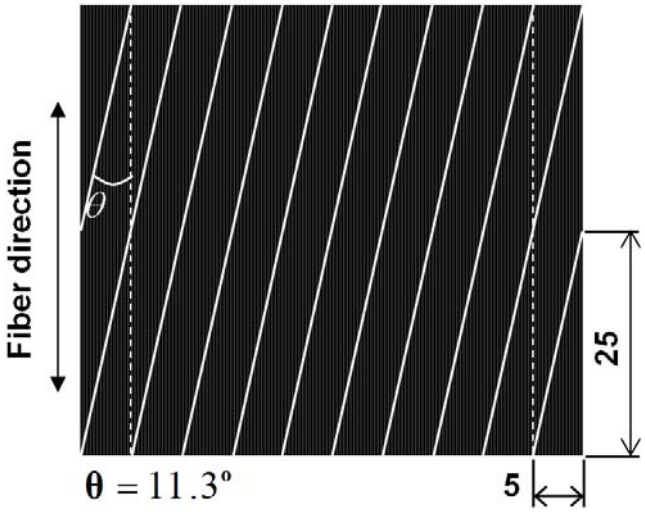

Figure 1-11: Schematic diagram of UACS by introducing continuous angled slits in prepreg.

In Fig. 1-12, the mechanism of why the small angle can reduce the stress concentration and suppressing the initiation of delamination is described. A local square region is selected as an analysis model and the average in-plane stresses occurred due to the tensile stress σ applied in the fiber direction are expressed by axial stress σ_x, σ_y and shear stress τ_{xy},

$$\sigma_x = \sigma \cos^2 \theta, \quad \sigma_y = \sigma \sin^2 \theta, \quad \tau_{xy} = \sigma \cos 2\theta/2, \tag{1-1}$$

In the case of first UACS (θ= 90°), σ_x=0, τ_{xy} = 0, and σ_y = σ. Therefore, the stress σ_y applied to the slit in the direction perpendicular to the slit is maximized, so the shear stress around the slit is also maximized due to load transfer at the interface. In contrast, in

the case of UACS with a slit small angled at a smaller θ, σ_x becomes larger and σ_y and τ_{xy} become smaller. σ_x does not contribute to the initiation of delamination from the slit because σ_x is parallel to the slit, while the shear stress around the slit caused by σ_y and τ_{xy} are responsible for delamination in modes II and III. Therefore, the initiation of delamination around slits is not as so severe as the early UACS laminates.

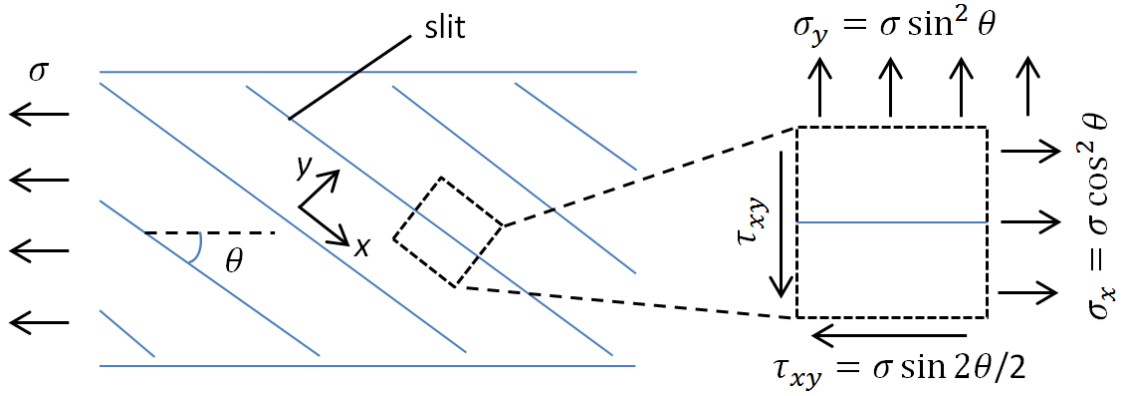

Figure 1-12: Schematic diagram of stress distribution around an continuous angled slit in the 0° ply.

In this study, effects of the slit angle on the strength of the UACS laminates are investigated. The UACS plies with angled slits were stacked in a quasi-isotropic lamination of $[45/0/-45/90]_{2S}$ and cured by a hot pressing. Two kinds of UACS laminates with 31% stretched and non-stretched shapes are fabricated to investigate the flowability during the curing process. The stretch of UACS occurred due to the flowability of chopped strands under the pressure of 3MPa in hot pressing process. The angled slit direction was +θ on the upper half of the laminate $[45/0/-45/90]_2$ and –θ on the lower half. Tensile tests of the secondly designed UACS laminates are also conducted. The relation between the tensile strength of quasi-isotropic UACS laminates and the slit angle θ are

presented in Fig. 1-13. As the slit angle becomes smaller than 45°, the tensile strength dramatically increases, approaching that of conventional laminate without slits (θ = 0°). The UACS laminates with an area increase (31% stretched) exhibit higher strength than those of non-stretched UACS laminates for each slit angle because the each ply in stretched laminates becomes thinner than original ply.

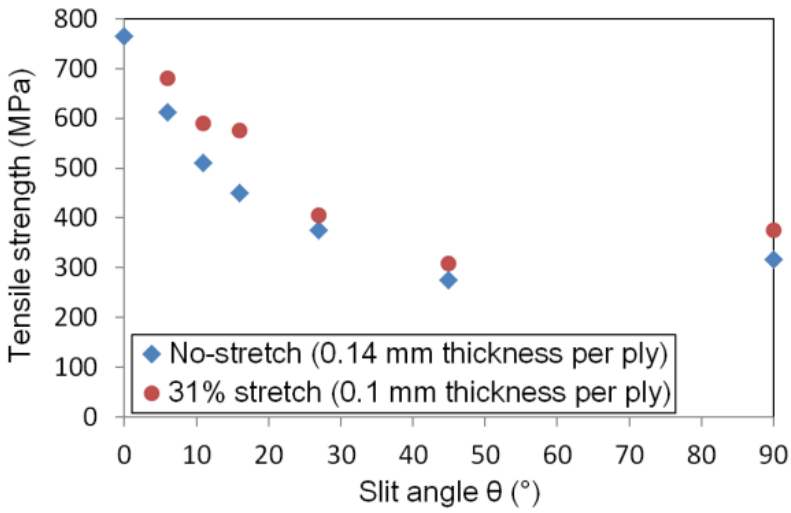

Figure 1-13: Relation between tensile strength of quasi-isotropic UACS laminates and the slit angle.

1.4 Objective and outline

Although the above mentioned early UACS laminates exhibit better mechanical properties and similar flowabilty compared to traditional short fiber reinforced composites made by such as injection molding and SMC, the final failure of the early UACS laminates even the secondly designed UACS laminate with continuous angled slits are still dominated by the delamination progression and fiber breakage is rarely observed. It means that the high strength advantage of the carbon fiber is still not efficiently utilized. Large delamination easily occurs and extends along the continuous

slits due to the stress concentration along the slits. Is there an idea slit distribution pattern which allows UACS laminates to perform not only excellent flowability but also more excellent mechanical properties? In order to explore the answer, two newly designed UACS prepregs, namely, with discontinuous staggered angled slits and with discontinuous bi-angled slits, are proposed and investigated experimentally and numerically in this study [32, 33].

The objective of the present dissertation is to reveal the mechanic properties of newly designed UACS with different slit patterns. Tensile experiment and damage progression analysis based on finite element method (FEM) are conducted. In addition, effects of specimen size on the tensile properties of various UACS laminates are investigated by experiment and FEM analysis.

The outline of this dissertation is listed as below:

Chapter 1 introduced the general background of short carbon fiber reinforced polymers and the previous research on the early UACS laminates.

Chapter 2 describes fabrication of two kinds of newly designed UACS laminates, one is contains staggered angled slits and the other contains bi-angled slits. A hand-made technique to introduce the two kinds of slit distribution patterns is introduced in detailed. Quasi-isotropic UACS laminates with various slit patterns together with the conventional laminate without slits are fabricated for tensile tests. Additionally, hybrid laminates [90/0/90] with two unidirectional glass-fiber/epoxy plies and one UACS ply are fabricated for flowability tests.

Chapter 3 simulates the damage progression in newly designed UACS laminates and existing UACS laminate with continuous slit pattern under tension based on a multiscale

analysis. A FEM multiscale model is constructed. Cohesive interface element and maximum stress criterion are employed for the simulation of the progression of delamination and other failures in the laminates, respectively.

Chapter 4 investigates the size effects in tensile properties of various UACS laminates. Specimens with different widths are fabricated for tensile experiment. Additionally, FEM analysis of damage progression in the UACS laminates are studied based on the multiscale models to reveal the influences of specimen width on the tensile properties of UACS laminates.

Chapter 5 summarizes the major results of the present dissertation.

Bibliography

[1] Thuis HG. Development of a composite cargo door for an aircraft. *Composite Structures*, 1999; 47(1-4): 813-819.

[2] Shokrieh, MM, Taheri BF. Wing instability of a full composite aircraft. *Composite Structures,* 2001; 54(2-3): 335-340.

[3] Okafor, AC, Singh N, Enemuoh UE, Rao SV. Design, analysis and performance of adhesively bonded composite patch repair of cracked aluminum aircraft panels. *Composite Structures,* 2005; 71(2): 258-270.

[4] Murugan S, Saavedra Flores EI, Adhikari S, Friswell MI. Optimal design of variable fiber spacing composites for morphing aircraft skins. *Composite Structures,* 2012; 94(5): 1626-1633.

[5] Kapidžić Z, Nilsson L, Ansell H. Finite element modeling of mechanically fastened composite-aluminum joints in aircraft structures. *Composite Structures,* 2014; 109(0): 198-210.

[6] Schouwenaars R, Cerrud S, Ortiz A. Mechanical analysis of fracture in an automotive radiator head produced from a nylon–glass fibre composite. *Composites Part A: Applied Science and Manufacturing,* 2002; 33(4): 551-558.

[7] Corum JM, Battiste RL, Ruggles-Wrenn MB. Low-energy impact effects on candidate automotive structural composites. *Composites Science and Technology,* 2003; 63(6): 755-769.

[8] Ruggles-Wrenn MB, Corum JM, Battiste RL. Short-term static and cyclic behavior of two automotive carbon-fiber composites. *Composites Part A: Applied Science and Manufacturing*, 2003; 34(8): 731-741.

[9] Lee DG, Sung Kim H, Woon KJ, Kook KJ. Design and manufacture of an automotive hybrid aluminum/composite drive shaft. *Composite Structures,* 2004; 63(1): 87-99.

[10] Lee SW, Lee DG. Composite hybrid valve lifter for automotive engines. *Composite Structures*, 2005; 71(1): 26-33.

[11] Tseng YC, Kuo CY. Engineering and construction torsional responses of glass-fiber/epoxy composite blade shaft for a small wind turbine. *Procedia Engineering,* 2011; 14(0): 1996-2002.

[12] Lanting Z. Research on Structural Lay-up Optimum design of composite wind turbine blade. *Energy Procedia,* 2012; 14(0): 637-642.

[13] Kim T, Hansen AM, Branner K. Development of an anisotropic beam finite element for composite wind turbine blades in multibody system. *Renewable Energy,* 2013; 59(0): 172-183.

[14] Marouani S, Curtil L, Hamelin P. Ageing of carbon/epoxy and carbon/vinylester composites used in the reinforcement and/or the repair of civil engineering structures. *Composites Part B: Engineering,* 2012; 43(4): 2020-2030.

[15] Awad ZK, Aravinthan T, Zhuge Y, Gonzalez F. A review of optimization techniques used in the design of fibre composite structures for civil engineering applications. *Materials & Design,* 2012; 33(0): 534-544.

[16] Böer P, Holliday L, Kang THK. Independent environmental effects on durability of fiber-reinforced polymer wraps in civil applications: A review. *Construction and Building Materials,* 2013; 48(0): 360-370.

[17] Slater C, Otto SR, Strangwood M. The quasi-static and dynamic testing of damping in golf clubs shafts fabricated from carbon fiber composites. *Procedia Engineering,* 2010; 2(2): 3361-3366.

[18] McGrath JJ, Wille JM. Determination of 3D fiber orientation distribution in thermoplastic injection molding. *Composites Science and Technology*, 1995; 53(2): 133-143.

[19] Vivekanandhan S, Misra M, Mohanty AK. Thermal, mechanical, and morphological investigation of injection molded poly (trimethylene terephthalate)/carbon fiber composites. *Polymer Composites*, 2012; 33(11): 1933-1940.

[20] Beardmore P, Johnson CF. The potential for composites in structural automotive applications. *Composites Science and Technology*, 1986; 26(4): 251-281.

[21] Oldenbo M, Fernberg SP, Berglund LA. Mechanical behavior of SMC composites with toughening and low density additives. *Composites Part A: Applied Science and Manufacturing*, 2003; 34(9): 875–885.

[22] Hosseinzadeh R, Shokrieh MM, Lessard LB. Parametric study of automotive composite bumper beams subjected to low-velocity impacts. *Composite Structures*, 2005; 68(4): 419–427.

[23] Friedrich K, Almajid AA. Manufacturing aspects of advanced polymer composites for automotive applications. *Applied Composite Materials*, 2013; 20(4): 107-128.

[24] Palmer J, Savage L, Ghita OR, Evans KE. Sheet moulding compound (SMC) from carbon fibre recyclate. *Composites Part A: Applied Science and Manufacturing*, 2010; 41(9): 1232–1237.

[25] Benson S. Materials and processing-move into the 90's. *Material and Manufacturing Progresses,* 1991; 6(4): 753–757.

[26] Chang IY, Pratte JF. LDF™ thermoplastic composites technology. *Journal of Thermoplastic Composite Materials,* 1991; 4(3): 227–252.

[27] Feraboli P, Peitso E, Cleveland T, Stickler P, Halpin JC. Notched behavior of prepreg-based discontinuous carbon fiber/epoxy systems. *Composites Part A: Applied Science and Manufacturing,* 2009; 40(3): 289-299.

[28] Feraboli P, Cleveland T, Ciccu M, Stickler P, Deoto L. Defect and damage analysis of advanced discontinuous carbon/epoxy composite materials. *Composites Part A: Applied Science and Manufacturing,* 2010; 41(7): 888–901.

[29] Taketa I, Okabe T, Kitano A. A new compression-molding approach using unidirectionally arrayed chopped strands. *Composites Part A: Applied Science and Manufacturing,* 2008; 39(12): 1884–1890.

[30] Taketa I, Okabe T, Kitano A. Strength improvement in unidirectional arrayed chopped strands with interlaminar toughening. *Composites Part A: Applied Science and Manufacturing,* 2009; 40(8): 1174–1178.

[31] Taketa I, Sato N, Kitano A, Nishikawa M, Okabe T. Enhancement of strength and uniformity in unidirectionally arrayed chopped strands with angled slits. *Composites Part A: Applied Science and Manufacturing,* 2010; 41(11): 1639–1646.

[32] Li H, Wang wen-xue, Takao Y, Matsubara T. New designs of unidirectionally arrayed chopped strands by introducing discontinuous angled slits into prepreg. *Composites Part A: Applied Science and Manufacturing,* 2013; 45(1): 127-133.

[33] Li H, Wang wen-xue, Matsubara T. Multiscale analysis of damage progression in newly designed UACS laminates. *Composites Part A: Applied Science and Manufacturing,* 2014; 57: 108–117.

CHAPTER 2

Fabrication, tensile and flowability experiments of newly designed UACS laminates

In this chapter, new designs of unidirectionally arrayed chopped strands (UACS) are proposed to improve the mechanical properties of existing UACS laminates with continuous angled slits by introducing discontinuous angled slits into a unidirectional prepreg. Two slit patterns of staggered angled slits and bi-angled slits are designed. Quasi-isotropic UACS laminates with new slit patterns and existing continuous angled slits together with the conventional laminate without slits are fabricated for tensile tests. Additionally, hybrid laminates [90/0/90] with two unidirectional glass-fiber/epoxy plies and one UACS ply are fabricated for flowability test.

2.1 Introduction

In this chapter, two new designs of UACS composites are proposed to improve the strength and material symmetry of existing UACS laminates by introducing two types of discontinuous angled slits into a unidirectional prepreg of conventional CFRP. Two slit patterns, namely, staggered discontinuous angled slit pattern and discontinuous bi-angled slit pattern are designed. A hand-made method is employed to introduce the slits into the prepreg using a commercial paper cutter. Tensile tests are conducted for quasi-isotropic laminates of $[45/0/-45/90]_{2S}$ fabricated by UACS prepregs with two newly designed slit patterns and with existing continuous slit pattern. Flowability tests on [90/0/90] hybrid laminates with two unidirectional glass-fiber/epoxy plies and one UACS ply are performed for UACS prepregs with two newly designed slit patterns and with existing continuous slit pattern. Tensile properties and flowability of two new UACS laminates are investigated and compared with those of existing UACS laminates.

2.2 Fabrication of UACS laminates

2.2.1 Material

Commercial available unidirectional CFRP prepreg of PYROFIL#350 (TR50S) (Mitsubishi Rayon) is used in this study. The longitudinal modulus is 142 GPa, Poisson's ratio is 0.32 and the longitudinal strength is 2950 MPa. Fiber volume fraction (V_f) and thickness of the prepreg are V_f = 60% and 0.2 mm, respectively.

2.2.2 Introducing the slits into the prepreg

As mentioned in last chapter, UACS is fabricated by introducing regular slits into a unidirectional prepreg before curing. In previous studies, an automatic cutting machine is

developed by Toray Industries and the slits are mechanically introduced into the prepreg by a tangential knife attached to the machine. In this study, newly designed UACS prepregs with two kinds of slit patterns are made by following hand-made procedures using a commercial paper cutter.

First, 0°, 45°, 90° and -45° plies with a rectangular geometry of 250 mm × 250 mm are cut out from the unidirectional prepreg, respectively. Then a separate polymer sheet and a white paper with a printed slit distribution are put on the prepreg, which is shown in Fig. 2-1. In order to avoid the scraps of the white paper adhering on the prepreg in the cutting procedure and leading to voids in the laminate after cure, a cellophane tape layer is added on the back of the printed white paper. Next, slits are introduced into the prepreg following the slit lines printed on the white paper using a paper cutter. Fig. 2-2 shows the photograph of hand-made cutting process using a paper cutter. It is worth mentioning that the cutting process must be completed in a short time due to that the prepreg becomes soft gradually with the time at the room temperature, and it is difficult to ensure the quality of uniform slits for too soft prepreg.

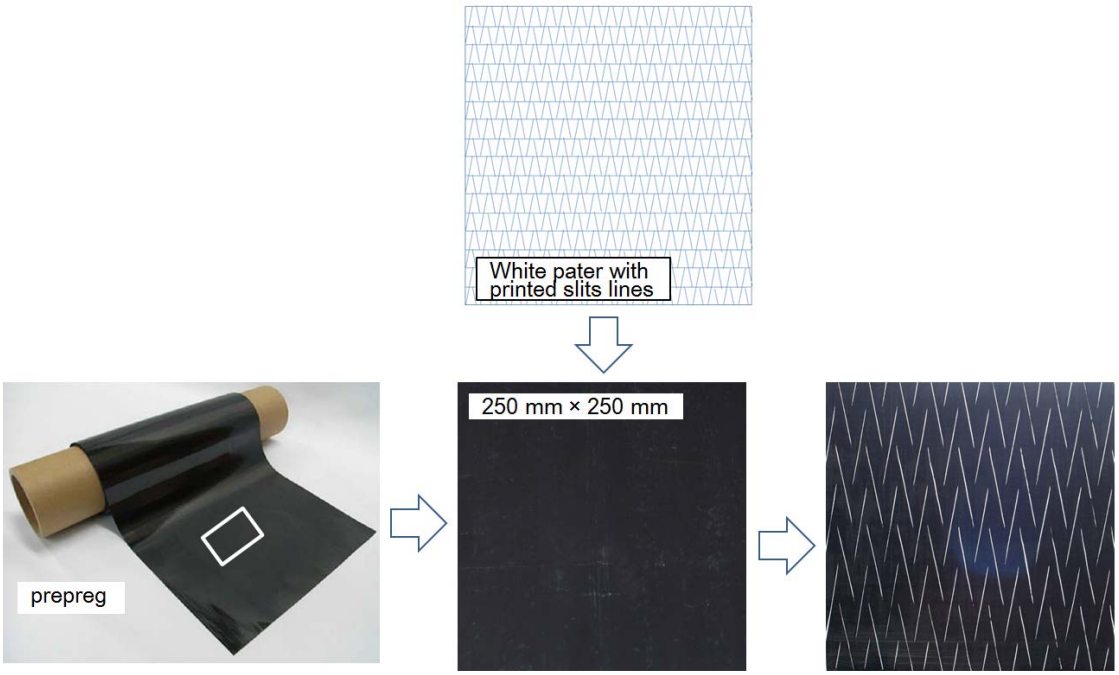

Figure 2-1: Schematic diagram of cutting procedures for fabricating a bi-angled slit pattern UACS lamina.

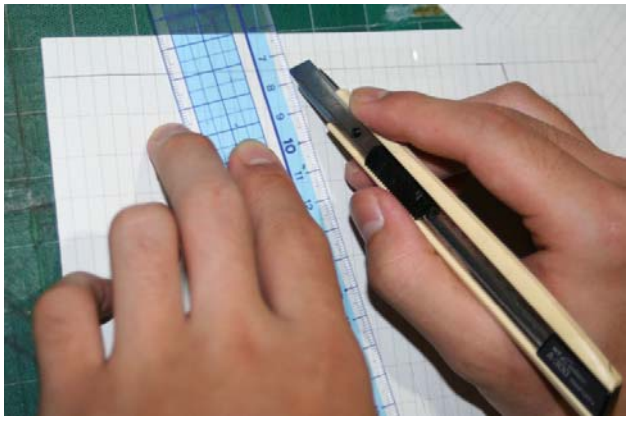

Figure 2-2: Image of cutting process of slits by using a paper cutter.

UACS prepregs used in fabricating laminates with two newly designed slit patterns and with existing continuous angled slits are made, respectively. The schematics of newly

designed slit patterns and existing continuous slit pattern are shown in detail on the left side of Fig. 2-3 and the corresponding images of UACS prepregs, taken by a transparent photography technique, are presented on the right side of Fig. 2-3. According to previous research [3], the slit angle between the slit and the fiber direction is taken as 11.3 degrees in all cases of angled plies, and the length of chopped strands is taken as 25 mm for all slit patterns. In other words, the fiber length of all UACS prepregs is 25 mm. In the right photos of Fig. 2-3, light lines represent the slits introduced into the CFRP prepreg. It is seen that slit distributions in three types of UACS prepregs are quite different.

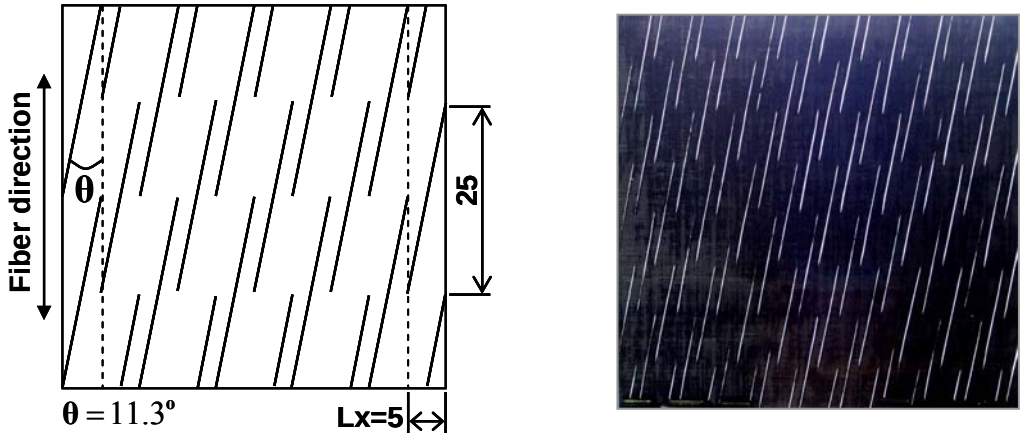

(a) Staggered slit pattern (left: schematic, right: slit prepreg)

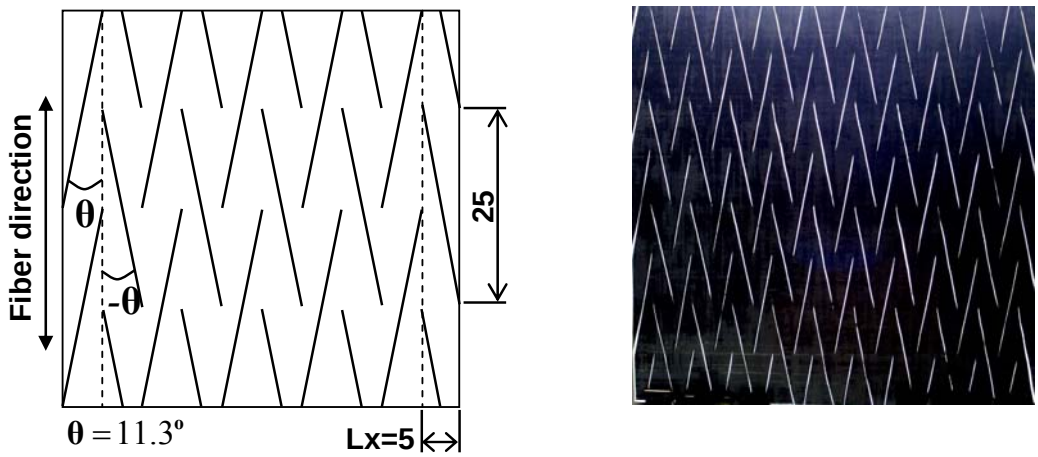

(b) Bi-angled slit pattern (left: schematic, right: slit prepreg)

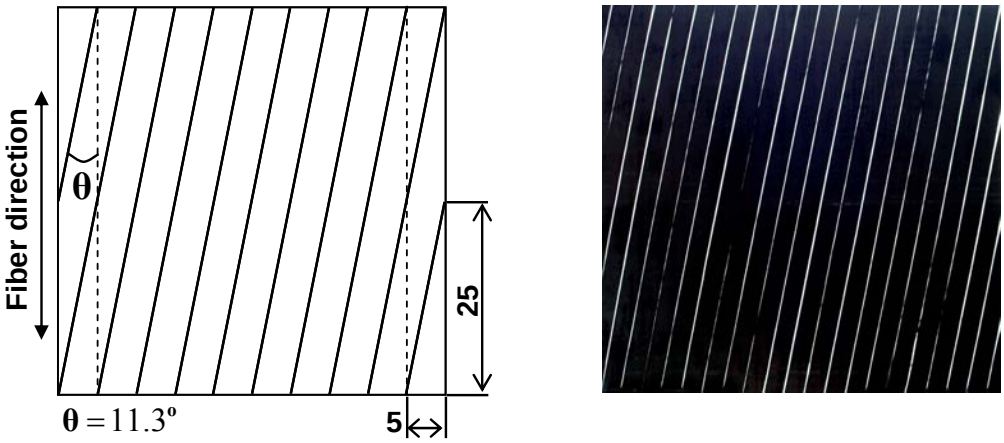

(c) Continuous angled slit pattern (left: schematic, right: slit prepreg)

Figure 2-3: Newly designed discontinuous angled slit patterns and the existing continuous angled slit pattern.

In order to investigate the influence of slit length of new slit patterns on the mechanical properties of UACS laminates, UACS prepregs with four kinds of slit lengths, namely, 25.5 mm, 38.3 mm, 51.0 mm, and 63.4 mm are also made. For simplicity, the horizontal projection L_x of the slit length, as shown in Fig. 2-3, is taken as a parameter to describe the slit length. Hence, L_x = 5 mm, 7.5 mm, 10 mm, and 12.5 mm correspond to the above four kinds of slit lengths, respectively. For instance, Fig. 2-4 presents the schematic of staggered and bi-angled slit patterns UACS plies when L_x = 10 mm.

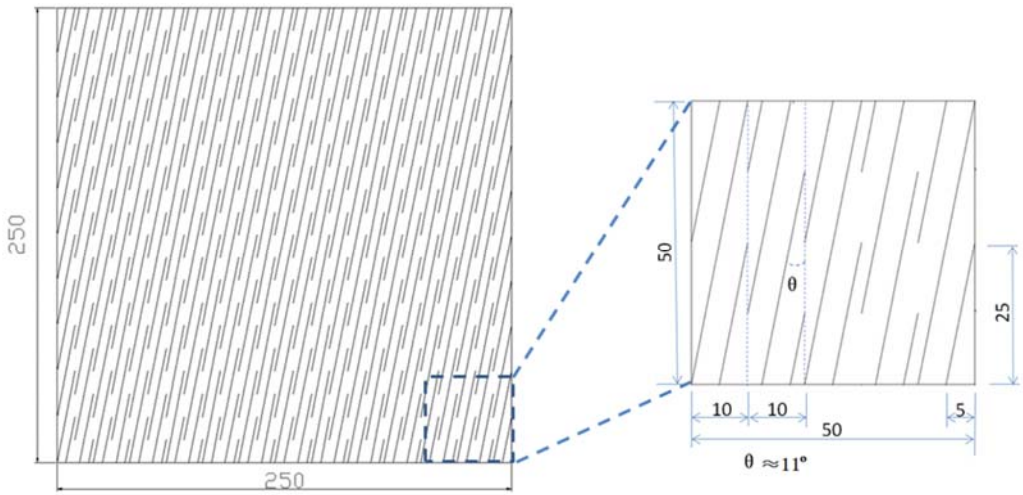

(a) Staggered slit pattern

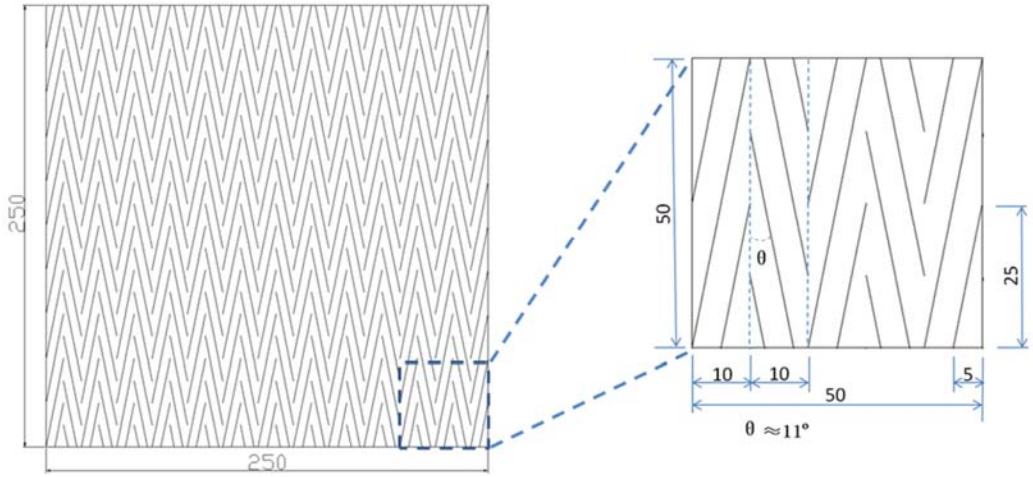

(b) Bi-angled slit pattern

Figure 2-4: Slits distribution in staggered and bi-angled pattern UACS plies when L_x = 10 mm.

2.2.3 Fabrication of the UACS laminates

Quasi-isotropic UACS laminates used for tensile tests are fabricated by the use of UACS prepregs with two newly designed slit patterns and with existing slit pattern. Firstly, the UACS prepregs of 0°, 45°, 90° and -45° are stacked in the sequence of [45/0/-

45/90]$_{2S}$. As a typical example, a schematic of stacking a laminate by UACS prepregs with discontinuous bi-angled slits is depicted in Fig. 2-5.

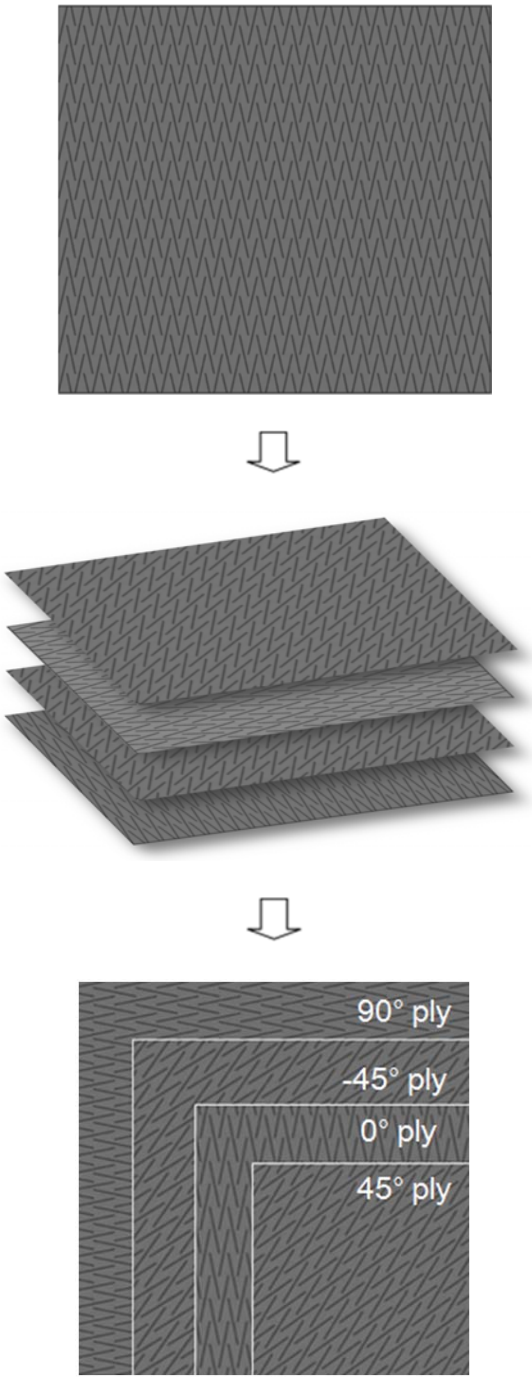

Figure 2-5: Schematic of stacking a laminate by UACS plies with discontinuous bi-angled slits.

Afterwards, stacked prepregs are cured using an autoclave (Fig. 2-6). The cure cycle recommended by the manufacture of CFRP prepregs is presented in Fig. 2-7. According to the manufacture recommend cure cycle, the pressure inside autoclave is increased to 0.3 MPa at first, then temperature is raised from room temperature up to the first isothermal dwell at 80° C. The stacked prepreg is then maintained at 80° C for 20 minutes and heated once again at a heating rate 1° C per minute, up to a second isothermal dwell at 127° C . The stacked prepreg is cured for 120 minutes upon the temperature of 127° C. At the end of the curing dwell, the pressure inside the autoclave is released and the stacking is cooled down to about 55° C in 40 minutes, then the laminate can be taken out from autoclave and be cooled down in ambient condition.

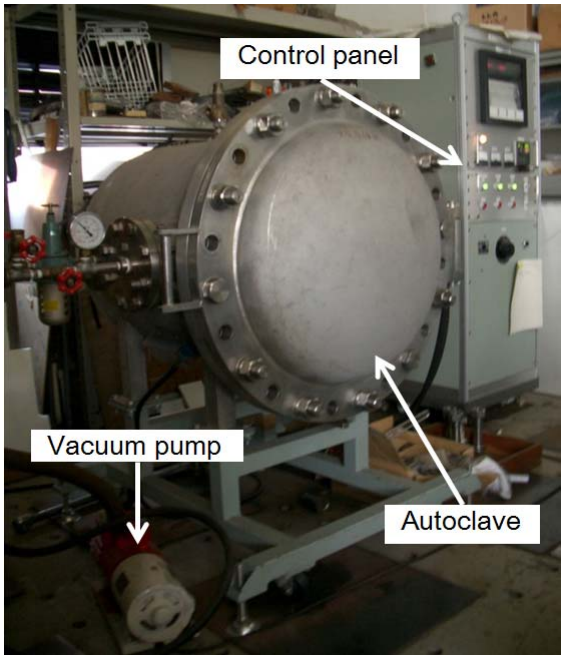

Figure 2-6: Photograph of the autoclave used for curing the UACS laminates.

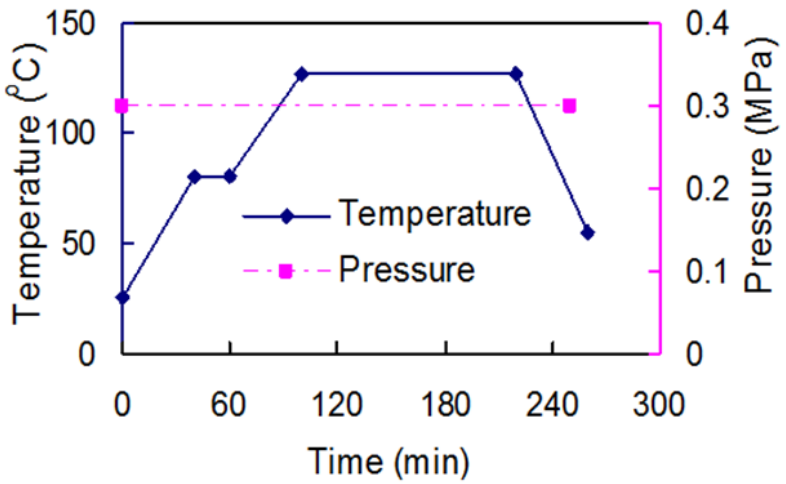

Figure 2-7: Cure cycle recommended by the manufacture of the CFRP prepreg.

It is noted that the main reason of using an autoclave is because we have no such suitable hot-pressing equipment to fabricate a laminate of 250 mm by 250 mm, although in previous studies [1-4] the UACS laminate was cured by hot pressing. Our mini hot-press, purchased a little later, can only make a laminate smaller than 180 mm by 180 mm, and it is used for the fabrication of the specimens for flowability tests as described in the next subsection. Therefore, at such limited situation, specimens with slits of different patterns cured using an autoclave under the same curing condition are useful for the investigation of the effects of the slit patterns on the tensile properties of UACS laminates. As a benchmark, a conventional laminate without slits is also fabricated.

A typical optical micrograph of slits in the prepreg before curing is presented in Fig. 2-8. The width of slits in the prepreg is in the range of 50~100 micrometers. After cure, the slits regions are filled with resin. These resin regions significantly affect the damage progression in UACS laminates, which will be described in detail in next chapter.

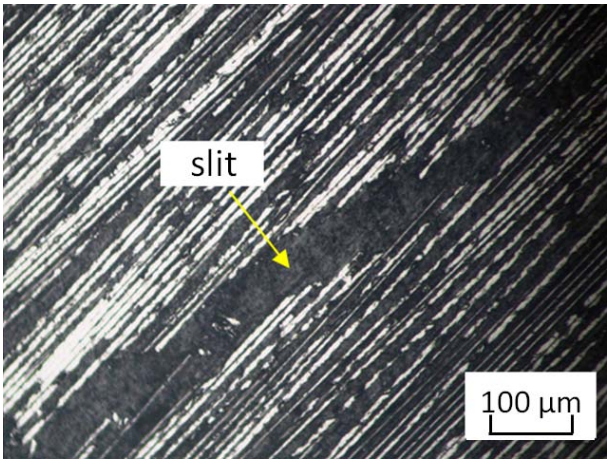

Figure 2-8: Typical optical micrograph of slits cut using a paper cutter.

Typical images of slits in a cured UACS laminate with continuous angled slits are presented in Fig. 2-9. It is seen that the slit may be considered as a resin-rich region, and it is evident from the photos that few fibers debris are embedded into the resin-rich region. It is noted that different dimensions of the slit width in different plies are mainly due to the different angle between the slit and the view direction.

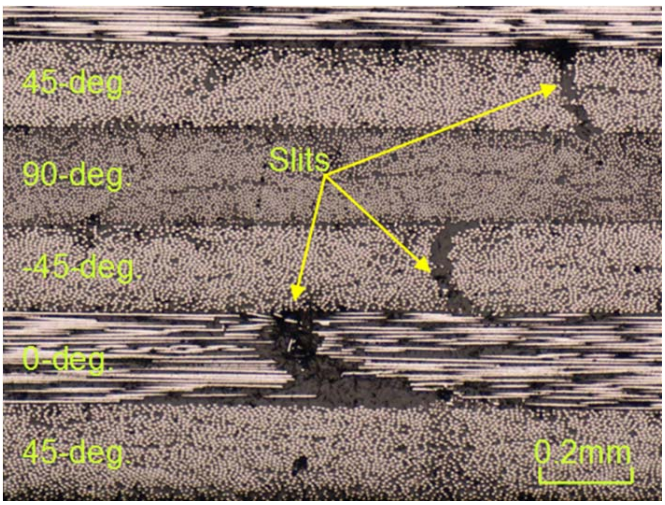

Figure 2-9: Typical images of slits in a cured UACS laminate with continuous angled slits.

From the schematics and optical images of Fig. 2-9, it is easily imagined that large delamination between 0° ply and neighboring plies could occur along the continuous slit due to the stress concentration around the slit if the laminate is loaded in the fiber direction. Compared with continuous slits, staggered slits and bi-angled slits are discontinuous so that delamination could be limited to a certain area even though a stress concentration exists at a small region around the slit ends. Hence, it is expected that new slit patterns may improve the mechanical properties of UACS laminates. Furthermore, the bi-angled slit pattern maintains orthotropic material symmetry of the original prepreg, which is convenient for the design and fabrication of UACS composites.

2.3 Tensile experiment of UACS laminates

Specimens, used for the tensile tests, of 250 mm in length with a 150 mm gauge length, 25 mm in width, and about 3.2 mm in thickness are cut from laminates by using a diamond cutter, as shown in Fig. 2-10. Four glass fiber reinforced polymer (GFRP) tabs with the length of 50mm are adhered at the grip areas in all cases of tensile test specimens.

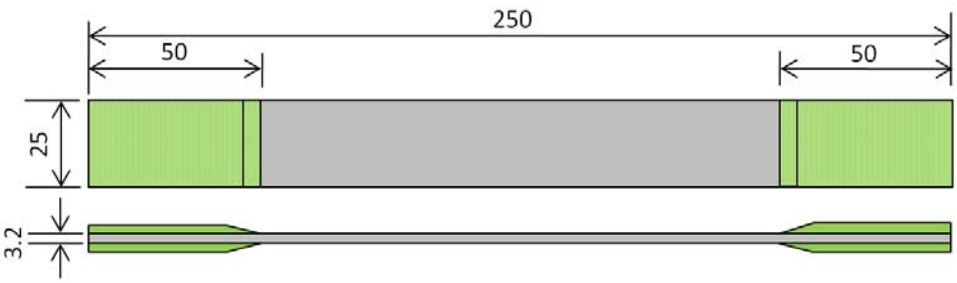

Figure 2-10: Geometry of the specimens for tensile test.

There are at least two slit cycles in the width of the specimen since the horizontal projection of the slit is in the range of L_x = 5~12.5 mm. As a benchmark, specimens cut from a conventional laminate without slits are also fabricated. In total, ten kinds of specimens are cut from ten types of laminates, as summarized in Table 2-1. Four specimens for each kind of laminate are fabricated. Tabs made of conventional glass-fiber cloth/epoxy laminate are bonded on the two sides of the specimen at the grip areas. Strain gauges of 10 mm in length are bonded at the centers of the two surfaces of the specimen. Tensile tests are conducted using a MTS 810 material-testing system and the crosshead speed is 0.5 mm/min. The photograph of MTS 810 material-testing system is presented in Fig. 2-11. In addition, to investigate the failure mechanism of various laminates, tensile tests at the load levels of 90% and 95% of the strength of the laminate are also conducted for UACS laminates of two new slit patterns and existing continuous slit pattern. The side edge of specimens before fracture are polished by sand paper and then observed using optical microscopy to investigate the damage morphology.

Table 2-1: Specimens used for tensile tests.

Specimen	Slit pattern	Projection of slit length
Conventional	without slit	-
Existing	continuous angled slits	-
S(5)	staggered discontinuous angled slits	L_x=5
S(7.5)	staggered discontinuous angled slits	L_x=7.5
S(10)	staggered discontinuous angled slits	L_x=10
S(12.5)	staggered discontinuous angled slits	L_x=12.5
B(5)	discontinuous bi-angled slits	L_x=5
B(7.5)	discontinuous bi-angled slits	L_x=7.5
B(10)	discontinuous bi-angled slits	L_x=10
B(12.5)	discontinuous bi-angled slits	L_x=12.5

Figure 2-11: MTS 810 material-testing system used in the tensile tests of UACS laminates.

2.4 Experimental results and discussions

Results of tensile tests are presented in Fig. 2-12 to Fig. 2-20. Typical stress-strain curves for conventional CFRP laminates and various UACS laminates with L_x = 5 mm are presented in Fig. 2-12. It is seen that the conventional laminate without slits shows a nonlinear behavior near the peak value and that newly designed UACS laminates also show a similar nonlinear behavior near their peak values although the nonlinear range is relatively smaller than that of the conventional laminate. This nonlinear behavior is considered to reflect the damage progress of matrix cracking and delamination before fiber completely breaking of 0° plies, which can be seen in the analysis of fractured specimens later. In contrast, in the case of the existing UACS laminate with continuous slits, stress increases linearly with the increase of strain until failure. This fact means that the final failure of the laminate happens instantaneously with the delamination progressing in the existing UACS laminate with continuous slits. Besides, newly

designed UACS laminates appear to have almost the same tensile modulus as a conventional laminate without slits, which is a little higher than that of the UACS laminate with continuous slits. The reason for this feature is that the in-plane shear stiffness of a UACS ply with continuous angled slits is lower than those of newly designed UACS plies with discontinuous angled slits, which finally lead to a lower tensile modulus of the UACS laminate with continuous angled slits. The tensile strength values of both kinds of newly designed UACS laminates are also higher than the existing UACS laminate with continuous slits.

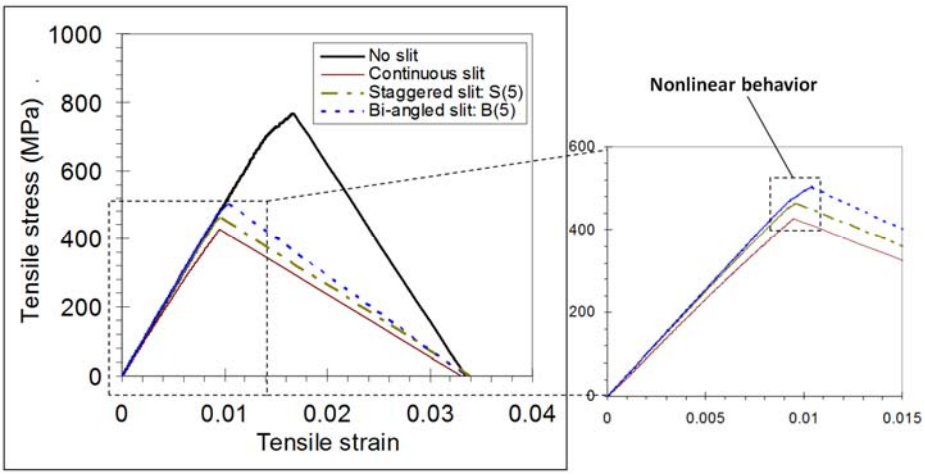

Figure 2-12: Typical stress-strain curves of cured UACS laminate with various slit patterns.

Detailed values of the tensile modulus and strength are given in Fig. 2-13 and Fig. 2-14. Each value in the figure represents the average over four specimens and the error bar indicates the scatter range of test results. Comparing with a laminate without slits, the modulus and strength of UACS laminate with continuous slits reduces by 4.0% and 42.2%, the laminate with staggered slits reduces by 2.6% and 36.5%, and the laminate with bi-angled slits reduces by 0.3% and 33.7%, respectively. Comparing with an existing UACS laminate with continuous slits, newly designed UACS laminates with bi-

angled slits and with staggered slits enhance the tensile strength by 14.7% and 9.9%, respectively. Evidently, out of the three types of laminates studied, the UACS laminate with bi-angled slits gives the best tensile properties among the UACS laminates. It should be noted that in previous research [1, 3] the UACS laminate is cured by hot pressing at 2 MPa pressure, which is much higher than the present curing pressure of 0.3 MPa, so that the thickness of each ply of the UACS laminate changes from original 0.14 mm to 0.1 mm. Hence, the tensile strength of the UACS laminate with continuous 11.3-degree angled slits arrives at almost 80% of that of the conventional laminate without slits and with each ply being 0.14 mm in thickness in [3] because of the significant influence of ply thickness on the tensile strength of UACS laminates. In present paper, all laminates are cured by autoclave at 0.3 MPa pressure and each ply of all laminates is almost the same at about 0.2 mm in thickness. Therefore, the present test results do not contain the influence of ply thickness and only reveal the influence of slit patterns on the tensile properties.

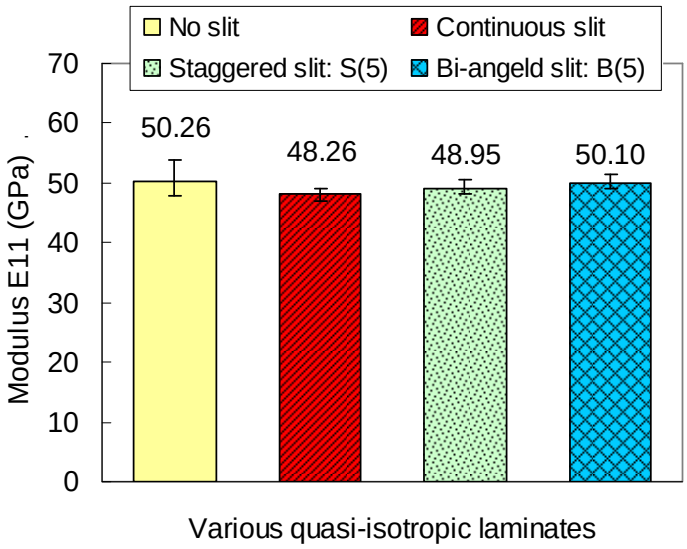

Figure 2-13: Tensile modulus of various quasi-isotropic laminates.

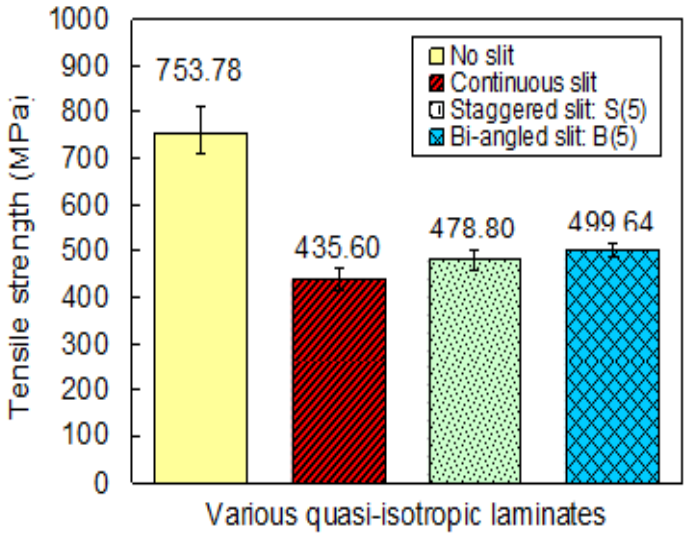

Figure 2-14: Tensile strength of various quasi-isotropic laminates.

Typical images of fractured specimens are shown in Fig. 2-15. In the cases of conventional laminate without slits the breakage of 0° plies dominates the final failure. In newly designed UACS laminates with staggered and bi-angled slit patterns, it is also observed that a few fibers of 0° plies are broken. On the other hand, relatively less fiber breakages are observed in the case of UACS laminate with continuous slits, and the portion of delamination is a little bit higher than the cases of newly designed UACS laminates. These results reveal that effective utilization of the fiber strength of 0° plies can enhance the strength of the laminate. These fiber breakages are supposed to be related to the nonlinear regions of stress-strain curves in Fig. 2-12.

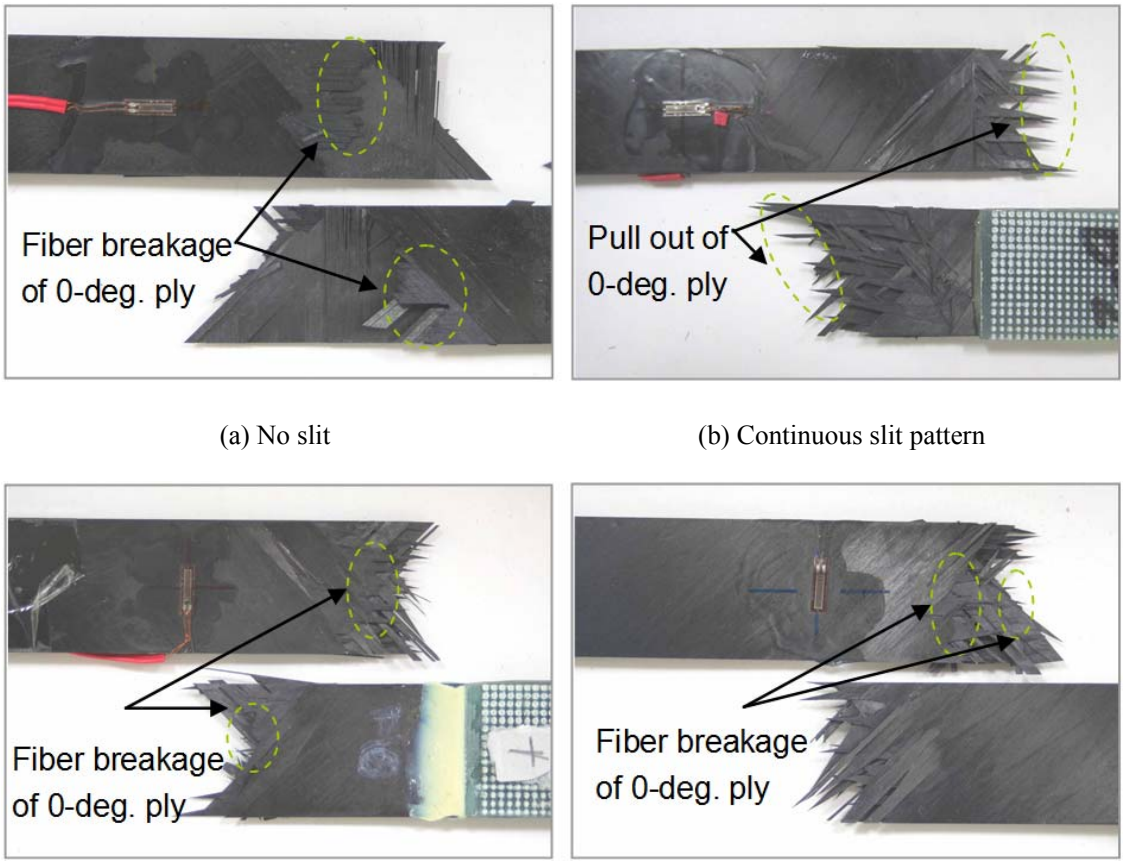

(a) No slit (b) Continuous slit pattern

(c) Staggered slit pattern (d) Bi-angled slit pattern

Figure 2-15: Typical images of fractured specimens of various quasi-isotropic laminates.

To further understand the failure mechanisms of the three types of UACS laminates, the cross-sections of specimens loaded at the load levels of 90% and 95% of the strength are polished and then observed using optical microscopy. Fig. 2-16 shows the polished cross-section images of continuous slit pattern UACS laminate at the load level of 90% of the strength. Damage images in other patterns of UACS laminates display the similar properties. Matrix cracking in the neighboring two 90° plies (8th and 9th) occurs as the initial damage in the whole of laminates to all patterns of UACS. However, this form of damage mode is not the critical damage mode resulting to the final fracture and not

develops to the adjacent plies. The other damage mode observed under this load level is the slit cracking in 0° plies. Crack easily occurs in the slit regions in 0° plies under longitudinal load due that the fibers are cut off in these regions which are filled with resin after cure. Subsequently, significant concentration of shear stresses occurs around the cracked slits between 0° plies and its adjacent plies, which turns to lead to the initiation of the delamination along the interlaminate between 0° plies and its adjacent plies, as shown in Fig. 2-16.

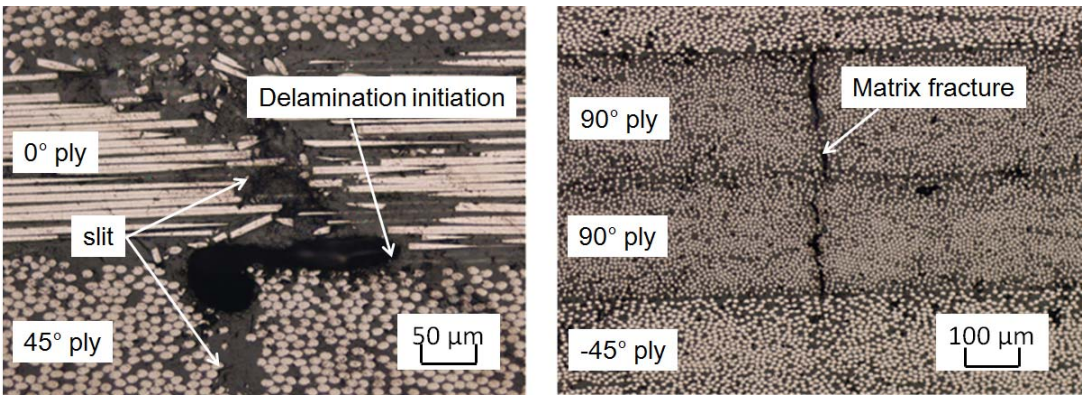

Figure 2-16: Cross-section images of continuous slit pattern UACS laminate at the load level of 90% of the laminate strength.

At the load level of 95%, various damage morphologies are observed, as shown in Fig. 2-17. Relatively more matrix cracks are observed in laminates with two new slit patterns compared to the laminate with continuous slits because the former laminates carry higher load than the latter. On the other hand, relatively large delamination extension from the cracked slit of the 0° ply is observed in the laminate with continuous slits compared to laminates with two new slit patterns. In addition, it is interesting that no crack occurs within the slits of 90° and ±45° plies.

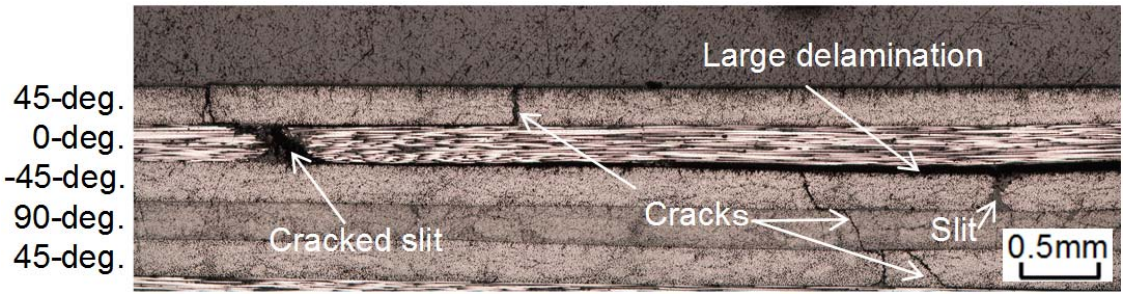

(a) Continuous slit pattern

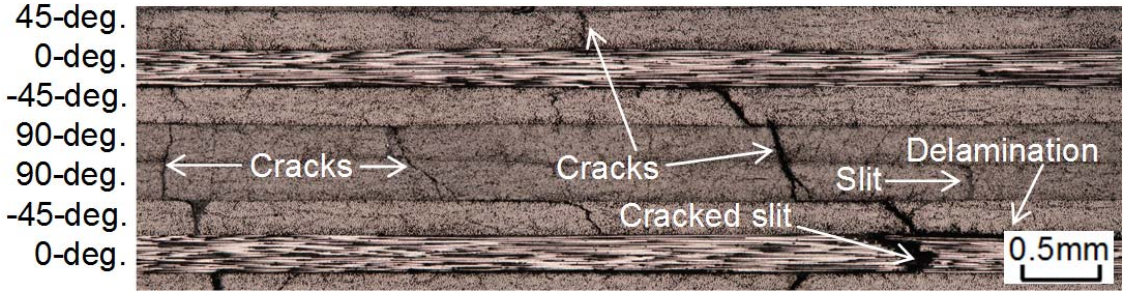

(b) Staggered slit pattern

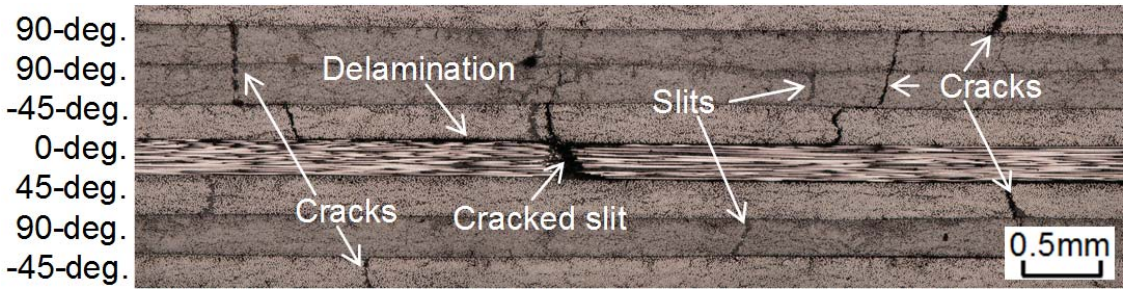

(c) Bi-angled slit pattern

Figure 2-17: Cross-section images of various UACS laminates after tensile test at the load level of 95% of the laminate strength.

Based on the observed results of fractured specimens and specimens loaded at 90% and 95% of the laminate strength, basic damage progress behaviors are schematically depicted in Fig. 2-18. Firstly, 90° plies, 45° plies, and slits in 0° plies crack and then

delamination occurs and progresses between 0° ply and adjacent ±45° plies. Finally, the delamination adjoining matrix cracks leads to the fracture of the specimen. The main difference between UACS laminate with continuous slits and two newly designed UACS laminates is that large delamination develops in the laminate with continuous slits as indicated in the figure by a yellow line and arrows. This schematic image is consistent with Fig. 2-15(b) where many fragments of 0° plies are pulled out due to large delamination. In contrast, delamination occurred in laminates with two new slit patterns stops progressing when it meets the matrix crack so that 0° plies can still carry higher load.

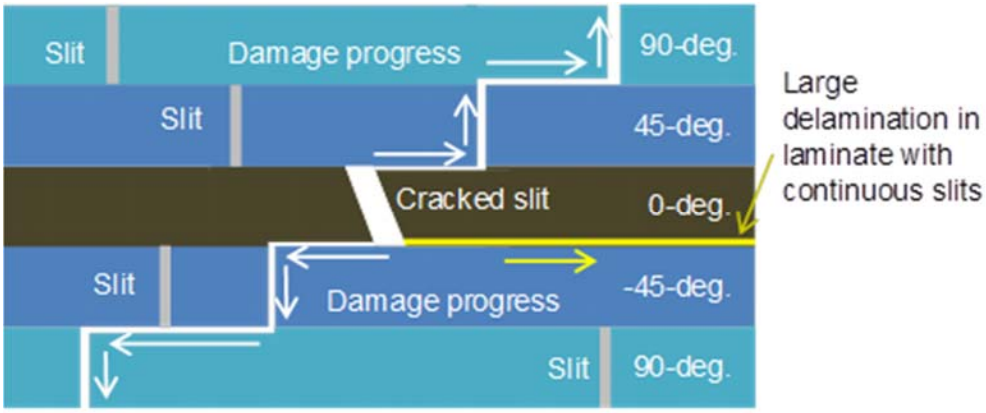

Figure 2-18: Schematic of damage progress for UACS laminates under tension.

Fig. 2-19 presents the distribution schematic of slits in 0° plies and adjacent 45° plies of the three kinds of UACS laminates and the gray and blue lines strand for slits in 0° plies and 45° plies respectively. According to the damage progress analysis under the load level of 95% final load, the delamination develops along slit direction of 0° plies after occurring in the crossing points of slits. To continuous slit pattern UACS, distribution of slits is the most regular and delamination develops most rapidly and

delamination areas are linked together easily. To staggered and bi-angled slit patterns, delamination is inhibited at the tips of discontinuous slits. The delamination development behavior is the main difference of damage progress in UACS laminates with different patterns slit distributions.

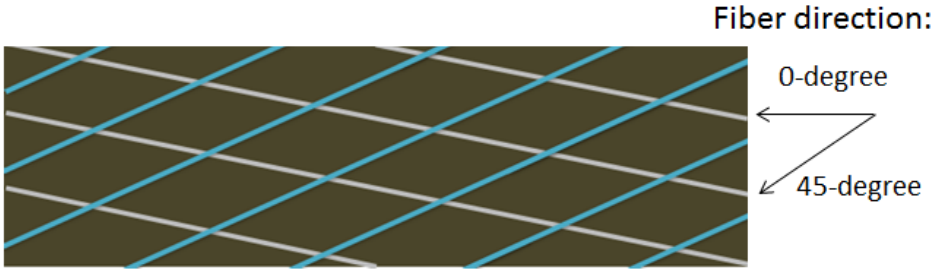

(a) Continuous slit pattern

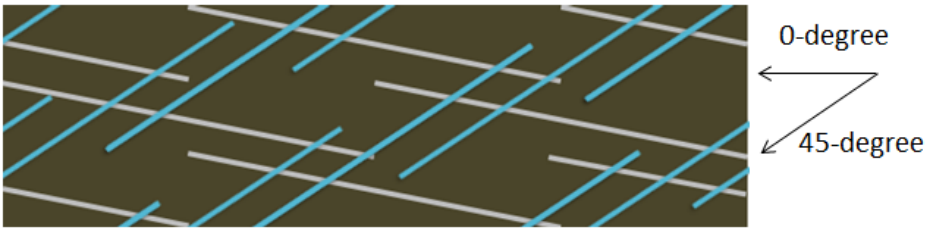

(b) Staggered slit pattern

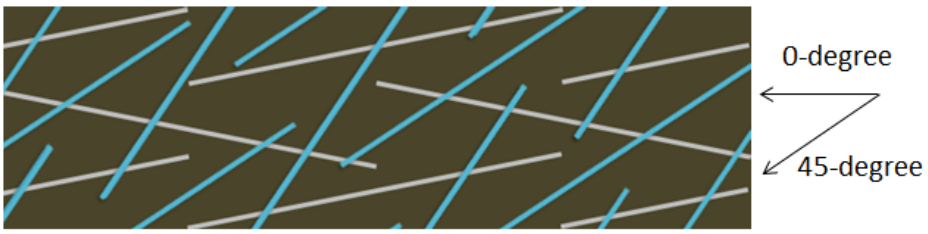

(c) Bi-angled slit pattern

Figure 2-19: Slits distributions of 0° plies and adjacent 45° plies in various UACS laminates.

In conclusion, delamination extension in UACS laminates is quite complicated as indicated in [1, 3]. Further study combined with numerical analysis is necessary to reveal

the failure mechanism of the three kinds of UACS laminates, which will be clarified in the next chapter.

Results associated with the influence of slit length on the tensile properties of laminates with two newly designed slit patterns are presented in Fig. 2-20. Tensile modulus seems to have slight variation, but tensile strength appears to obviously decrease with the increase of slit length.

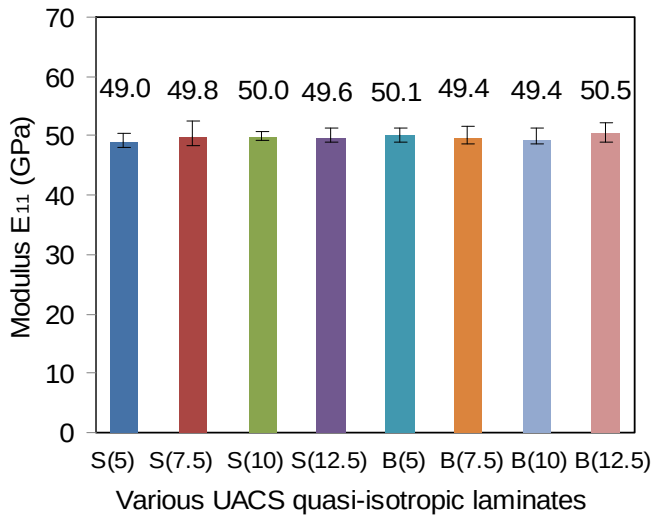

(a) Tensile modulus

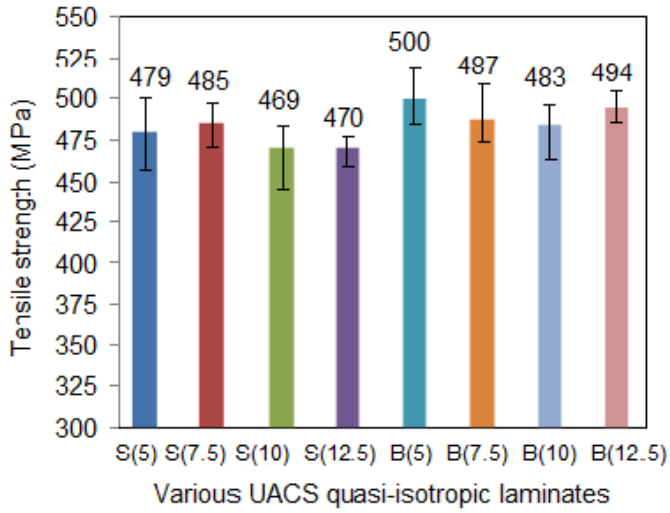

(b) Tensile strength

Figure 2-20: Influence of slit length on the tensile properties of laminates with two new slit patterns.

2.5 Flowability test of UACS lamina

Flowability is significantly important to CFRP in fabricating complexly shaped components. Discontinuous fiber reinforced polymers perform better flowability and formability based on the movement of fibers in curing procedure. SMC is composed of randomly distributed chopped strands and unsaturated thermoset resin and used for compression molding in many engineering fields. Complexly shaped products can be easily fabricated using SMC due to its good flowability during molding.

As introduced in subsection 1.4, previous UACS have superior flowability, which is displayed in previous researches [1, 4]. The area of UACS laminate is increased by 31% after cure at the pressure of 3 MPa. In addition, a rib structure fabricated by UACS plies revealed that the chopped strands sufficiently filled the rib part and nearly no resin-rich regions are been observed.

2.5.1 Flowability test procedures

In this study, in order to investigate the flowability of the two newly designed UACS laminates, hybrid laminates of [90/0/90] are fabricated using one 0° UACS ply and two 90° unidirectional glass-fiber/epoxy plies without slits, as shown in Fig. 2-21.

The unidirectional glass-fiber/epoxy prepreg (E16-35) is provided by Kanae Corporation. The thickness of glass-fiber/epoxy prepreg is 0.14 mm, and fiber volume fraction is about 63%. The present newly designed UACS plies with slit length parameter L_x = 5 mm and existing UACS ply with continuous slits are employed as UACS ply. At first, glass-fiber/epoxy plies and three types of UACS plies with slits are cut into circles

of 100 mm in diameter, respectively. Then, each of three UACS plies is inserted between two glass-fiber/epoxy plies to stack a [90/0/90] hybrid laminate.

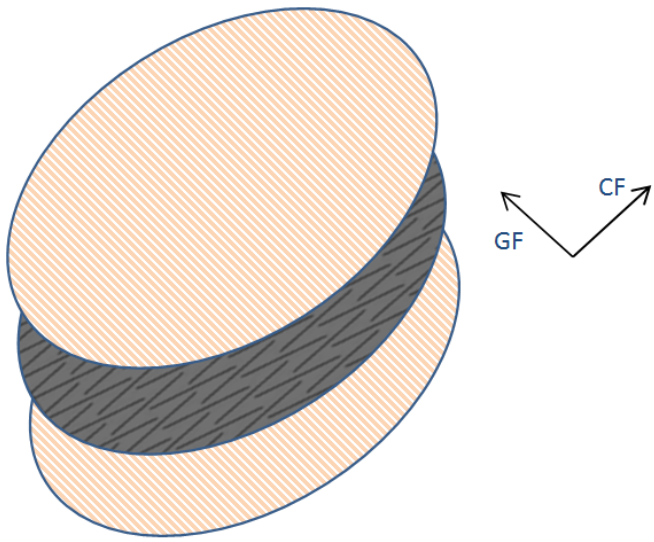

Figure 2-21: Stacking schematic of hybrid laminate (first and third plies: glass-fiber plies; second ply: bi-angled slit pattern UACS ply).

The stacked plies are cured by a mini hot pressing which is shown in Fig. 2-22 at 2 MPa pressure and 150ºC for 10 minutes. Three specimens are fabricated for each kind of UACS prepreg. Since the glass-fiber/epoxy ply is transparent after cure and the continuous glass fibers can restrict the flow of the laminate in the transverse direction during curing process, we can investigate the flowability of the UACS ply in the fiber direction due to the existence of slits by analyzing the geometrical change of the hybrid laminate after cure.

Figure 2-22: Photograph of mini hot-pressing equipment used in flowability test of UACS laminas.

Flowability tests are conducted during the curing process of three kinds of [90/0/90] hybrid laminates by hot pressing at 2 MPa pressure and 150º C for 10 min. After cure, the geometrical changes of the UACS plies in three kinds of hybrid laminates are investigated by analyzing the variation of geometry along 0° and 90° directions. Three specimens are tested for each kind of UACS prepreg. From the difference of geometrical changes of three UACS plies, we can evaluate the flowability of each UACS ply.

2.5.2 Flowability tests results

As mentioned before, the flowability test is conducted during the curing process of the hybrid laminate by hot pressing. After cure, the glass-fiber plies become transparent, which enables us to see the UACS ply in the middle plane clearly. Typical images of

three cured hybrid laminates are presented in Fig. 2-23. In each photo, the dashed line denotes the original circle of each hybrid laminate and the solid line indicates the geometry of each deformed hybrid laminate after cure. Some of the material for each of the UACS plies flows out of the glass-fiber/epoxy plies in the glass ply's fiber direction, although the glass-fiber/epoxy ply without slits constrains the flow of UACS ply along the glass fiber direction. The diameter of longitudinal axis of the ellipses of each hybrid laminate is utilized to evaluate the flowability of each UACS ply. The values of the longitudinal axis of three UACS plies, namely, ply with continuous slits, ply with staggered slits, and ply with bi-angled slits, are 116mm, 119mm and 123mm, which correspond to the extension rates of 16%, 19% and 23%, respectively. In addition, several transparent areas can be seen near the boundary region in the cases of UACS plies with continuous slits and with staggered slits. Additional two tests for each kind of UACS ply show similar results. The average extension rate over the three specimens is 16.7%, 20.3%, 22.7% for three kinds of UACS plies, respectively. From these results, it is recognized that the UACS ply with bi-angled slits appears to have the highest degree of flowability and uniformity.

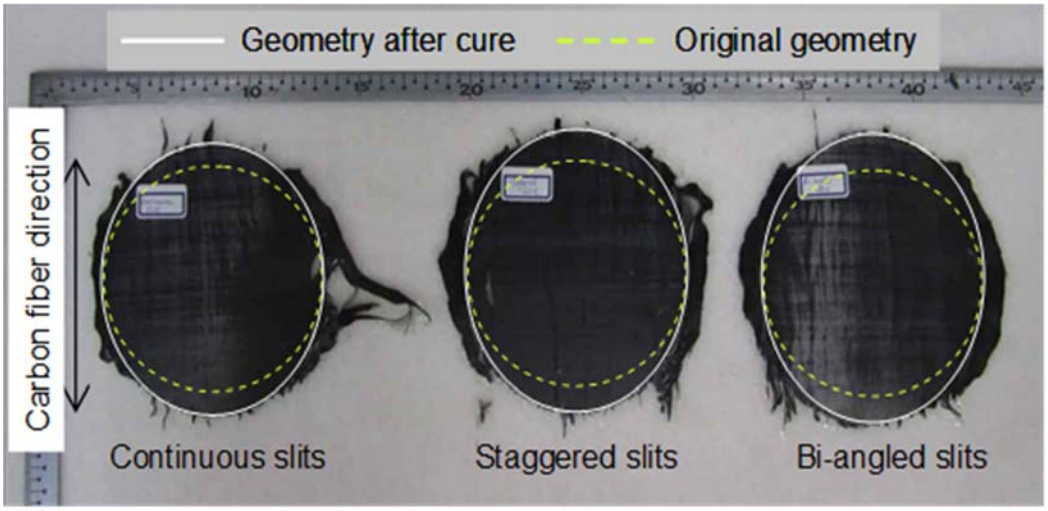

Figure 2-23: Images of three [90/0/90] hybrid laminates after cure.

2.6 Summary

In this chapter, two new designs of UACS laminates are proposed to improve the strength and material symmetry of existing UACS laminates by introducing discontinuous angled slits into prepreg made of continuous CFRP. A hand-made fabrication method for new UACS prepregs is introduced. Tensile tests on quasi-isotropic laminates fabricated by UACS prepregs with three slit patterns and the conventional quasi-isotropic laminate without slits are conducted. Flowability tests on [90/0/90] hybrid laminates with two 90° glass-fiber/epoxy plies and one 0° UACS ply are performed for UACS prepregs of three slit patterns. Based on the test results, the following conclusions are obtained.

1. Newly designed UACS laminates with staggered discontinuous angled slits and with discontinuous bi-angled slits enhance the tensile strength by about 10% and 15%

comparing with the existing UACS laminate with continuous angled slits. The UACS laminate with discontinuous bi-angled slits has the best tensile mechanical properties.

2. The three kinds of UACS laminates appear to have different failure morphologies. Certain fiber breakages of 0° plies are observed in the case of two newly designed UACS laminates, but relatively less fiber breakages are observed in the case of existing UACS laminate with continuous slits and the portion of delamination is a little bit higher than the cases of newly designed UACS laminates. Further study is necessary to clarify the failure mechanisms of the three kinds of UACS laminates.

3. Slit length has obvious influence on the tensile strength of UACS laminates with two newly designed slit patterns. Long slits lead to low tensile strength. However, the influence of slit length on the tensile modulus is limited.

4. Newly designed UACS laminates have better flowability than the existing UACS laminate with continuous angled slits. The UACS laminate with discontinuous bi-angled slits appears to have the best flowability and uniformity.

Bibliography

[1] Taketa I, Okabe T, Kitano A. A new compression-molding approach using unidirectionally arrayed chopped strands. *Composites Part A: Applied Science and Manufacturing,* 2008; 39(12): 1884–1890.

[2] Taketa I, Okabe T, Kitano A. Strength improvement in unidirectional arrayed chopped strands with interlaminar toughening. *Composites Part A: Applied Science and Manufacturing,* 2009; 40(8): 1174–1178.

[3] Taketa I, Sato N, Kitano A, Nishikawa M, Okabe T. Enhancement of strength and uniformity in unidirectionally arrayed chopped strands with angled slits. *Composites Part A: Applied Science and Manufacturing,* 2010; 41(11): 1639–1646.

[4] Taketa I, Okabe T, Matsutani H, Kitano A. Flowability of unidirectionally arrayed chopped strands in compression molding. *Composites Part B: Engineering,* 2011; 42(6): 1764–1769.

CHAPTER 3

Multiscale analysis of damage progression in newly designed UACS laminates

In this chapter, the damage progression in laminates fabricated by unidirectionally arrayed chopped strands (UACS) with newly designed slit distribution patterns under tension is simulated based on a multiscale analysis. The multiscale analysis includes a homogenization analysis and a multiscale damage progression analysis of a microscopic region and a macroscopic region. Cohesive interface element and maximum stress criterion are employed for the simulation of the progression of delamination and other failure modes in the laminates, respectively.

3.1 Introduction

As a new option of short fiber reinforced composites, UACS laminates are expected to be applied to the primary and secondary structural components of automobiles. Therefore, clarifying the effects of slit distribution patterns on the damage progression is very important from the viewpoint of the design of the structural components using UACS laminates. It is a complicated subject how to accurately analyze the damage progression in the discontinuous fiber reinforced composites because of the complexity of the microstructure of the composites [1, 2]. Lee and Simunovic [3, 4] proposed a micromechanical damage constitutive model to analyze the progressive damage in aligned and randomly oriented discontinuous fiber composites. However, the interaction among fibers is not considered in the model and the laminated composites are not included. Yashiro and Ogi performed an analysis of a CFRP cross-ply laminate with initially cut fibers [5]. The effects of the initially cut fibers on the fracture behavior of the laminate were discussed. However, the cross-ply laminate only has several slits in partial plies, which is different from the UACS laminates with many slits in all plies.

In this chapter, a multiscale analysis based on finite element method (FEM) is implemented to clarify the damage progression in the UACS quasi-isotropic laminates and the effects of the slit distribution patterns. The present multiscale analysis consists of a homogenization analysis and a damage progression analysis of a multiscale model including a microscopic region and a macroscopic region. The homogenization analysis is employed to calculate the elastic constants of the laminas with various silt distribution patterns used for the macroscopic region. In the microscopic region, the silt distribution is precisely simulated, cohesive interface element is employed to simulate the

delamination progression between the 0° ply and its adjacent plies, and maximum stress criterion is adopted to describe the various failure scenarios such as slit cracking, matrix cracking, and fiber breakage in the laminas.

3.2 Multiscale FEM models of UACS laminates for damage progression analysis

From the UACS prepreg schematics shown in Fig. 2-3, it is easily imagined that the microstructure of a UACS laminate $[45/0/-45/90]_{2S}$ is very complex due to the existence of the slits. Therefore, it is difficult to precisely simulate the microstructure of silt distribution through the whole specimens in the analysis of damage progression of the UACS laminates from the viewpoint of the computational cost. For this reason, a multiscale FEM analysis model, as depicted in Fig. 3-1, is considered. This model represents the central region in the gauge length of the tensile specimens used in the previous experimental described in chapter 2, it is 25 mm in length, 25 mm in width, and 3.2 mm in thickness, and it consists of top four microscopic plies and lower three macroscopic layers for the simulation of a quasi-isotropic UACS laminate $[45/0/-45/90]_{2S}$. The top four plies precisely model the slit patters in the UACS laminas.

The images of the slit distribution in the top four plies of the UACS laminate is presented in Fig. 3-2. The slits of 0.1 mm in width are filled with epoxy resin as revealed in previous experiment and the material surrounding the slits is CFRP. Cohesive interface elements are inserted into the interface 1 between 45° and 0° plies and the interface 2 between 0° and -45° plies to simulate the delamination initiation and extension. The material properties of the CFRP and epoxy resin are given in Table 3-1, and the bilinear constitutive constants of the cohesive interface element [5] are given in Table 3-2, respectively. The lower three macroscopic layers describe three homogeneous

laminates including one [45/0/-45/90] and two [90/-45/0/45]. It is known that in the most real tensile tests the failure often occurs asymmetrically to the mid-plane in a laminate even though the laminate is a symmetrical laminate since the failure is very sensitive not only to the macroscale structure but also to the real microscale structure which is generally not perfectly symmetrical. Thus, in the present study, an asymmetrical model, shown in Fig. 3-1, is adopted as the first trial.

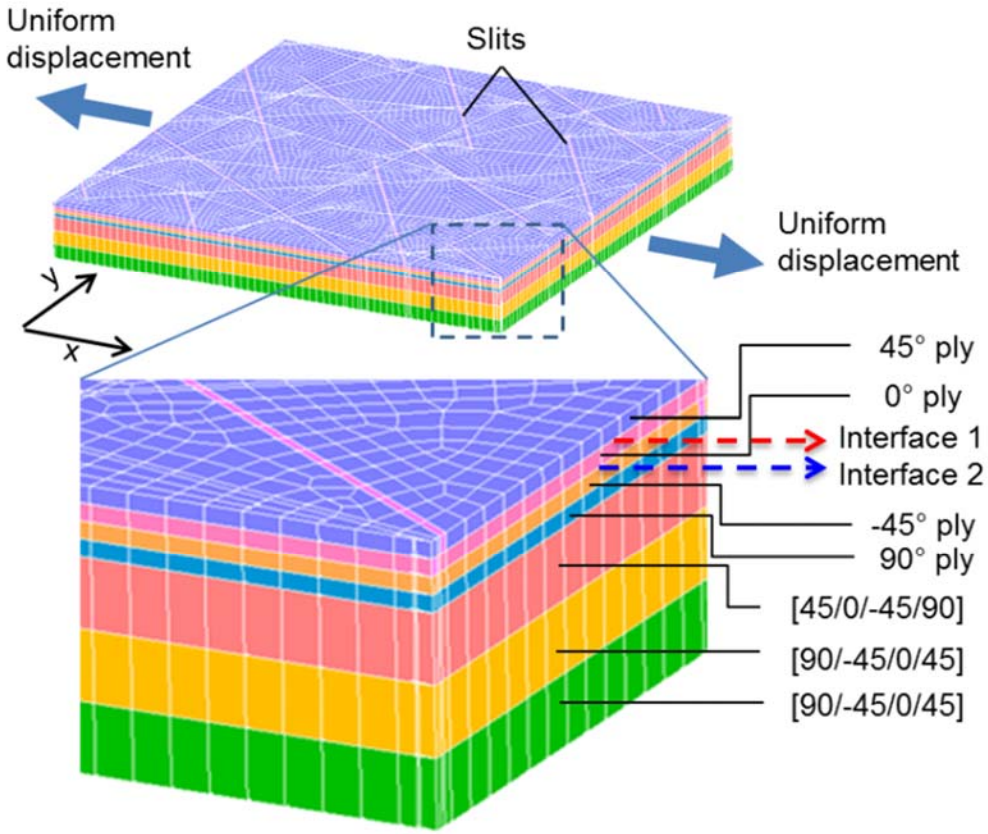

Figure 3-1: A multiscale FEM model for the UACS laminate with bi-angled slits.

Table 3-1: Material properties of the CFRP and the epoxy resin.

CFRP	
Longitudinal Young's modulus E_1 (GPa)	142
Transverse Young's modulus $E_2 = E_3$ (GPa)	8.8
In-plane shear modulus $G_{12} = G_{31}$ (GPa)	4.2
Out-of-plane shear modulus G_{23} (GPa)	3.7
In-plane Poisson's ratio ν_{12}	0.27
Out-of-plane Poisson's ratio ν_{23}	0.32
Longitudinal tensile strength X_t (MPa)	2950
Longitudinal compression strength X_c (MPa)	1570
Transverse tensile strength $Y_t = Z_t$ (MPa)	79
Transverse compression strength $Y_c = Z_c$ (MPa)	190
In-plane shear strength $S_{12} = S_{31}$ (MPa)	140
Out-of-plane shear strength S_{23} (MPa)	88
Epoxy resin	
Young's modulus E (GPa)	4
Poisson's ratio ν	0.35
Tensile strength (MPa)	79
Compression strength (MPa)	190
Shear strength (MPa)	88

In the present study, the multiscale analysis includes mainly two steps. The first step is the homogenization analysis for the calculation of the effective stiffness constants of the UACS laminas used in the three macroscopic layers (Fig. 3-1), which is described in the next subsection. Then the stiffness constants of three macroscopic layers are calculated using these effective stiffness constants and classical lamination theory. The second step is the damage progression analysis using the multiscale FEM model, which is described in the subsection 3.4 later.

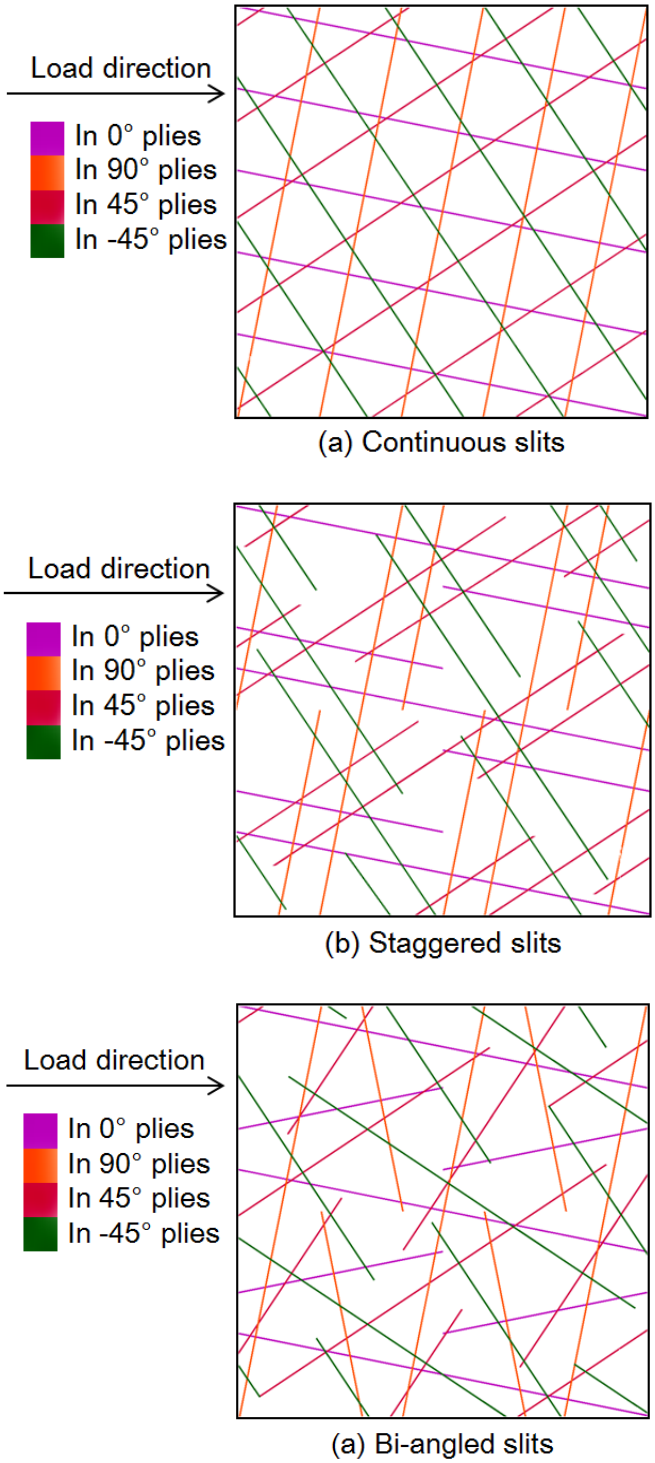

Figure 3-2: Illustration of the distribution of slits in the top four plies of the multiscale model for the UACS laminates.

3.3 Homogenization analysis

It is extremely difficult in analyzing a composite material with complex material heterogeneity involving with individual components due to the huge computational time and cost. Many researches have been focused on exploring an approximate and efficient analysis method. Several methods have been developed in past few decades to predict the macroscopic properties and microscopic mechanical behaviors of various composites. The homogenization method has been developed based on the mathematically multiscale perturbation theory by Benssousan et al, [6], Sanchez-Palencia [7], Bakhvalov and Panasenko [8], Bendsoe and Kikuchi [9], Guedes and Kikuchi [10], Hassani and Hinton [11], and others. This method can predict not only the macroscopic material properties but also the microscopic mechanical behaviors of various composites and porous materials with the help of FEM. In the case of homogenization method, a characteristic function of the third order tensor is introduced to relate the microscopic displacements to the macroscopic displacements, which make it possible to express the exact periodic conditions formally along the boundary of a basic cell.

3.3.1 Formulation of homogenization analysis

Consider a linearly elastic body with a periodic microstructure, as shown in Fig. 3-3. Ω denotes the open subset of three-dimensional space occupied by the body, Γ the boundary of Ω, Y the open subset of the space occupied by the basic unit cell, S_Y the boundary of Y. The sub-domain Y_2 may represent an inclusion in the unit cell to describe a composite, or a void to describe a porous material. Define S_{y12} as the interface

when Y_1 and Y_2 are different materials, or as the internal boundary of Y_1 when Y_2 represents a void. For the sake of simplicity, it is assumed that S_{Y12} is a traction-free surface if Y_2 represents a void. Referring to Fig. 3-3, it is observed that the solution of this boundary value problem varies not only on the macroscopic scale x with a Y-periodicity, but also varies rapidly within the unit cell on the microscopic scale y. It is hard to solve such a problem directly by the conventional FEM since the computational quantity becomes enormous in order to describe the individual microstructures precisely. The homogenization method was developed to solve such problems approximately based on the mathematically multi-scale perturbation theory. A brief review of the basic equations is given in this subsection according to Guedes and Kikuchi [10], Hassani and Hinton [11], and Jansson [12].

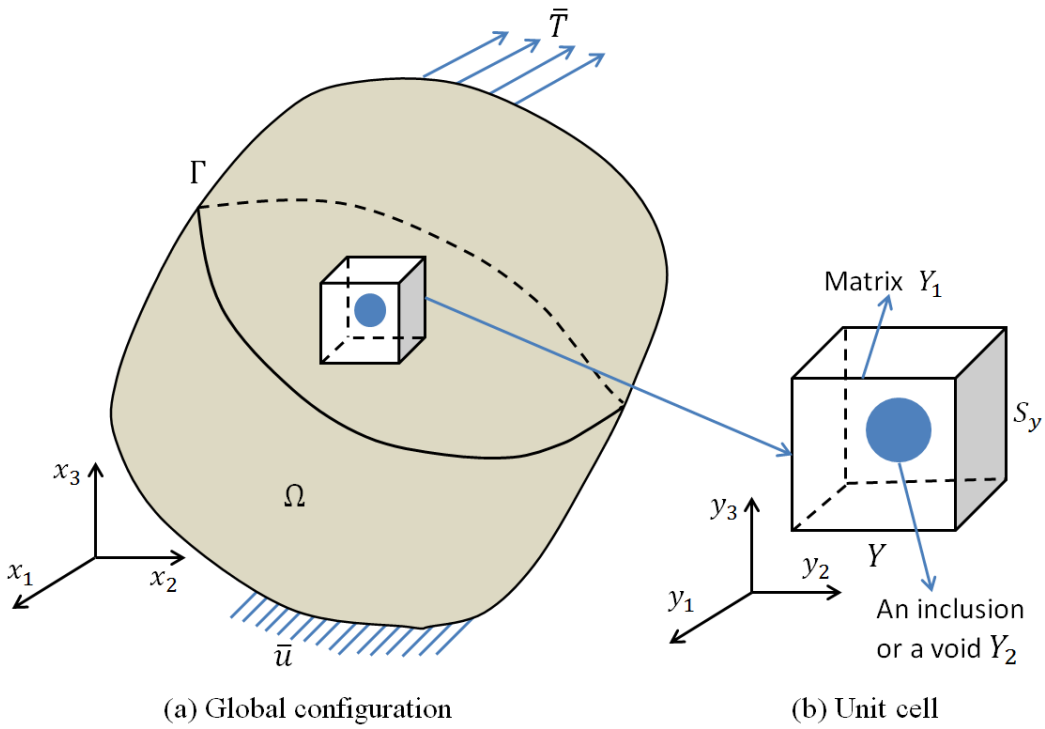

Figure 3-3: Illustration of an elasticity problem of a material with periodic microstructures.

In the construction of the homogenization theory, the displacements $u_i(\mathbf{x})$ are assumed as an asymptotic expansion with respect to a parameter η that is a scaling factor of the microscopic/macroscopic dimension, i.e.

$$u_i(\mathbf{x}) = u_i^0(\mathbf{x},\mathbf{y}) + \eta u_i^1(\mathbf{x},\mathbf{y}) + \eta^2 u_i^2(\mathbf{x},\mathbf{y}) + \cdots \qquad \text{(Eq. 3-1)}$$

Where $\mathbf{x} = (x_1, x_2, x_3)$ and $\mathbf{y} = (y_1, y_2, y_3)$ represent the macroscopic and the microscopic coordinate systems, respectively, which are related to each other by

$$y_i = \frac{x_i}{\eta} \qquad \text{(Eq. 3-2)}$$

Then, based on the elasticity, the strain-displacement and stress-strain relations can be expressed as

$$\varepsilon_{ij} = \frac{1}{2}\left(\frac{\partial u_i}{\partial x_j} + \frac{\partial u_j}{\partial x_i}\right), \qquad \sigma_{ij} = E_{ijkl}\varepsilon_{kl} \qquad \text{(Eq. 3-3)}$$

Where ε_{kl} , σ_{ij} represent strain and stress tensors, respectively, and E_{ijkl} denotes the elastic constants tensor. Applying the following chain rule of differentiation of a function with implicit variables

$$\frac{\partial \Phi(\mathbf{x},\mathbf{y}=\mathbf{x}/\eta)}{\partial x_i} = \frac{\partial \Phi(\mathbf{x},\mathbf{y})}{\partial x_i} + \frac{\partial \Phi(\mathbf{x},\mathbf{y})}{\partial y_k}\frac{\partial y_k}{\partial x_i} = \frac{\partial \Phi(\mathbf{x},\mathbf{y})}{\partial x_i} + \frac{1}{\eta}\frac{\partial \Phi(\mathbf{x},\mathbf{y})}{\partial y_i} \qquad \text{(Eq. 3-4)}$$

to the partial differentials of the strain-displacement and stress-strain relations yields

$$\begin{aligned}\varepsilon_{ij} = {} & \frac{1}{2\eta}\left(\frac{\partial u_i^0}{\partial y_j} + \frac{\partial u_j^0}{\partial y_i}\right) + \frac{1}{2}\left[\left(\frac{\partial u_i^0}{\partial x_j} + \frac{\partial u_j^0}{\partial x_i}\right) + \left(\frac{\partial u_i^1}{\partial y_j} + \frac{\partial u_j^1}{\partial y_i}\right)\right] + \\ & \frac{\eta}{2}\left[\left(\frac{\partial u_i^1}{\partial x_j} + \frac{\partial u_j^1}{\partial x_i}\right) + \left(\frac{\partial u_i^2}{\partial y_j} + \frac{\partial u_j^2}{\partial y_i}\right)\right] + \cdots\end{aligned} \qquad \text{(Eq. 3-5)}$$

$$\sigma_{ij} = \frac{1}{\eta} E_{ijkl} \frac{\partial u_k^0}{\partial y_l} + E_{ijkl} (\frac{\partial u_k^0}{\partial x_l} + \frac{\partial u_k^1}{\partial y_l}) + \eta E_{ijkl} (\frac{\partial u_k^1}{\partial x_l} + \frac{\partial u_k^2}{\partial y_l}) + \cdots \qquad \text{(Eq. 3-6)}$$

According to the elasticity, the virtual displacement equation can be expressed as:

$$\int_\Omega E_{ijkl} \frac{\partial u_k}{\partial x_l} \frac{\partial v_i}{\partial x_j} d\Omega = \int_\Omega f_i v_i d\Omega + \int_{\Gamma_T} \overline{T}_i v_i d\Gamma \qquad \text{(Eq. 3-7)}$$

Where Γ_T denotes the region of the boundary Γ with specified tractions $\overline{T}_i$, v_i is the virtual displacement and $v_i = 0$ on the Γ_u where $u_i = \overline{u}_i$, f_i is the body force. By inserting Eq. 3-1 into the above virtual displacement equation, applying the chain rule of differentiation to the partial differentials of u_k and v_i, and equating the terms with the same power of η, we can derive a series of equations related to the displacements u_i^0, u_i^1, u_i^2 and so on as follows.

$$u_i^0(\mathbf{x}, \mathbf{y}) = u_i^0(\mathbf{x}) \qquad \text{(Eq. 3-8)}$$

$$\int_Y E_{ijkl} \left(\frac{\partial u_k^0(\mathbf{x})}{\partial x_l} + \frac{\partial u_k^1(\mathbf{x}, \mathbf{y})}{\partial y_l} \right) \frac{\partial v_i(\mathbf{y})}{\partial y_j} dY = 0 \qquad v_i \in Y \qquad \text{(Eq. 3-9)}$$

$$\int_\Omega [\frac{1}{|Y|} \int_Y E_{ijkl} (\frac{\partial u_k^0(\mathrm{x})}{\partial x_l} + \frac{\partial u_k^1(\mathrm{x}, \mathrm{y})}{\partial y_l}) dY] \frac{\partial v_i(\mathrm{x})}{\partial \mathrm{x_j}} d\Omega =$$

$$\int_\Omega (\frac{1}{|Y|} \int_Y f_i dY v_i(\mathbf{x}) d\Omega + \int_{\Gamma_T} \overline{T}_i v_i(\mathbf{x}) d\Gamma \qquad v_i \in \Omega \qquad \text{(Eq. 3-10)}$$

$$\int_Y E_{ijkl} \left(\frac{\partial u_k^1(\mathbf{x})}{\partial x_l} + \frac{\partial u_k^2(\mathbf{x}, \mathbf{y})}{\partial y_l} \right) \frac{\partial v_i(\mathbf{y})}{\partial y_j} dY = \int_Y f_i v_i(\mathbf{y}) dY \qquad v_i \in Y \qquad \text{(Eq. 3-11)}$$

etc.

Theoretically, solving all the above equations together with specified boundary conditions will yields the full solution for u_i^0, u_i^1, $u_i^2, \cdots$. However, the first order

approximation of $u_i(\mathbf{x})$ is usually of interest for many practical applications. Then only two equations of Eq. 3-9 and Eq. 3-10 related to u_i^0 and u_i^1 need to be solved.

In the conventional solution method for the homogenization analysis, it is assumed that

$$u_k^1(\mathbf{x},\mathbf{y}) = -\chi_k^{pq}(\mathbf{x},\mathbf{y})\frac{\partial u_p^0(\mathbf{x})}{\partial x_q} + \tilde{u}_k^1(\mathbf{x}) \qquad \text{(Eq. 3-12)}$$

where χ_k^{pq}, called as characteristic function, is an unknown *Y*- periodic tensor of the third order. It is noted that χ_k^{pq} may also be considered as a symmetric tensor of the second order for each *k* (*k* = 1, 2, 3). Inserting Eq. 3-12 into Eq. 3-9 leads to

$$\int_Y \left(E_{ijkl}\frac{\partial u_k^0(\mathbf{x})}{\partial x_l} - E_{ijkl}\frac{\partial \chi_k^{pq}(\mathbf{x},\mathbf{y})}{\partial y_l}\frac{\partial u_p^0(\mathbf{x})}{\partial x_q}\right)\frac{\partial v_i(\mathbf{y})}{\partial y_j}dY = 0 \qquad \text{(Eq. 3-13)}$$

Since $u_p^0(\mathbf{x})$ is independent of **y** and

$$E_{ijkl}\frac{\partial \chi_k^{pq}(\mathbf{x},\mathbf{y})}{\partial y_l}\frac{\partial u_p^0(\mathbf{x})}{\partial x_q} = E_{ijpq}\frac{\partial \chi_p^{kl}(\mathbf{x},\mathbf{y})}{\partial y_q}\frac{\partial u_k^0(\mathbf{x})}{\partial x_l} \qquad \text{(Eq. 3-14)}$$

Eq. 3-3 is identically equal to

$$\int_Y E_{ijpq}\frac{\partial \chi_p^{kl}(\mathbf{x},\mathbf{y})}{\partial y_q}\frac{\partial v_i(\mathbf{y})}{\partial y_j}dY = \int_Y E_{ijkl}\frac{\partial v_i(\mathbf{y})}{\partial y_j}dY \qquad \text{(Eq. 3-15)}$$

that is, χ_k^{pq} is the solution of the above inhomogeneous integral equation. In other words, χ_k^{pq} can be obtained by solving Eq. 3-15 together with the *Y*-periodic conditions of $u_k^1(\mathbf{x},\mathbf{y})$ $(k = 1,2,3)$. For example, if the unit cell is a rectangular parallelepiped, as shown in Fig. 3-4, the six faces of the rectangular parallelepiped can be described by

$$(y_1, y_2, y_3)\Big|_{\substack{face1\\face3}} = (\mp\frac{a}{2}, y_2, y_3), \quad (y_1, y_2, y_3)\Big|_{\substack{face2\\face4}} = (y_1, \mp\frac{b}{2}, y_3),$$

$$(y_1, y_2, y_3)\Big|_{\substack{face5\\face6}} = (y_1, y_2, \mp\frac{c}{2})$$

(Eq. 3-16)

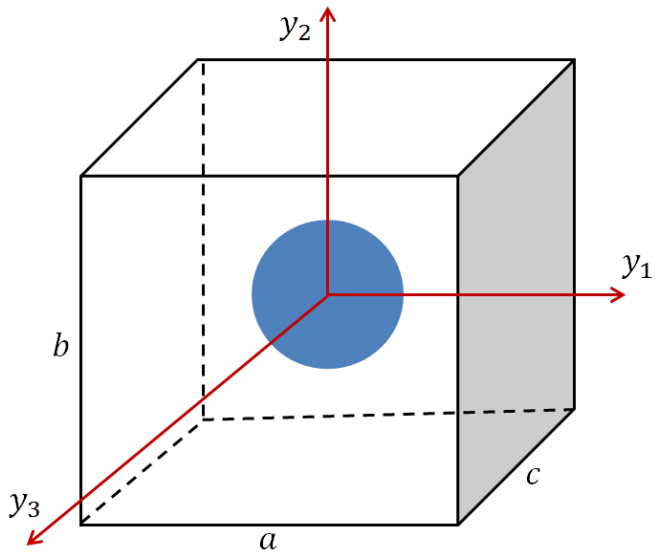

Figure 3-4: A rectangular parallelepiped unit cell.

Then the periodic boundary conditions of $u_k^1(\mathbf{x},\mathbf{y})$ require

$$u_k^1(\mathbf{x},\mathbf{y})\Big|_{face1} = u_k^1(\mathbf{x},\mathbf{y})\Big|_{face3}, \; u_k^1(\mathbf{x},\mathbf{y})\Big|_{face2} = u_k^1(\mathbf{x},\mathbf{y})\Big|_{face4},$$

$$u_k^1(\mathbf{x},\mathbf{y})\Big|_{face5} = u_k^1(\mathbf{x},\mathbf{y})\Big|_{face6}$$

(Eq. 3-17)

Inserting Eq. 3-2 into the above equations leads to

$$\left[-\chi_k^{pq}(\mathbf{x},\mathbf{y})\frac{\partial u_p^0(\mathbf{x})}{\partial x_q} + \tilde{u}_k^1(\mathbf{x})\right]\Big|_{face1} = \left[-\chi_k^{pq}(\mathbf{x},\mathbf{y})\frac{\partial u_p^0(\mathbf{x})}{\partial x_q} + \tilde{u}_k^1(\mathbf{x})\right]\Big|_{face3}$$

$$\left[-\chi_k^{pq}(\mathbf{x},\mathbf{y})\frac{\partial u_p^0(\mathbf{x})}{\partial x_q} + \tilde{u}_k^1(\mathbf{x})\right]\Big|_{face2} = \left[-\chi_k^{pq}(\mathbf{x},\mathbf{y})\frac{\partial u_p^0(\mathbf{x})}{\partial x_q} + \tilde{u}_k^1(\mathbf{x})\right]\Big|_{face4}$$

$$\left[-\chi_k^{pq}(\mathbf{x},\mathbf{y})\frac{\partial u_p^0(\mathbf{x})}{\partial x_q}+\tilde{u}_k^1(\mathbf{x})\right]\Big|_{face5}=\left[-\chi_k^{pq}(\mathbf{x},\mathbf{y})\frac{\partial u_p^0(\mathbf{x})}{\partial x_q}+\tilde{u}_k^1(\mathbf{x})\right]\Big|_{face6}$$

(Eq. 3-18)

Since $\tilde{u}_k^1(\mathbf{x})$ is independent of $\mathbf{y}$ and the macroscopic strains

$$\varepsilon_{pq}^0=\frac{1}{2}\left[\frac{\partial u_p^0(\mathbf{x})}{\partial x_q}+\frac{\partial u_q^0(\mathbf{x})}{\partial x_p}\right] \qquad \text{(Eq. 3-19)}$$

are arbitrary uniform strains, Eq. 3-17 can be rewritten in terms of the characteristic function as

$$-\chi_k^{pq}(\mathbf{x},\mathbf{y})\Big|_{face1}=-\chi_k^{pq}(\mathbf{x},\mathbf{y})\Big|_{face3},\ -\chi_k^{pq}(\mathbf{x},\mathbf{y})\Big|_{face2}=-\chi_k^{pq}(\mathbf{x},\mathbf{y})\Big|_{face4}$$

$$-\chi_k^{pq}(\mathbf{x},\mathbf{y})\Big|_{face5}=-\chi_k^{pq}(\mathbf{x},\mathbf{y})\Big|_{face6}$$

(Eq. 3-20)

Hence, the characteristic function can be completely determined from Eq. 3-15 and Eq. 3-20.

On the other hand, inserting Eq. 3-12 into Eq. 3-10 leads to

$$\int_\Omega D_{ijkl}^H(\mathbf{x})\frac{\partial u_k^0(\mathbf{x})}{\partial x_l}\frac{\partial v_i(\mathbf{x})}{\partial x_j}d\Omega=\int_\Omega b_i(\mathbf{x})v_i(\mathbf{x})d\Omega+\int_{\Gamma_T}\overline{T}_i(\mathbf{x})v_i(\mathbf{x})d\Gamma,\ \ \mathbf{x}\in\Omega \qquad \text{(Eq. 3-21)}$$

$$D_{ijkl}^H(\mathbf{x})=\frac{1}{|Y|}\int_Y\left(E_{ijkl}-E_{ijpq}\frac{\partial\chi_p^{kl}}{\partial y_q}\right)dY \qquad \text{(Eq. 3-22)}$$

$$b_i(\mathbf{x})=\frac{1}{|Y|}\int_Y f_i(\mathbf{x},\mathbf{y})dY \qquad \text{(Eq. 3-23)}$$

Equation Eq. 3-21 describes the macroscopic equilibrium. Where D_{ijkl}^H denotes the homogenized elastic constants and is usually called as the macroscopic elastic constants. Therefore the basic equations of a homogenization problem in the sense of first order

approximation are reduced to the integral equation Eq. 3-15 subject to periodic conditions of Eq. 3-20 and the integral equation Eq. 3-21 subject to specified boundary conditions. Both of the integral equations can be solved separately by the use of FEM. We can firstly obtain $\chi_i^{kl}(\mathbf{x},\mathbf{y})$ by solving Eq. 3-15 under the periodic conditions Eq. 3-20 and then solve Eq. 3-21 to obtain macroscopic $u_k^0(\mathbf{x})$. If only the homogenized elastic constants D_{ijkl}^H is of interest, we can solve Eq. 3-15 and calculate Eq. 3-22 to obtain $\chi_i^{kl}(\mathbf{x},\mathbf{y})$ and D_{ijkl}^H. Hence, solving Eq. 3-15 is an important step in the homogenization analysis.

It is observed that equation Eq. 3-15 is quite similar to the virtual work equation frequently used in the elasticity with initial strains and without body force and applied tractions along the boundary of the unit cell, if $\chi_i^{kl}(\mathbf{x},\mathbf{y})$ (i=1,2,3) are considered as three generalized displacements and $v_i(\mathbf{y})$ (i=1,2,3) as the corresponding virtual displacements for each $(kl = 11,22,33,23,31,12)$. In general, six independent sets of $(\chi_1^{kl},\chi_2^{kl},\chi_3^{kl})$ $(kl = 11,22,33,23,31,12)$ for a three-dimensional problem or three independent sets of $(\chi_1^{kl},\chi_2^{kl},\chi_3^{kl})$ $(kl = 11,22,12)$ for a two-dimensional problem need to be solved due to the symmetry of $\chi_i^{kl} = \chi_i^{lk}$. In the conventional solution, two processes of imposing initial strains and periodic conditions are necessary to solve every set of $(\chi_1^{kl},\chi_2^{kl},\chi_3^{kl})$. It is realized that these solution processes are obviously inefficient to solve the full sets of $\chi_i^{kl}(\mathbf{x},\mathbf{y})$. In present study, a new solution method developed in [13] is used alternately, which reduces the process of imposing the initial stresses and makes it easy to define unified periodic boundary conditions.

Referring to Eq. 3-15, it is realized that the solution of the inhomogeneous equations admits solutions which are additive in nature with one part being independent of ***x*** and linear in ***y*.** Therefore an alternative characteristic tensor $\tilde{\chi}_k^{pq}$ is introduced as follows.

$$\tilde{\chi}_k^{pq}(\mathbf{x},\mathbf{y}) = \chi_{0k}^{pq}(\mathbf{y}) - \chi_k^{pq}(\mathbf{x},\mathbf{y}) \qquad \text{(Eq. 3-24)}$$

Where χ_{0k}^{pq} is also a symmetric tensor of the second order for each k (k=1, 2, 3) and is expressed by

$$\left[\chi_{0k}^{pq}\right] = \begin{bmatrix} \chi_{0k}^{11} & \chi_{ok}^{12} & \chi_{0k}^{13} \\ \chi_{0k}^{21} & \chi_{0k}^{22} & \chi_{0k}^{23} \\ \chi_{0k}^{31} & \chi_{0k}^{32} & \chi_{0k}^{33} \end{bmatrix}, \qquad \chi_{0k}^{pq} = \frac{1}{2}(\delta_{pk} y_q + \delta_{qk} y_p) \qquad \text{(Eq. 3-25)}$$

or in detail by

$$\left[\chi_{01}^{pq}\right] = \begin{bmatrix} y_1 & \frac{1}{2}y_2 & \frac{1}{2}y_3 \\ \frac{1}{2}y_2 & 0 & 0 \\ \frac{1}{2}y_3 & 0 & 0 \end{bmatrix}, \qquad \left[\chi_{02}^{pq}\right] = \begin{bmatrix} 0 & \frac{1}{2}y_1 & 0 \\ \frac{1}{2}y_1 & y_2 & \frac{1}{2}y_3 \\ 0 & \frac{1}{2}y_3 & 0 \end{bmatrix},$$

$$\left[\chi_{03}^{pq}\right] = \begin{bmatrix} 0 & 0 & \frac{1}{2}y_1 \\ 0 & 0 & \frac{1}{2}y_2 \\ \frac{1}{2}y_1 & \frac{1}{2}y_2 & y_3 \end{bmatrix}$$

(Eq. 3-26)

Where the symbol δ_{ij} is the Kronecker delta defined by

$$\delta_{ij} = \begin{cases} 1 & \text{if } i = j \\ 0 & \text{if } i \neq j \end{cases} \qquad \text{(Eq. 3-27)}$$

It is seen that the component of χ_{0k}^{pq} is a linear function of y_i or zero for given k (k=1,2,3), p and q (p,q=1,2,3), and its derivation can be expressed by

$$\frac{\partial \chi_{0k}^{pq}}{\partial y_l} = \frac{1}{2}(\delta_{pk}\delta_{ql} + \delta_{qk}\delta_{pl}) \qquad \text{(Eq. 3-28)}$$

Inserting Eq. 3-24 into Eq. 3-15 leads to

$$\int_Y \left(E_{ijkl} - E_{ijpq}\frac{\partial \chi_{0p}^{kl}(\mathbf{y})}{\partial y_q} + E_{ijpq}\frac{\partial \tilde{\chi}_p^{kl}(\mathbf{x},\mathbf{y})}{\partial y_q}\right)\frac{\partial v_i(\mathbf{y})}{\partial y_j}dY = 0 \qquad \text{(Eq. 3-29)}$$

From Eq. 3-28 and $E_{ijkl} = E_{ijlk}$, we have

$$E_{ijpq}\frac{\partial \chi_{0p}^{kl}}{\partial y_q} = \frac{1}{2}E_{ijpq}(\delta_{kp}\delta_{lq} + \delta_{lp}\delta_{kq}) = \frac{1}{2}(E_{ijkl} + E_{ijlk}) = E_{ijkl} \qquad \text{(Eq. 3-30)}$$

Then inserting Eq. 3-30 into Eq. 3-29 yields

$$\int_Y E_{ijkl}\frac{\partial \tilde{\chi}_k^{pq}(\mathbf{x},\mathbf{y})}{\partial y_l}\frac{\partial v_i(\mathbf{y})}{\partial y_j}dY = 0 \qquad \text{(Eq. 3-31)}$$

Similarly, by the use of Eq. 3-30 the homogenized elastic constants can be rewritten as

$$D_{ijkl}^H(\mathbf{x}) = \frac{1}{|Y|}\int_Y (E_{ijkl} - E_{ijpq}\frac{\partial \chi_{0p}^{kl}}{\partial y_q} + E_{ijpg}\frac{\partial \tilde{\chi}_p^{kl}}{\partial y_q})dY = \frac{1}{|Y|}\int_Y E_{ijpq}\frac{\partial \tilde{\chi}_p^{kl}}{\partial y_q}dY \qquad \text{(Eq. 3-32)}$$

Consequently, it is seen that Eq. 3-15 has been transformed into a homogeneous integral equation Eq. 3-31 in terms of the new characteristic function $\tilde{\chi}_i^{kl}(\mathbf{x},\mathbf{y})$. That is, the original problem with initial strains and periodic conditions has been reduced to a simple displacement boundary value problem. Hence, the calculation process of imposing the initial stresses is reduced during the solution of every set $(\chi_1^{kl}, \chi_2^{kl}, \chi_3^{kl})$. Furthermore, the periodic conditions for a rectangular parallelepiped unit cell in terms of $\tilde{\chi}_k^{pq}$ can be easily expressed as follows by the substitution of Eq. 3-24 into Eq. 3-20.

$$[\tilde{\chi}_k^{pq}(\mathbf{x},\mathbf{y}) - \chi_{0k}^{pq}(\mathbf{y})]\Big|_{face1} = [\tilde{\chi}_k^{pq}(\mathbf{x},\mathbf{y}) - \chi_{0k}^{pq}(\mathbf{y})]\Big|_{face3}$$

$$[\tilde{\chi}_k^{pq}(\mathbf{x},\mathbf{y}) - \chi_{0k}^{pq}(\mathbf{y})]\Big|_{face2} = [\tilde{\chi}_k^{pq}(\mathbf{x},\mathbf{y}) - \chi_{0k}^{pq}(\mathbf{y})]\Big|_{face4}$$

$$[\tilde{\chi}_k^{pq}(\mathbf{x},\mathbf{y}) - \chi_{0k}^{pq}(\mathbf{y})]\Big|_{face5} = [\tilde{\chi}_k^{pq}(\mathbf{x},\mathbf{y}) - \chi_{0k}^{pq}(\mathbf{y})]\Big|_{face6}$$

(Eq. 3-33)

Referring to Eq. 3-16 and Eq. 3-26, the periodic conditions of Eq. 3-33 for six sets $\tilde{\chi}_k^{pq}$ $(pq = 11, 22, 33, 23, 31, 12)$ can be rewritten in detail as

$$\tilde{\chi}_1^{11}\Big|_{face1} - \tilde{\chi}_1^{11}\Big|_{face3} = -a, \quad \tilde{\chi}_k^{11}\Big|_{face1} = \tilde{\chi}_k^{11}\Big|_{face3} \quad (k = 2,3),$$

$$\tilde{\chi}_k^{11}\Big|_{face2} = \tilde{\chi}_k^{11}\Big|_{face4}, \quad \tilde{\chi}_k^{11}\Big|_{face5} = \tilde{\chi}_k^{11}\Big|_{face6} \quad (k = 1,2,3)$$

(Eq. 3-34a)

$$\tilde{\chi}_2^{22}\Big|_{face2} - \tilde{\chi}_2^{22}\Big|_{face4} = -b, \quad \tilde{\chi}_k^{22}\Big|_{face2} = \tilde{\chi}_k^{22}\Big|_{face4} \quad (k = 1,3)$$

$$\tilde{\chi}_k^{22}\Big|_{face1} = \tilde{\chi}_k^{22}\Big|_{face3}, \quad \tilde{\chi}_k^{22}\Big|_{face5} = \tilde{\chi}_k^{22}\Big|_{face6} \quad (k = 1,2,3)$$

(Eq. 3-34b)

$$\tilde{\chi}_3^{33}\Big|_{face5} - \tilde{\chi}_3^{33}\Big|_{face6} = -c, \quad \tilde{\chi}_k^{33}\Big|_{face5} = \tilde{\chi}_k^{33}\Big|_{face6} \quad (k = 1,2)$$

$$\tilde{\chi}_k^{33}\Big|_{face1} = \tilde{\chi}_k^{33}\Big|_{face3}, \quad \tilde{\chi}_k^{33}\Big|_{face2} = \tilde{\chi}_k^{33}\Big|_{face4} \quad (k = 1,2,3)$$

(Eq. 3-34c)

$$\tilde{\chi}_k^{23}\Big|_{face1} = \tilde{\chi}_k^{23}\Big|_{face3} \quad (k = 1,2,3),$$

$$\tilde{\chi}_3^{23}\Big|_{face2} - \tilde{\chi}_3^{23}\Big|_{face4} = -\frac{1}{2}b, \quad \tilde{\chi}_k^{23}\Big|_{face2} = \tilde{\chi}_k^{23}\Big|_{face4} \quad (k = 1,2)$$

$$\tilde{\chi}_2^{23}\Big|_{face5} - \tilde{\chi}_2^{23}\Big|_{face6} = -\frac{1}{2}c, \quad \tilde{\chi}_k^{23}\Big|_{face5} = \tilde{\chi}_k^{23}\Big|_{face6} \quad (k = 1,3)$$

(Eq. 3-34d)

$$\tilde{\chi}_3^{31}\Big|_{face1} - \tilde{\chi}_3^{31}\Big|_{face3} = -\frac{1}{2}a, \quad \tilde{\chi}_k^{31}\Big|_{face1} = \tilde{\chi}_k^{31}\Big|_{face3} \quad (k = 1,2)$$

$$\tilde{\chi}_k^{31}\Big|_{face2} = \tilde{\chi}_k^{31}\Big|_{face4} \quad (k = 1,2,3)$$

$$\tilde{\chi}_1^{31}\Big|_{face5} - \tilde{\chi}_1^{31}\Big|_{face6} = -\frac{1}{2}c, \quad \tilde{\chi}_k^{31}\Big|_{face5} = \tilde{\chi}_k^{31}\Big|_{face6} \quad (k = 2,3)$$

(Eq. 3-34e)

$$\tilde{\chi}_2^{12}\Big|_{face1} - \tilde{\chi}_2^{12}\Big|_{face3} = -\frac{1}{2}a, \quad \tilde{\chi}_k^{12}\Big|_{face1} = \tilde{\chi}_k^{12}\Big|_{face3} \quad (k = 1,3)$$

$$\tilde{\chi}_1^{12}\Big|_{face2} - \tilde{\chi}_1^{12}\Big|_{face4} = -\frac{1}{2}b, \quad \tilde{\chi}_k^{12}\Big|_{face2} = \tilde{\chi}_k^{12}\Big|_{face4} \quad (k = 2,3)$$

$$\tilde{\chi}_k^{12}\Big|_{face5} = \tilde{\chi}_k^{12}\Big|_{face6} \quad (k = 1,2,3)$$

(Eq. 3-34f)

From Eq. 3-34, it is seen that these six sets of displacement boundary conditions represent six simple and basic deformations of three extensions and three shears under the periodic constraint, respectively, and that the only external loads are the given displacements along the boundary of unit cell. These displacement boundary value problems expressed by Eq. 3-31 and Eq. 3-34 are easily solved by the use of any FEM code. Similar to the above derivation procedure, exact periodic boundary conditions can also be derived explicitly for a unit cell in any two-dimensional or other three-dimensional shape. Moreover, if the elasticity problem of the unit cell has some symmetric features, equations of Eq. 3-34 may be much simplified because several ones of these equations could be satisfied automatically due to the symmetry. Once $(\tilde{\chi}_1^{kl}, \tilde{\chi}_2^{kl}, \tilde{\chi}_3^{kl})$ are solved by the use of FEM, we can easily calculate the homogenized elastic constants from Eq. 3-32 and then solve $u_i^0(\mathbf{x})$ from Eq. 3-21 with the help of FEM.

3.3.2 Homogenization analysis of UACS laminas

In order to implement the multiscale analysis in Fig. 3-2, the first task is to obtain the effective anisotropic stiffness constants of the UACS laminas with three slit distribution patterns because it is difficult to determine all of these constants experimentally. A homogenization analysis [13, 14] using a unit cell is available for the calculation of the effective anisotropic stiffness constants of the UACS laminas. Three rectangular parallelepiped unit cells for the UACS laminas with three different slit distribution patterns are depicted in Fig. 3-5. The dimensions of the unit cells are 25 mm in length, 10 mm in width, and 0.2 mm in thickness.

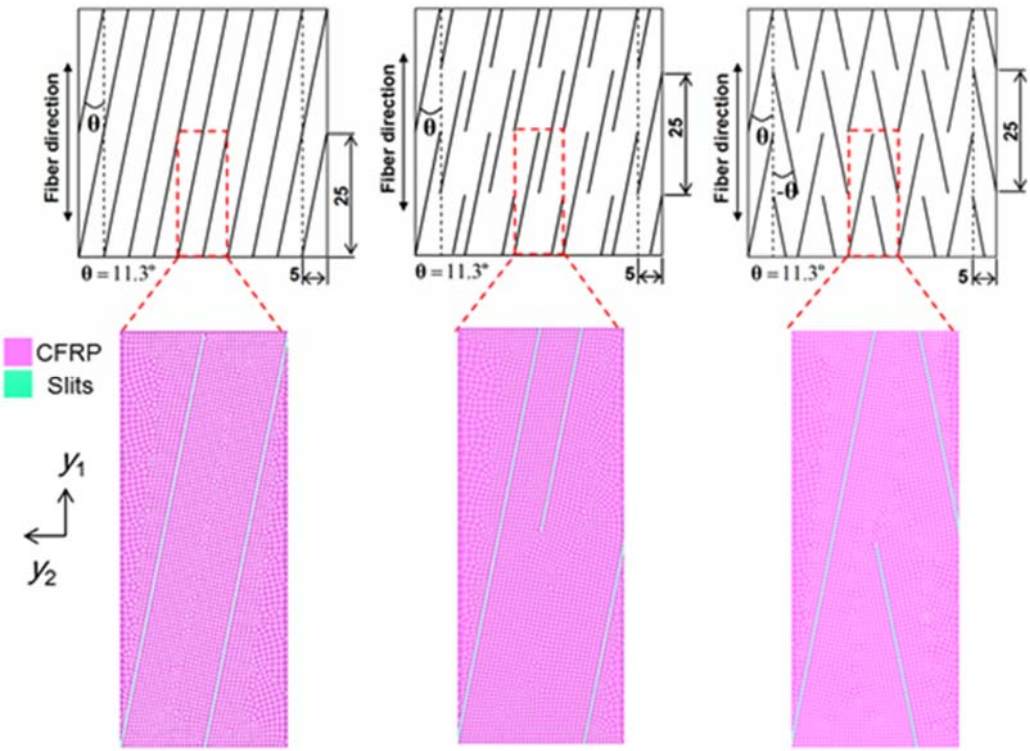

(a) Continuous slit distribution (b) Staggered slit distribution (c) Bi-angled slit distribution

Figure 3-5: FEM meshes of three representative volume cells for the three kinds of UACS laminas in progressive damage analysis.

The thin and long line-like regions represent slits filled with epoxy resin, the width of all the slits is 0.1 mm, and the surrounding areas are CFRP. Based on the homogenization theory, applying the displacement conditions of Eq. 3-34 to the unit cell and solving Eq. 3-31 by means of FEM lead to the numerical solution of $\tilde{\chi}_p^{kl}$ (p=1, 2, 3; kl = 11, 22, 33, 23, 31, 12). Then we can obtain the homogenized elastic constants from the calculation of Eq. 3-32. FEM software of MSC.MARC 2010 is used in the present analysis and eight-node solid element is employed in all of the unit cell models. After the effective stiffness constants for the UACS laminas with three slit distribution patterns are obtained from the homogenization analysis, the stiffness constants of the [45/0/-45/90] and [90/-45/0/45] laminates used in the multiscale model of Fig. 3-1 are easily calculated using the classical lamination theory.

3.4 Analysis of damage progression in the UACS laminates

In this subsection, the damage progression analysis in the UACS laminates using the multiscale FEM model shown in Fig. 3-1 is described. As the same with previous subsection, FEM software of MSC.MARC 2010 is used in the damage progression analysis. The size and quantity of the elements of the FEM mesh are controlled by a specified length, a parameter called the length scale, between two seed nodes along the curves on the boundary of the model. To investigate the influence of the mesh size on the analytical results, analysis for a UACS laminate with bi-angled slit distribution is firstly conducted using five different FEM meshes with five different length scales of 0.5 mm, 0.75 mm, 1 mm, 1.25 mm, and 1.5 mm, as shown in Fig. 3-6 (the FEM mesh with length scale of 1 mm is presented in Fig. 3-1). From the calculation results which will be

presented in the subsection of 3.5 Results and discussions later, it is confirmed that the numerical results tend to converge to constants with the decreasing of the length scale from the length scale of 1 mm. Thus, all the calculations of the UACS laminates with other slit distribution patterns are conducted based on the meshes with this length scale. Furthermore, in order to investigate the validity of the present asymmetrical FEM model (Fig. 3-1), comparative analysis using the asymmetrical model and a symmetrical model for the UACS laminate with bi-angled slit distribution is also conducted. The symmetrical model is easily constructed from the asymmetrical model shown in Fig. 3-1 by deleting the lower two layers and applying the symmetrical boundary conditions to the bottom surface. Eight-node solid elements are used for all the elements including the cohesive interface elements with zero thickness. The bilinear constitutive model is employed to simulate the damage behavior of interface and maximum stress criterion is employed to simulate the damage behavior in CFRP and slits, respectively.

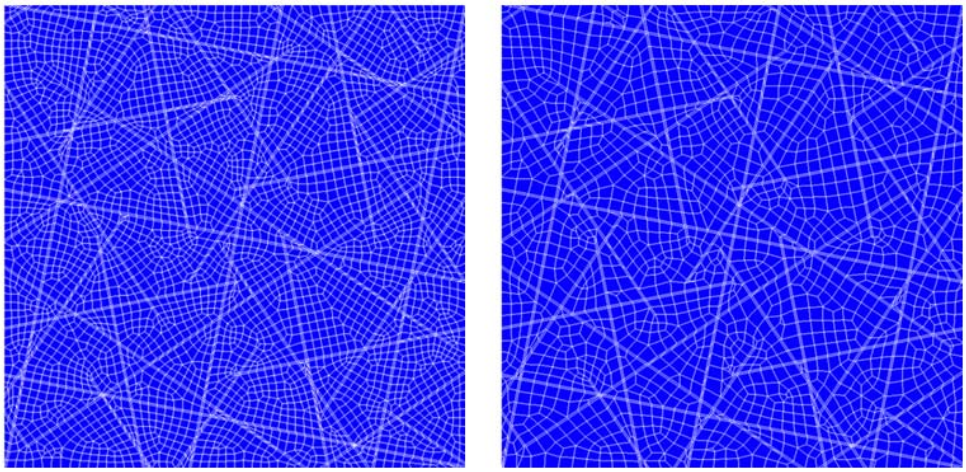

Length scale = 0.5 mm　　Length scale = 0.75 mm

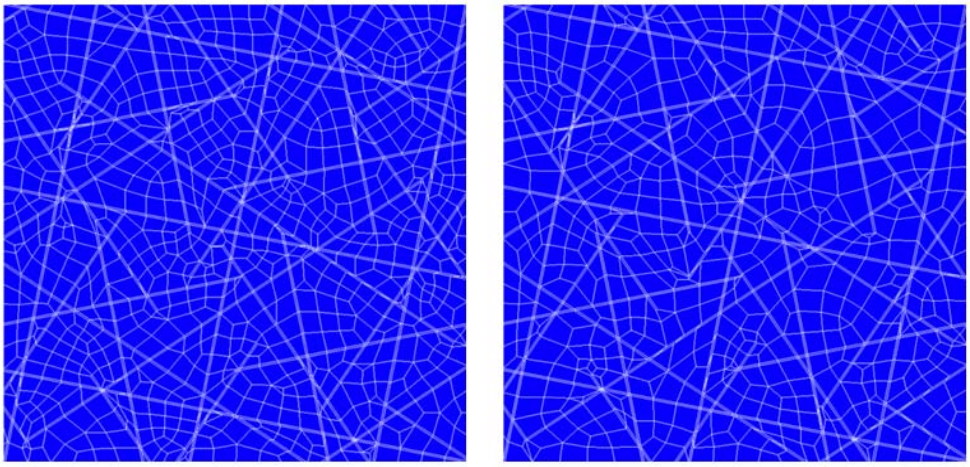

Length scale = 1.25 mm Length scale = 1.5 mm

Figure 3-6: FEM meshes of UACS laminate with bi-angled slit distribution in different length scales.

3.4.1 Bilinear constitutive model for the cohesive interface elements

As being discussed in the last chapter, delamination between UACS layers is the main failure mode of different patterns UACS laminates. The simulation of delamination using the finite element method (FEM) is normally performed by means of the Virtual Crack Closure Technique (VCCT) [15], or using cohesive finite elements [16-19]. The VCCT is based on the assumption that the energy released during delamination propagation equals the work required to close the crack back to its original position. There are some difficulties when using the VCCT in the simulation of progressive delamination. The calculation of fracture parameters requires nodal variables and topological information from the nodes ahead and behind the crack front. Such calculations are tedious to perform and may require remeshing for crack propagation.

The use of cohesive elements can overcome some of these above difficulties. Cohesive elements can predict both the onset and propagation of delamination. It is shown that it is

possible to predict the propagation of delamination accurately in specimens with and without pre-existing cracks by using coarse meshes and their correspondingly adjusted constitutive models [16].

In this study, a layer of cohesive elements is inserted into the two interfaces of UACS laminates between 0° ply and the adjacent 45° and -45° plies to simulate the onset and propagation of delamination, as shown in Fig. 3-1, which is the one of the main failure modes for UAC laminates under tension.

Cohesive element type 188 is chosen to model interface [20]. Element type 188 is a mechanical eight-node three-dimensional interface element, which can be used to simulate the onset and progress of delamination. The element is typically used to model the interface between different materials, where nodes 1, 2, 3 and 4 correspond to one side (called the bottom) of the interface and nodes 5, 6, 7 and 8 to the other (called the top) as shown in Fig. 3-7. The stress components of the element are one normal traction and two shear tractions, which are expressed with respect to the local coordinate system. The corresponding deformations are the relative displacements between the top and the bottom face of the element. The element is allowed to be infinitely thin, in which case the faces 1-2-3-4 and 5-6-7-8 coincide. The constitutive behavior of these elements is expressed in terms of tractions versus relative displacements between the top and bottom surface of the elements.

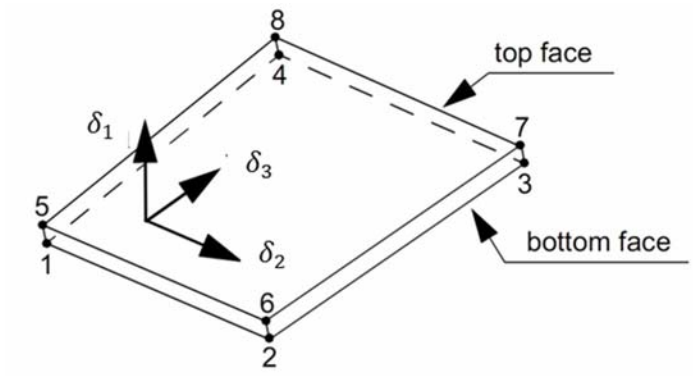

Figure 3-7: Illustration of eight-node cohesive elements.

Considering a 3-D interface element, the relative displacement components are given by one normal (subscript *n*) and two shear components (subscripts *s* and *t*), expressed with respect to the local element system:

$$\delta_n = \delta_n^{top} - \delta_n^{bottom}$$

$$\delta_s = \delta_s^{top} - \delta_s^{bottom} \qquad \text{(Eq. 3-35)}$$

$$\delta_t = \delta_t^{top} - \delta_t^{bottom}$$

Based on the relative displacement components, the effective opening displacement is defined as:

$$\delta = \sqrt{\delta_n^2 + \delta_s^2 + \delta_t^2} \qquad \text{(Eq. 3-36)}$$

The effective traction *t* is introduced as a function of the effective opening displacement and is characterized by an initial reversible response followed by an irreversible response as soon as a critical effective opening displacement δ_c has been reached. The irreversible part is characterized by increasing damage ranging from 0 (onset of delamination) to 1 (full delamination).

Three standard functions are currently available; namely, a bilinear, an exponential, and a linear-exponential function, as shown in Fig. 3-8. In this study, only bilinear function is used, as shown in Fig. 3-9, which is the most frequently and successfully used cohesive model [16].

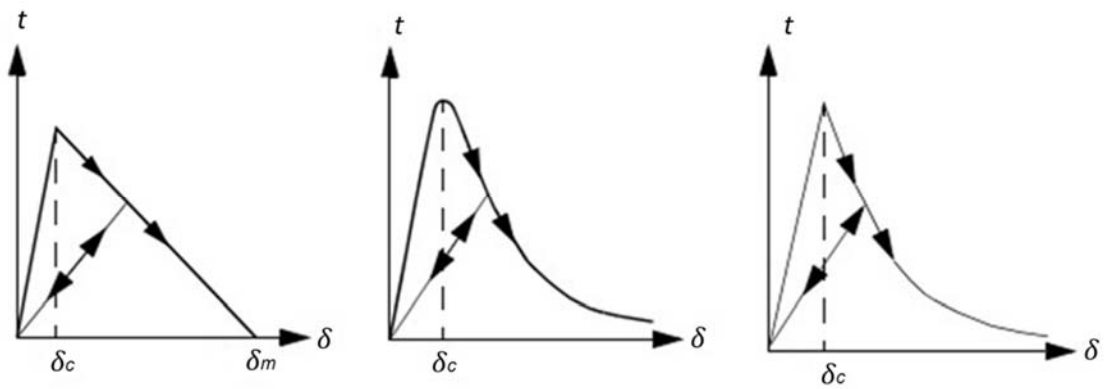

Figure 3-8: Three standard traction/displacement mode: Bilinear (left), Exponential (middle), and linear exponential (right)

The bilinear traction/displacement function is shown as follows:

$$t = \frac{2G_c\delta}{\delta_m\delta_c} \qquad if\ 0 \le \delta \le \delta_c$$

$$t = \frac{2G_c}{\delta_m}\left(\frac{\delta_m - \delta}{\delta_m - \delta_c}\right) \qquad if\ \delta_c \le \delta \le \delta_m \qquad \text{(Eq. 3-37)}$$

$$t = 0 \qquad if\ \delta > \delta_m$$

in which G_c is the critical energy release rate (cohesive energy), δ_m is the maximum effective opening displacement. It can easily be verified that the maximum effective traction t_c, corresponding to the critical effective opening displacement δ_c is given by:

$$t_c = \frac{2G_c}{\delta_m} \qquad \text{(Eq. 3-38)}$$

So if the maximum effective traction is known, the critical or maximum effective opening displacement can be determined by:

$$\delta_m = \frac{2G_c}{t_c} \qquad \text{(Eq. 3-39)}$$

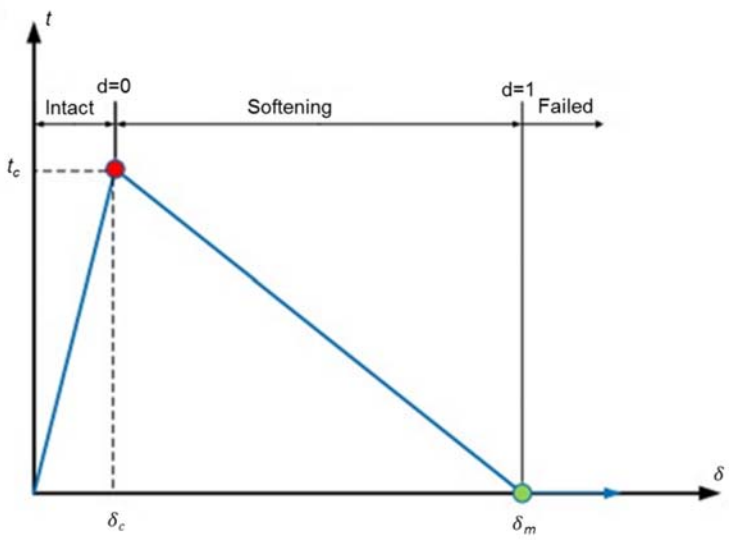

Figure 3-9: Characteristics of constitutive relations (Bilinear).

Interface elements behave in three unique regions: intact region, softening region and failed region [17-19]. The intact region is dedicated for the ideal bulk material representation, that is, the undamaged part. The intact region goes up to the point where delamination onset occurs. This is the point where chemical bonds of the intact materials start to break, in other words, the cohesive phenomenon starts. Therefore, the maximum traction t_c is the interfacial strength defining the onset of delamination.

In the intact region, the traction versus displacement profile is given as follows:

$$t = K\delta \quad \text{if } 0 \leq \delta \leq \delta_c \qquad \text{(Eq. 3-40)}$$

K is the interfacial stiffness, the slope of traction versus displacement of the cohesive element in intact region shown as below:

$$K = \frac{t_c}{\delta_c} \qquad \text{(Eq. 3-41)}$$

After delamination onset, the softening of the interface occurs due to the cohesive effects like fiber bridging, crazing and micro void, which means the phenomenon of cohesive effects. Softening region is the one between delamination onset displacement and the maximum displacement relating to the total failure.

According to damage mechanics, a damage parameter *d* is introduced as follows to describe the delamination behavior [18]:

$$t = (1 - d)K\delta \quad if\ \delta_c \leq \delta \leq \delta_m \qquad \text{(Eq. 3-42)}$$

It is easy to understand from above equation that the line equation shows a declining behavior as the damage term *d* increases from no damage value of "0" to fully damaged value of "1". Referring to Eq. 3-37, Eq. 3-38, and Eq. 3-41, one can obtain

$$\begin{aligned} d &= 0 && if\ 0 \leq \delta \leq \delta_c && (Intact) \\ d &= \frac{\delta_m(\delta - \delta_c)}{\delta(\delta_m - \delta_c)} && if\ \delta_c \leq \delta \leq \delta_m && (Softening) \\ d &= 1 && if\ \delta > \delta_m && (Failed) \end{aligned} \qquad \text{(Eq. 3-43)}$$

When the displacement δ exceeded the maximum displacement δ_m (d=1), full delamination happens. In other words, the interface element is fully failed. The damage parameter *d* is calculated by using Eq. 3-43.

If the cohesive element is fully damaged, all the integration points have reached the maximum damage, this element would be deactivated. In a contact analysis, this implies that the outer boundary of a contact body is newly determined. After this point, the cohesive elements would behave as a traction free crack.

Table 3-2 lists material properties of the interface elements used in this study, according to Ref. [16]. Based on these material properties listed in this table, the interfacial strength t_c and stiffness K can be easily calculated, and they are 60 N/mm^2 and 10^6 N/mm^3, respectively.

Table 3-2: Material properties of the cohesive element.

Critical energy release rate G_c (N/mm)	0.352
Critical opening displacement δ_c (mm)	6×10^{-6}
Maximum opening displacement δ_m (mm)	0.0117

3.4.2 Maximum stress criterion

The maximum stress criterion is used to simulate the damage behavior of the CFRP regions and the slits in the top four plies. At each integration point, six failure indices *FIi* (i=1, 2, …, 6) are calculated as follows:

$$FI1 = \begin{cases} \left(\frac{\sigma_1}{X_t}\right) & if\ \sigma_1 > 0 \\ \left(-\frac{\sigma_1}{X_c}\right) & if\ \sigma_1 < 0 \end{cases} \quad \text{(Eq. 3-44a)}$$

$$FI2 = \begin{cases} \left(\frac{\sigma_2}{Y_t}\right) & if\ \sigma_2 > 0 \\ \left(-\frac{\sigma_2}{Y_c}\right) & if\ \sigma_2 < 0 \end{cases} \quad \text{(Eq. 3-44b)}$$

$$FI3 = \begin{cases} \left(\frac{\sigma_3}{Z_t}\right) & if\ \sigma_3 > 0 \\ \left(-\frac{\sigma_3}{Z_c}\right) & if\ \sigma_3 < 0 \end{cases} \quad \text{(Eq. 3-44c)}$$

$$FI4 = \left(\left|\frac{\sigma_{12}}{S_{12}}\right|\right) \quad \text{(Eq. 3-44d)}$$

$$FI5 = \left(\left|\frac{\sigma_{23}}{S_{23}}\right|\right) \quad \text{(Eq. 3-44e)}$$

$$FI6 = \left(\left|\frac{\sigma_{31}}{S_{31}}\right|\right) \quad \text{(Eq. 3-44f)}$$

In these equations, $X_{t(c)}$, $Y_{t(c)}$, $Z_{t(c)}$ represent the tensile (compressive) strength along three principal material directions of the CFRP lamina, respectively. The fiber direction is along the 1-direction, the 12-plane is called the in-plane. S_{12}, S_{23}, S_{31} represents three shear strength in three principal material planes of 12-plane, 23-plane, and 31-plane, respectively, and $S_{12} = S_{31}$. The values of these six strength parameters used in the analysis are listed in Table 3-1. In order to reduce the computational cost, the tensile strength of the epoxy resin is used for the tensile failure index in the slit irrespective of the failure occurring at the interface or within the slit for an approximation.

3.4.3 Damage progression analysis

In the damage progression analysis of UACS laminates, uniform incremental displacement load is applied to the edge of x = 25 mm step by step along the fiber direction of the 0° ply of the multiscale model and appropriate fixed boundary conditions are applied to the edge of x = 0 mm, referring to Fig. 3-1. Linear elastic behavior is assumed for all the elements before the failure occurs. At each incremental load step, damage diagnosis is performed. In the case of interface damage, the stiffness reduction is imposed following the bilinear rule as mentioned above for the subsequent calculation. In

the case of failure occurred in the CFRP region outside of the slits, the corresponding components, related to the failure index, of the stiffness tensor of the element of CFRP is reduced to the 1% of its initial stiffness. However, in the case of the slit elements, the material epoxy is always considered as an isotropic material before and after failure occurring for the sake of approximation, thus the Young's modulus of the element is reduced to the 1% of its original value after failure occurring. The residual stiffness factor 1% is the default value in the FEM code of MSC. MARC2010. The flowchart of the progressive damage analysis is depicted in Fig. 3-10. Incremental loading procedure and iterative schemes are adopted in the damage progression analysis.

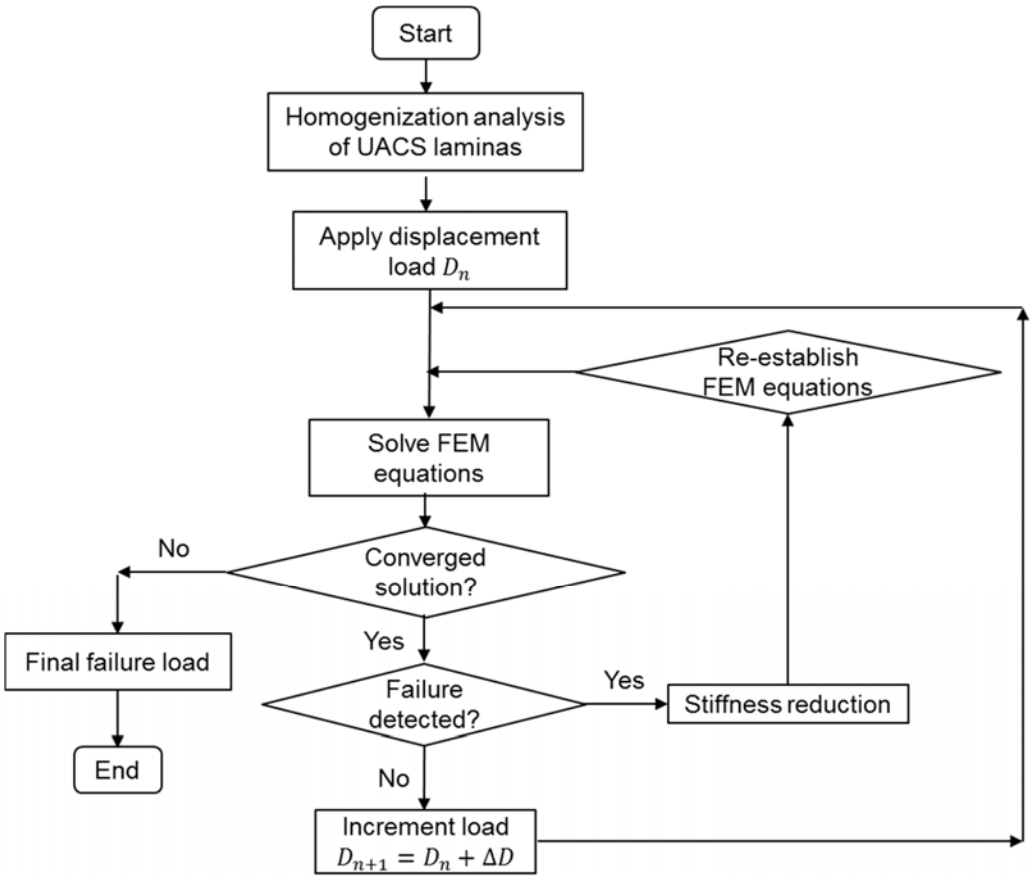

Figure 3-10: Flowchart of the multiscale FEM analysis.

3.5 Results and discussion

Numerical results obtained from the homogenization analysis and the damage progression analysis of the UACS quasi-isotropic laminates are presented in Fig. 3-11 to Fig. 3-23, Table 3-3, and Table 3-4.

In Fig. 3-11, the effective longitudinal modulus of the UACS quasi-isotropic laminates obtained from the homogenization analysis and the classical lamination theory are shown together with the experimental results to confirm the validity and accuracy of the homogenization analysis. The bar graphs denote the average values of the experimental results obtained from four specimens for each kind of UACS laminates, the error bars denote the scatter ranges of the experimental results, and the solid diamond points denote the FEM results. It is obvious that the numerical results agree well with the experimental values. These results reveal that the introduction of slits into the prepreg causes slight decrease of the modulus of the UACS laminates.

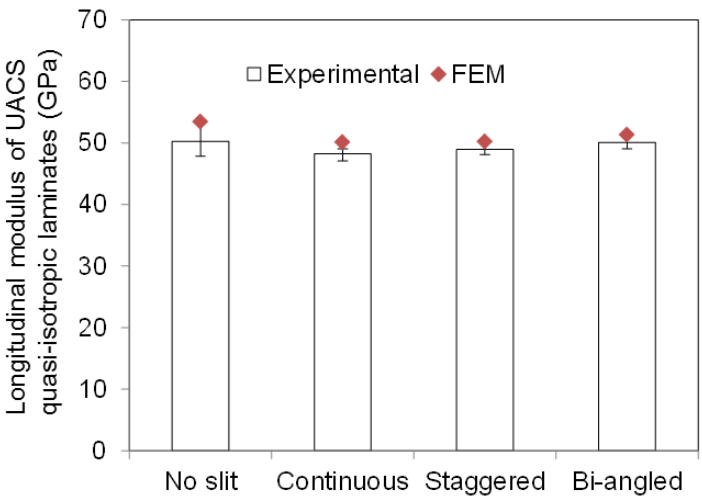

Figure 3-11: Longitudinal modulus of various quasi-isotropic laminates without or with slits obtained from homogenization analysis and the previous experimental results.

The influence of the mesh size on the numerical results for the UACS laminate with bi-angled slit distribution is described in Fig. 3-12, which is obtained from the damage progression analysis using the multiscale FEM model (Fig. 3-1). The dashed parts of the curves are drawn through extrapolation. It is clear that the strength value and critical load of delamination initiation tend to converge to two constants with the decreasing of the length scale from the length scale of 1 mm. These results indicate that the choice of the mesh with the length scale of 1 mm is appropriate to obtain the calculation results with appropriate accuracy and reasonable computational cost. Therefore, all the following numerical results are obtained from the analysis using the meshes with the length scale of 1 mm.

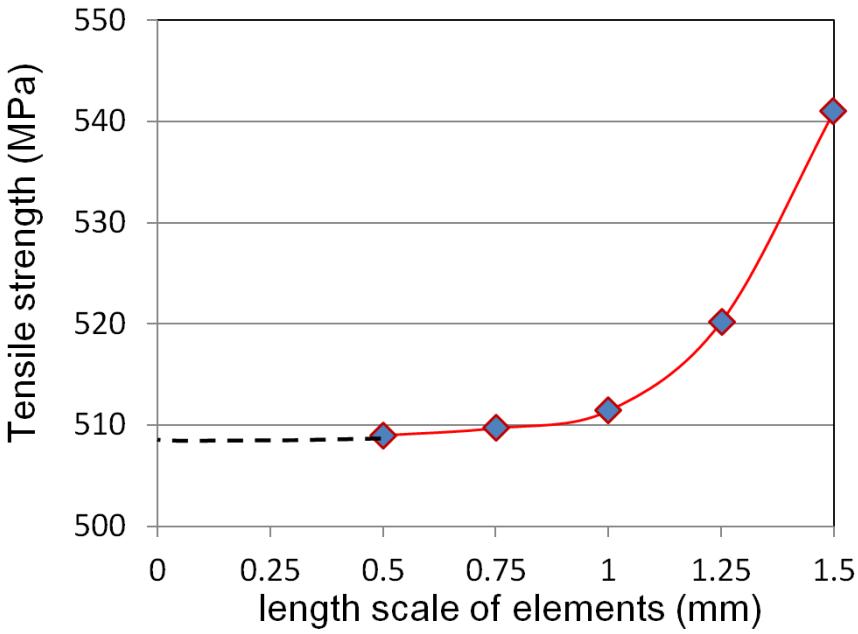

(a) Tensile strength

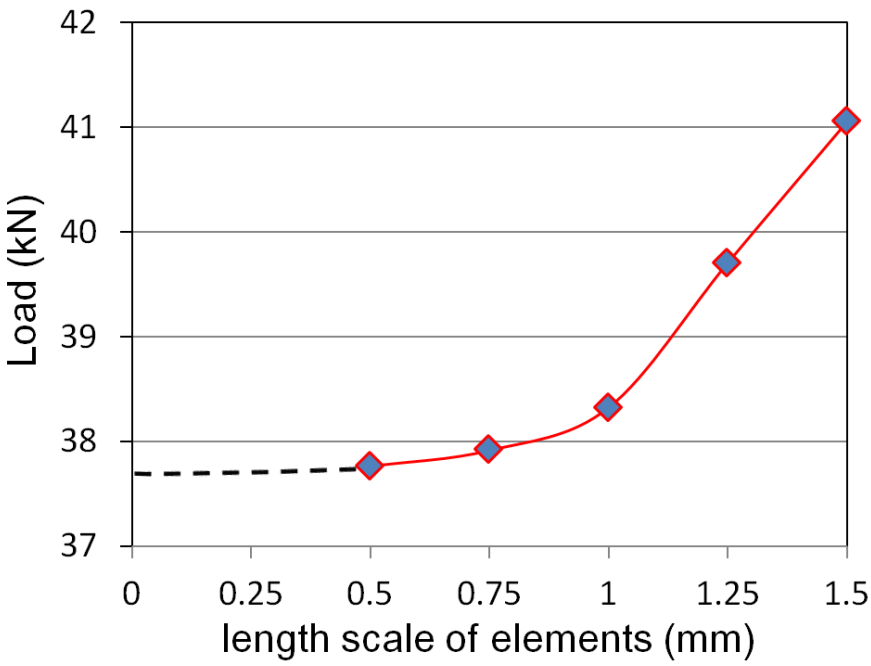

(b) Critical load of delamination initiation

Figure 3-12: Influence of mesh size on the calculation results.

In addition, from the comparative analysis using the asymmetrical model and the symmetrical model for the UACS laminate with bi-angled slit distribution, slightly different tensile strength values are obtained (Fig. 3-13). The asymmetrical model gives 511.40 MPa, and the symmetrical model gives 514.24 MPa, compared to the experimental result of 499.64 MPa. Therefore, the asymmetrical model is suitable for the damage progression analysis because it gives the tensile strength value closer to the experimental value than the symmetrical model.

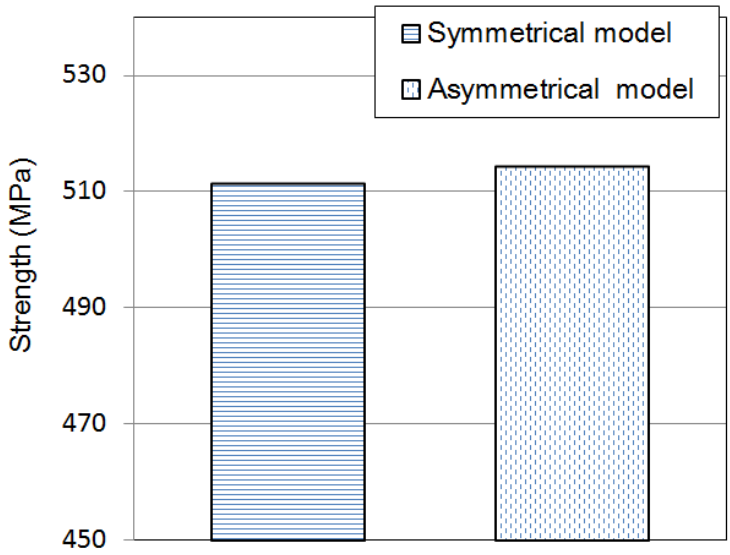

Figure 3-13: tensile strength results obtained from symmetrical and asymmetrical models of UACS laminate with bi-angled slit distribution.

The critical loads for main failure modes of the three kinds of UACS quasi-isotropic laminates are listed in Table 3-3. The tensile failure in the slits of 0° ply occurs firstly at relatively low loads less than 40% of their maximum loads of the UACS laminates, next the matrix cracking in the 90° ply occurs as the loads reach the 44% to 50% of their maximum loads, then the matrix cracking in 45° and -45° plies occurs at the loads near 25 kN (about 60% to 67% of their maximum loads), subsequently the delamination appears at the interfaces between 0° ply and its adjacent plies at the loads of about 34 kN, 36 kN, and 38 kN (about 94%, 90%, and 94% of their maximum loads), finally the fiber breakage in 0° ply occurs near the strength values for the UACS laminates with staggered and bi-angled slit distribution patterns. No fiber breakage occurs in the analysis of the UACS laminate with continuous slit distribution pattern and the laminate fails as the delamination extension.

Table 3-3: Critical loads for various failure modes occurring in the three kinds of UACS laminates.

Critical loads for various failure modes	Continuous	Staggered	Bi-angled
Tensile failure in slits of 0° plies (kN) ($FI1 = 1$)	13.6	14.6	13.9
Matrix cracking in 90° plies (kN) ($FI2 = 1$)	18.4	18.9	18.0
Matrix cracking in ±45° plies (kN) ($FI2 = 1$)	24.6	24.6	24.9
Delamination occurs (kN) ($d = 1$)	34.1	36.2	38.3
Fiber breakage in CFRP of 0° ply (kN) ($FI1 = 1$)		39.2	40.9
Final fracture (Maximum load) (kN)	36.4	40.4	40.9

In order to further display the behavior of damage progression in the UACS laminates, typical numerical results are illustrated in Fig. 3-14 to Fig. 3-21. The variation of the tensile failure index $FI1$ in the slits of the 0° plies of the UACS laminates with the applied load is depicted in Fig. 3-14. The value of vertical axis denotes the maximum value of the index $FI1$ in the slits for each kind of UACS laminates at each incremental load step. The index $FI1$ tends to increase linearly with the increasing load, the failure loads of the slits in the 0° plies of the three kinds of UACS laminates are slightly different (Table 3-3). These facts mean that the tensile failure in the slits of the 0° ply is almost independent of the slit distribution patterns. The typical images of the index $FI1$ in the 0° plies of the three kinds of UASC laminates at 16.2 kN are described in Fig. 3-15. Tensile failure occurs in many slits and extends along the slits.

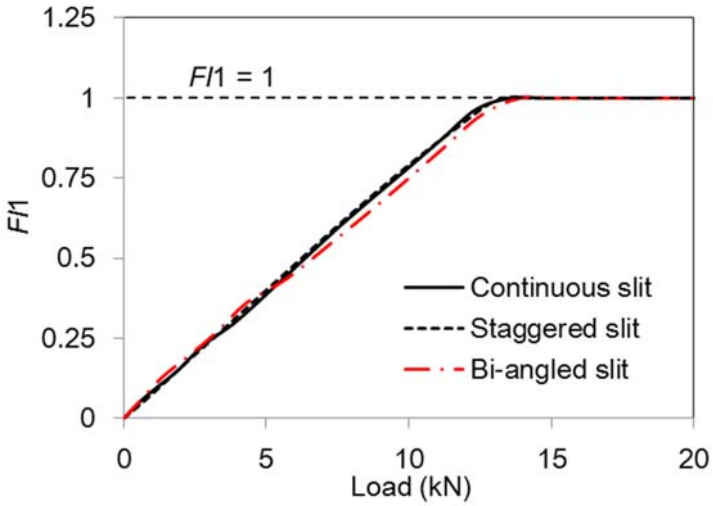

Figure 3-14: Load-tensile damage (*FI*1) curves of the slits in 0° plies of the three kinds of UACS laminates.

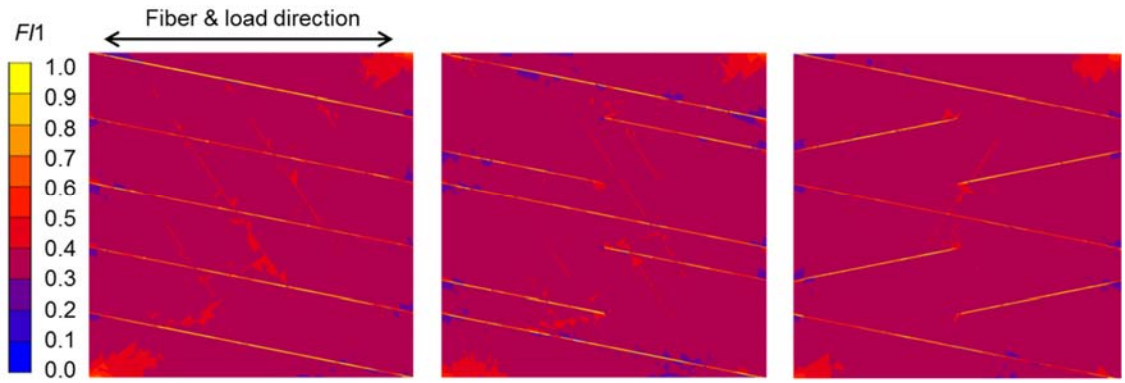

(a) Continuous slit pattern (b) Staggered slit pattern (c) Bi-angled slit pattern

Figure 3-15: Tensile damage images of the slits in 0° plies of the three kinds of UACS laminates at 16.2 kN.

The variation of the stress in a typical slit of the 0° ply of a UACS laminate with bi-angled slit distribution due to the reduction of the modulus of the epoxy resin elements is demonstrated in Fig. 3-16. From the right and upper graph, it is seen that the stress in the bright region (yellow) along the slit reaches its critical value given in Table 3-3. Thus, the modulus of the elements is reduced in the subsequent calculation, so that the stress in

these elements decreases immediately when the load increases from 33.0 kN to 34.3 kN, as shown in the right and lower graph.

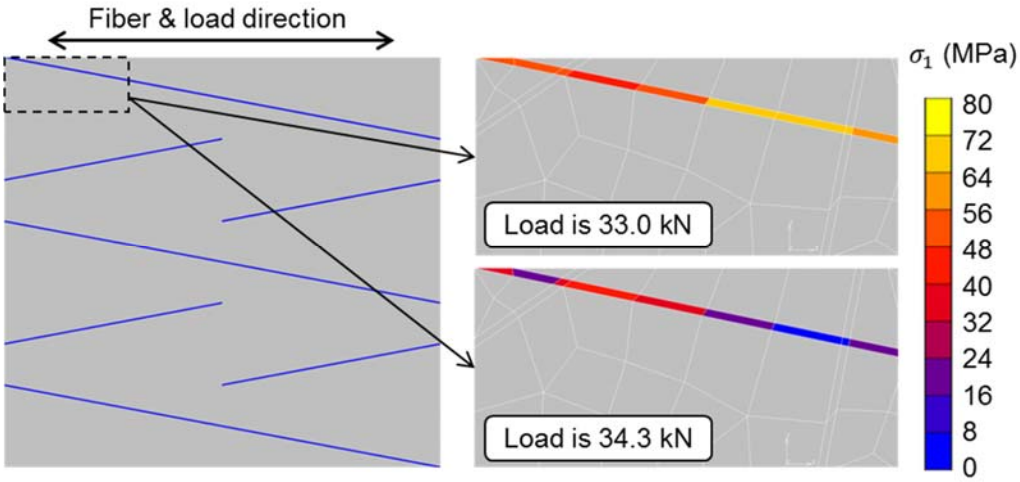

Figure 3-16: Variation of stress distribution in a typical slit in 0° ply of the UACS laminate with bi-angled slit distribution due to the reduction of stiffness after the tensile failure occurs in the slit.

Typical load-damage (*d*) curves of the interface 1 between the 45° and 0° plies of the three kinds of UACS laminates are presented in Fig. 3-17. The vertical axis denotes the maximum value of the interface damage for each kind of UACS laminates at each incremental load step. It is seen that the values of the interfacial damage parameter *d* of the three kinds of UACS laminates increase very slowly and have no significant difference at low load levels. On the other hand, after the load increases beyond about 25 kN, the values of the damage parameter *d* of all UACS laminates increase rapidly. Referring to Table 3-3, it is known that three failure modes of the slit cracking in the 0° ply, matrix cracking in the 90° ply, and matrix cracking in the ±45° plies have occurred when the load increases beyond 25 kN. Thus, it is deduced that the very high concentration of stresses around these cracks at the interfaces between the 0° ply and its adjacent ±45° plies promotes the rapid progression of the interface damage in the three

kinds of UACS laminates. Another interesting result is also seen in Fig. 3-17. That is, the increasing rates of the interface damage in the three kinds of UACS laminates are quite different. The UACS laminate with bi-angled slit distribution shows the lowest increasing rate, and the UACS laminate with continuous slit distribution shows the highest increasing rate. These results reveal that the bi-angled slit distribution is available in suppressing the delamination initiation and extension compared to other two slit distribution patterns. It is noted that the damage level of the interface 2 between the 0° and -45° plies is lower than that of the interface 1 because the interface 2 is relatively far away from the top surface of the laminate. Therefore, only the results associated to the interface 1 are described here.

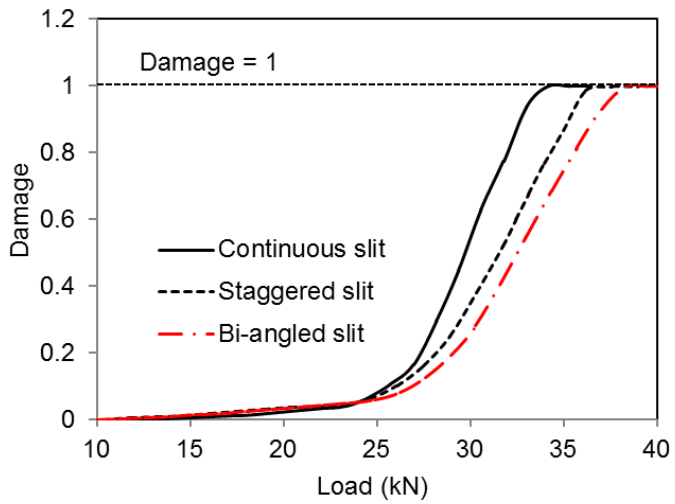

Figure 3-17: Typical load-damage (*d*) curves of the interface 1 between 45°and 0° plies of the three kinds of UACS laminates.

To understand the delamination initiation and extension at the interface, the interface damage images at the interface 1 are shown in Fig. 3-18 and Fig. 3-19. Typical damage image of the interface 1 in the UACS laminate with bi-angled slit distribution is shown in

Fig. 3-18. It is seen that the maximum value 0.618 of the damage occurs around the intersection point. This fact means that the delamination may initiate firstly around these intersection points of the slits in the 0° ply and the slits in the adjacent ±45° plies, although the delamination has not occurred yet because $d < 1$ at this load level. Typical images of delamination growth at the interface 1 of the three kinds of UACS laminates with the increase of the load are shown in Fig. 3-19. The upper three images describe the interface damage at the load 35.3 kN, the lower three images describe the interface damage at a few higher load 36.3 kN, and Fig. 3-19 (c) shows the same location as Fig. 3-18 but at increased loads. It is seen that the damage value and area in the lower three images are a few larger than those in the corresponding upper three images. These facts indicate that the delamination grows along the longitudinal and width directions of the slits in all of the three kinds of UACS laminates with the increasing load. However, different areas of high damage level are observed from the UACS laminates with different slit distribution patterns. The largest area of high damage level is observed in the UACS laminate with the continuous slit distribution, while the UACS laminate with bi-angled slit distribution shows the smallest damage area. These results reveal that the discontinuity and non-uniformity of the slit distribution is valid for the suppression of delamination progression compared to continuous and uniform slit distribution because the intact regions on the outside of the ends of discontinuous slits inhibit the extension of the delamination. Therefore, fibers in the intact regions of the 0° plies can carry higher load in the cases of UACS laminates with discontinuous slit distributions. These results agree well with the previous experimental results.

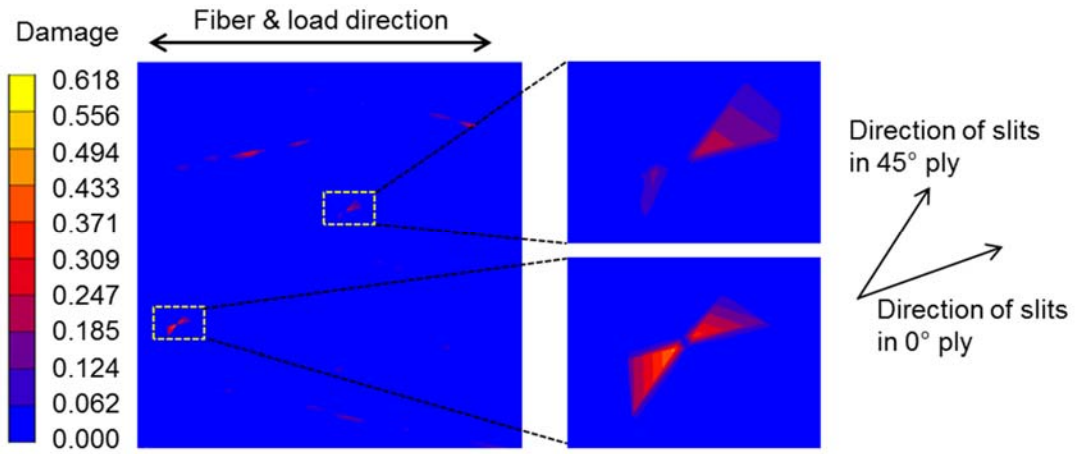

Figure 3-18: Typical damage (*d*) images in the interface 1 of the UACS laminate with bi-angled slit distribution at 34.3 kN.

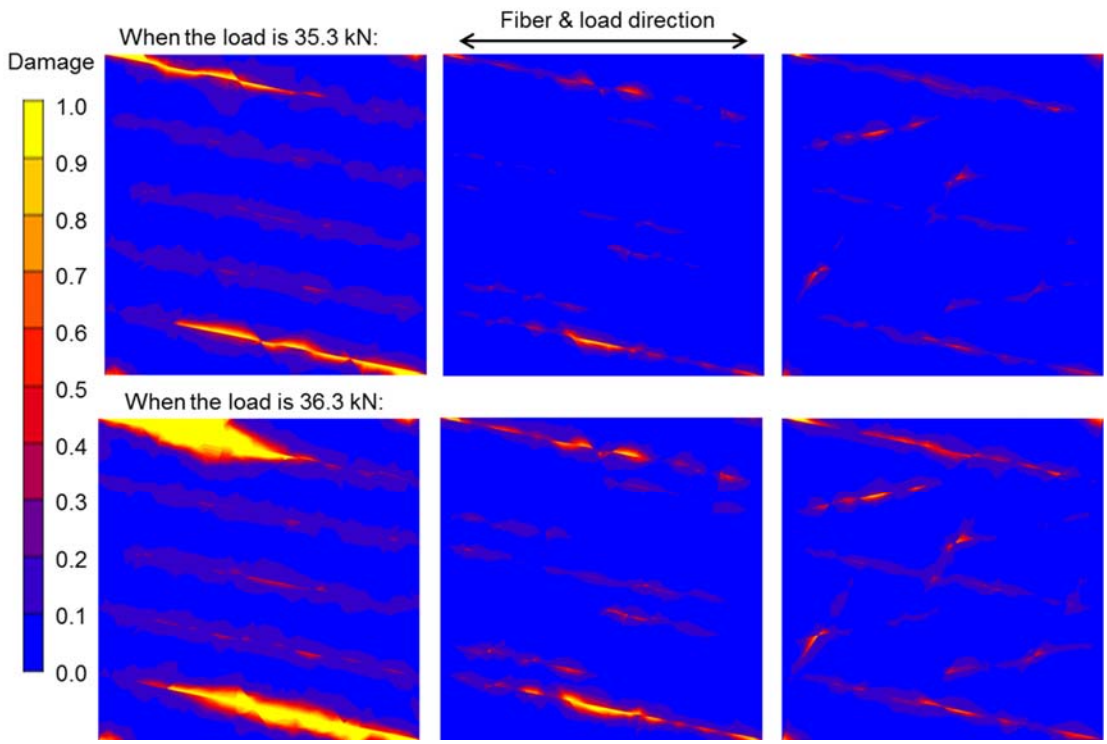

(a) Continuous slit pattern (b) Staggered slit pattern (c) Bi-angled slit pattern

Figure 3-19: Typical images of delamination growth in the interface 1 of the three kinds of UACS laminates with the increase of the load.

Typical images of the tensile failure index *FI*1 in the 0° ply for the three kinds of UACS laminates at or near their maximum loads are shown in Fig. 3-20 to investigate the fiber breakage occurrence. Very high *FI*1 is observed in the small regions around the slit ends of the 0° plies in the UACS laminates with the staggered and bi-angled slit distribution patterns. The very high *FI*1 implicates that the fiber breakage may occur in these regions due to the high tensile stress.

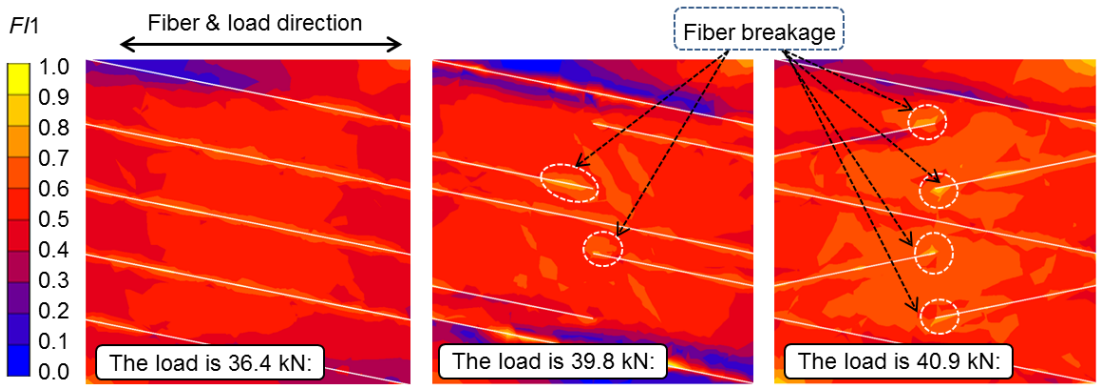

(a) Continuous slit pattern (b) Staggered slit pattern (c) Bi-angled slit pattern

Figure 3-20: Typical images of tensile damage parameter (*FI*1) in 0° ply for the three kinds of UACS laminates at or near their maximum loads.

Typical stress-strain curves of the three kinds of the UACS laminates are compared to those obtained from the previous experiments [16] in Fig. 3-21. The stress is the average value of the tensile stress on the cross section of the laminate. It is seen that the numerical analysis predicts almost the same stress-strain curves as those obtained from the previous experiments. The UACS laminate with bi-angled slit distribution gives the highest stiffness, strength, and failure strain, while the UACS laminate with continuous slit distribution gives the lowest values.

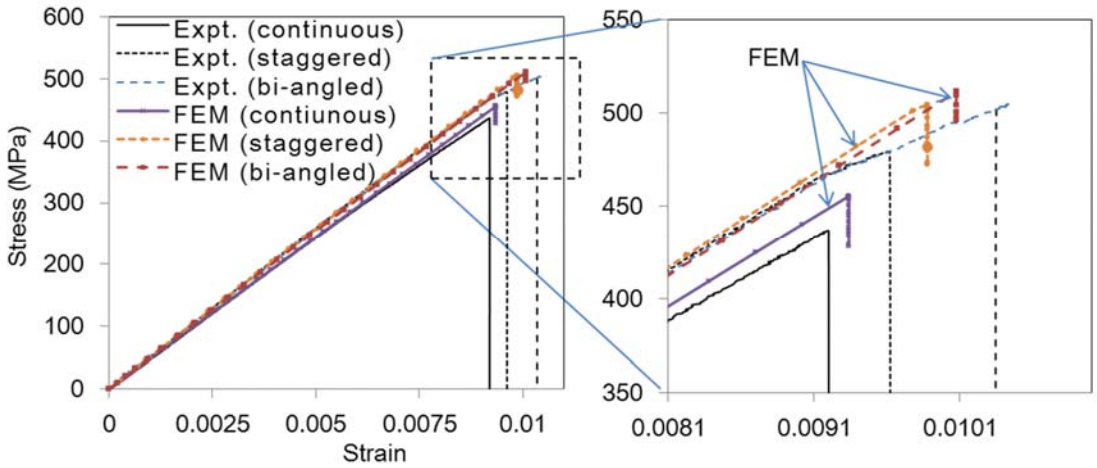

Figure 3-21: Typical stress-strain curves obtained from FEM analysis and the previous experiments.

The detail values of strength and failure strain are listed in Table 3-4 and Fig. 3-22 and Fig. 3-23. The errors between the numerical predictions and the experimental results are in the ranges of 2.4% to 5.3% for the strength, and 1.0% to 2.9% for the failure strain, respectively. Numerical results agree well with the experimental values and the errors are in the reasonable ranges. However, on the other hand, from the right enlarged plot in Fig. 3-21, it is observed that the stress-strain curves at high stress level obtained from the analysis deviate from those obtained from the experiments. This fact means that the present multiscale analysis is not efficient to accurately predict the reduction of the stiffness due to the delamination and fiber breakage in the newly designed UACS laminates with staggered and bi-angled slit distribution patterns. Further study is necessary to improve the prediction accuracy of the multiscale analysis.

Table 3-4: Results of the strength and failure strain of the three kinds of UACS laminates obtained from the multiscale FEM analysis and previous experiments.

	Continuous	Staggered	Bi-angled
Strength			
FEM (MPa)	455.4	504.4	511.4
Experiment (MPa)	435.6	478.8	499.6
Error (%)	4.5	5.3	2.4
Failure strain			
FEM (%)	0. 93	0. 99	1.01
Experiment (%)	0. 95	0. 98	1.04
Error (%)	2.1	1.0	2.9

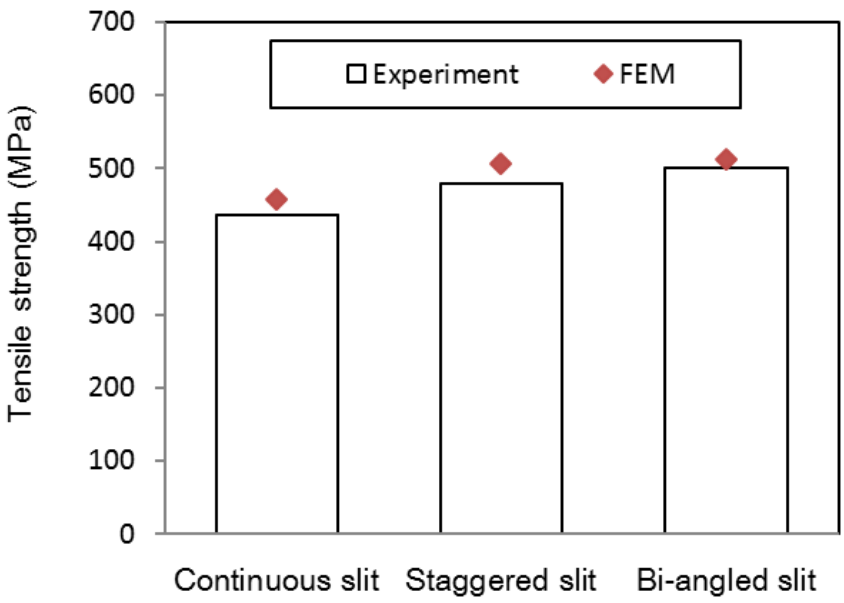

Figure 3-22: Comparison of experimental tensile strength with damage progression analysis for various UACS quasi-isotropic laminates.

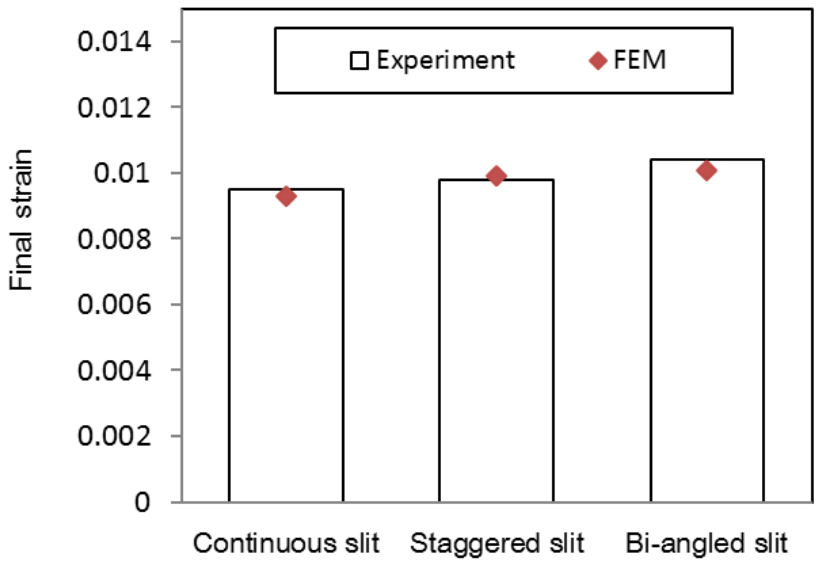

Figure 3-23: Comparison of experimental final strain strength with damage progression analysis for various UACS quasi-isotropic laminates.

3.6 Summary

In this chapter, a multiscale FEM model is proposed and a multiscale analysis is implemented to investigate the damage progression in the three kinds of UACS quasi-isotropic laminates under tension and the effects of the slit distribution patterns. The multiscale analysis includes a homogenization analysis and a damage progression analysis. The homogenization analysis is conducted to predict the elastic constants of the three kinds of UACS laminas. The damage progression behavior in the UACS laminates is simulated by employing the cohesive element and the maximum stress criterion. Based on the present analysis, the following conclusions are obtained.

1. Homogenization analysis method is available for predicting the effective elastic constants of UACS laminas with various periodic slit distribution patterns. The present multiscale analysis model is valid for the damage progression analysis of laminates with

complex microstructures in a reasonable computation cost. Numerical results are in good agreement with those obtained from previous experiments.

2. Numerical results reveal the damage progression manners of the three UACS laminates with different slit distribution patterns. The tensile failure initiates in the slits of 0° plies firstly, next the matrix cracks occur in the 90° plies, then the matrix cracks appear in ±45° plies, subsequently the delamination occurs and progresses around the cracked slits, finally the laminates fails due to the delamination progression or both the delamination progression and the breakage of the fibers in 0° plies. The delamination progression plays a dominant role in the final failure of the UACS laminates.

3. Discontinuous and non-uniform slit distribution in the two newly designed UACS laminates play a positive role in suppressing the delamination progression in the outside regions around the ends of discontinuous slits compared to the UACS laminates with continuous slit distribution. Especially, the newly designed UACS laminate with bi-angled slit distribution has the best material properties including the stiffness, strength, and formability among the three kinds of UACS laminates. Furthermore, the bi-angled slit distribution maintains the orthotropic material symmetry of the original intact prepreg, which is convenient for the design and fabrication of UACS structure components.

4. On the other hand, from the right enlarged plot in Fig. 3-21, it is realized that the present multiscale FEM analysis is not efficient to accurately predict the reduction of the stiffness due to the delamination and fiber breakage in the two newly designed UACS laminates with staggered slit and bi-angled slit distribution patterns. Further study is necessary to improve the prediction accuracy of the multiscale analysis.

Bibliography

[1] Taketa I, Sato N, Kitano A, Nishikawa M, Okabe T. Enhancement of strength and uniformity in unidirectionally arrayed chopped strands with angled slits. *Composites Part A: Applied Science and Manufacturing,* 2010; 41(11): 1639-1646.

[2] Li H, Wang WX, Takao Y, Matsubara T. New designs of unidirectionally arrayed chopped strands by introducing discontinuous angled slits into prepreg. *Composites Part A: Applied Science and Manufacturing,* 2013; 45(2): 127-133.

[3] Lee HK, Simunovic S. Modeling of progressive damage in aligned and randomly oriented discontinuous fiber polymer matrix composites. *Composites Part B: Engineering,* 2000; 31(3): 77-86.

[4] Lee HK, Simunovic S. A damage constitutive model of progressive debonding in aligned discontinuous fiber composites. *International Journal of Solids and Structures,* 2001; 38: 875-895.

[5] Yashiro S, Ogi K. Fracture behavior in CFRP cross-ply laminates with initially cut fibers. *Composites Part A: Applied Science and Manufacturing,* 2009; 40(6-7): 938-947.

[6] Benssousan A, Lions JL, Papanicoulau G. Asymptotic Analysis for Periodic Structures. Amsterdam: North-Holland, 1978.

[7] Scanchez-Palencia E. Non-homogeneous Media and Vibration Theory. Lecture Notes in Physics. Berlin: Spring Verlag, 1980.

[8] Bakhvalov NS, Panasenko GP. Homogenization in Periodic Media, Mathematical Problems of the Mechanics of Composite Materials. Moscow: Nauka, 1984.

[9] Bendsoe MP, Kikuchi N. Generating optimal topologies in structural design using a homogenization method. *Computational Methods in Applied Mechanics and Engineering,* 1988; 71(1): 192-224.

[10] Guedes JM, Kikuchi N. Preprocessing and postprocessing for materials based on the homogenization method with adaptive finite element methods. *Computational Methods in Applied Mechanics and Engineering,* 1990; 83: 143-198.

[11] Hassani B, Hinton E. A review of homogenization and topology optimization I-homogenization theory for media with periodic structure. *Computers & Structures* 1998; 69: 707-717.

[12] Jansson S. Homogenized nonlinear constitutive properties and local stress concentrations for composites with periodic internal structure. *International Journal of Solids and Structures,* 1992; 29: 2181-2200.

[13] Wang WX, Luo DM, Takao Y, Kakimoto K. New solution method for homogenization analysis and its application to the prediction of macroscopic elastic constants of materials with periodic microstructures. *Computers & Structures,* 2006; 84(6): 991–1001.

[14] Luo DM, Wang WX, Takao Y. Effects of the distribution and geometry of carbon nanotubes on macroscopic stiffness and microscopic stresses of nanocomposites. *Composite Science and Technology,* 2007; 64(11): 2947-2958.

[15] Krueger R. The virtual crack closure technique: history, approach and applications. *NASA/Contractor Report-2002-211628*, 2002.

[16] Turon A, Dávila CG, Camanho PP, Costa J. An engineering solution for mesh size effects in the simulation of delamination using cohesive zone models. *Engineering Fracture Mechanics*, 2007; 10(74): 1665-1682.

[17] Mi Y, Crisfield MA, Davies GAO, Hellweg HB. Progressive delamination using interface elements. *Journal of Composite Materials,* 1998; 32: 1246-1272.

[18] Alfano G, Crisfield MA. Finite element interface models for the delamination analysis of laminated composites: mechanical and computational issues. *International Journal for Numerical Methods in Engineering, 2001*; 50:1701-1736.

[19] Chen J, New application of decohesive model with mixed damage scale in fracture analysis of composite materials. *Fatigue & Fracture of Engineering Material & Structures,* 2001; 24: 761-769.

[20] MSC.Marc User manual, *Volume A: Theory and User Information*, 2010: 529-533.

CHAPTER 4

Size effects in tensile properties of newly designed UACS laminates

In this chapter, the size effects in tensile testing of UACS laminates with different slit distribution are investigated by experiment and FEM analysis. For all cases of UACS laminates, tensile specimens with six different widths are fabricated and tested. Additionally, multiscale analysis based on the FEM software of above specimens is conducted to reveal the effects of specimen width on the damage progression in UACS laminates with different widths.

4.1 Introduction

The size effect is defined as a change in strength with specimen dimensions, and this phenomenon is well-known to exist in composites [1-4]. It is important to consider the size effects in scaling up from small coupon tests to full scale structures in design of composite structures.

Several studies have shown size effects in mechanic properties of composite laminates [5-11]. It is very complicated to reveal the size effects because of the different failure mechanisms, and the possibility of interaction of matrix cracking and delamination with fiber direction failure. Jackson et al. [5-6] carried out tests changing all three dimensions together using ply level scaling on AS4/3502 carbon-epoxy specimens with cross-ply, angle-ply and quasi-isotropic lay-ups. Of particular relevance are tests on $[45_m/-45_m/0_m/90_m]_S$ laminates with *m* varying from 1 to 4. A significant size effect was found, with the strength reducing by 28% over the factor of four increases in linear dimensions. The failure strains however apparently increased. There was also a change in mode from a localized fracture for the smaller specimens to more extensive fracturing throughout the specimen for the larger ones. Johnson et al. [7] carried out sublaminate level scaled tension tests on AS4/3502 carbon fiber/epoxy with cross-ply, angle-ply and quasi-isotropic laminates including the same $[45/-45/0/90]_{nS}$ stacking sequence. The number of blocks of repeated plies, *n*, was varied from 1 to 4, with specimen widths and lengths scaled in proportion. The results actually showed an increase in strength from the smallest to the other sizes, which all gave quite similar results. This was attributed to the smallest specimens being more susceptible to free edge delamination. Wisnom et al. [8] carried out tensile tests on $[45/-45/0/90]_{nS}$ fabricated by Hexcel IM7/8552 carbon

fiber/epoxy when *n* varied from 1 to 4. All the dimensions, namely gauge length, width, and thickness, of the tensile specimens were scaled. The strength results showed an increase with specimen size and the largest specimens failed at 10% higher stress than the smallest ones.

There are many factors influencing size effects of composites, including material microstructure, stress gradients, testing consideration and free edge effects. Among them, free edge effects derive from very high interlaminar stresses arising at the free edge of a laminate with different ply orientations. This phenomenon was studied from the work of Pipes and Pagano [12] onwards. In some laminates it leads to premature failure initiating at the free edge. The effects of free edges on in-plane failure are less well understood, but could be significant for many layups and types of loading. For example Berbinau and Wolff [13] argue that interlaminar stresses at the free edge are important in initiating compressive failure in [0/± θ] laminates.

As described in chapter 2 and chapter 3, delamination is the most significant damage mode in the failure of UACS laminates with different patterns slit distribution. This feature implicates that the UACS laminates which are very dependent on the occurrence and extension of delamination may be sensitive to specimen sizes. In order to investigate the size effects of UACS laminate with newly designed slit distribution, tensile experiments and damage progression analysis of UACS laminates with five specimen widths are conducted in this chapter.

4.2 Tensile experiment of UACS laminates with different widths

4.2.1 Fabrication and tensile experiment

As the same as the tensile experiment described in chapter 2, conventional CFRP prepreg of PYROFIL (TR50S) (Mitsubishi Rayon) is used in this experiment. Material properties of this prepreg are listed in Table 3-1. The thickness of the separate lamina is 0.2 mm. The prepregs for 0°, 45°, 90° and -45° are cut into the sheets of 200 mm × 200 mm. The slit angle between the slit and the fiber direction is 11.3 degrees and the length of chopped strands is 25 mm, which are the same as the UACS prepregs shown in Fig. 2-3. Next, existing continuous slits pattern, newly designed discontinuous staggered slits pattern and bi-angled slits pattern are introduced into the prepreg by the hand-made cutting method, respectively. After introduced the slits, the UACS prepregs are stacked into the sequence of $[45/-45/0/90]_S$. Afterwards, stacked laminates are cured using a autoclave and the cure temperature and pressure are also the same as the curing procedures described in chapter 2.

After cure, the quasi-isotropic UACS laminates with different patterns slit distribution are cut into tensile specimens of 200 mm in length using the diamond cutter, with five widths including 10 mm, 15 mm, 20 mm, 30 mm, 40 mm. Fig 4-1 shows the schematic of tensile specimens, GFRP tabs of glass-fiber cloth/epoxy of 40 mm in length are adhered on two sides of the specimens. The thickness of the specimens is 1.6 mm. The gauge length of all the specimens is 120 mm and strain gauges of 10 mm in length are bonded at the centers of the two surfaces of the specimens. For all cases of three kinds of UACS specimens with five widths, 4 tensile specimens are fabricated and tested for each case. In other words, 60 tensile specimens in total are conducted in this experiment. Material-

testing system MTS 810 is employed to conduct the tensile tests and the crosshead speed is 0.5 mm/min.

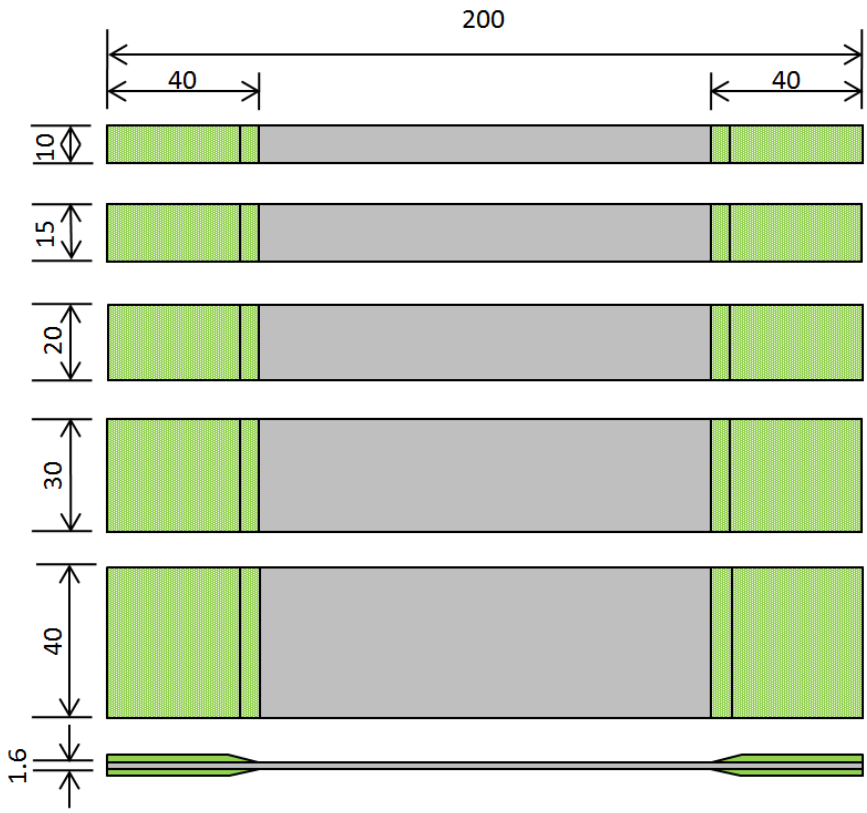

Figure 4-1: Schematic of tensile specimens with different widths.

4.2.2 Experimental results

Test results of UACS specimens with different widths are presented in Fig. 4-2 to Fig. 4-5 and Table 4-1. Tensile strength of various patterns UACS specimens with different widths are presented in Fig. 4-2. It is worth mentioning that the data of the UACS laminates of 25 mm in width is according to the tensile results of laminate of $[45/-45/0/90]_{2S}$ described in chapter 2. Final strength obviously increases when the specimen width vary from 10 mm to 25 mm. Tensile strength tends to a stable level while the width

of the specimens larger than 25 mm. The UACS laminate with bi-angled slit distribution presents the highest strength values and the continuous slits distribution presents the lowest in all cases of widths of specimens, which is consistent with the test results in chapter 2. Compared with UACS laminate with continuous slit distribution, tensile strength of UACS laminates with two newly designed slit distributions increase rapidly with the specimen width varying from 10 mm to 40 mm. For three kinds of UACS laminates, the increasing rates are 18.3%, 26.2% and 26.7%, respectively. These results reveal that the specimen size has significant influence on the tensile properties of cases of UACS laminates.

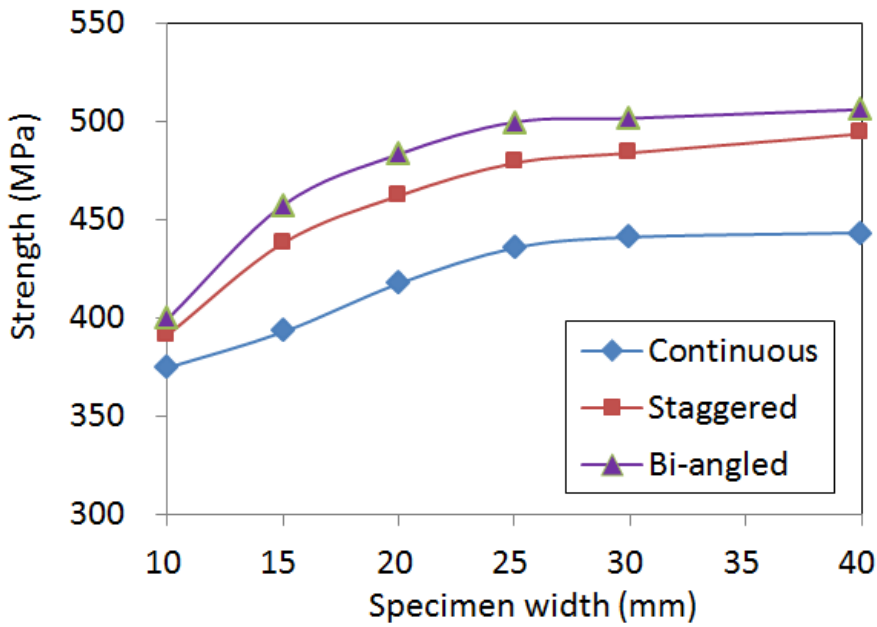

Figure 4-2: Tensile strength of UACS laminates with different widths.

Typical stress-strain curves and the values of strength and longitudinal modulus for bi-angled slit pattern UACS laminate with different widths are presented in Fig. 4-3 and Table 4-1. It is seen that nonlinear behavior near the peak values is obvious in all the

curves and that the nonlinear range becomes larger with the width of specimens becomes larger. The nonlinear behavior is considered to reflect the delamination between 0° ply and its adjacent plies before the occurrence of fiber breakage of 0° plies, which will be analyzed in detail later. Short nonlinear range means that the final failure happens immediately following the delamination occurring, especially when the width of the specimen is less than 25 mm. For a comparison in detail, the values of tensile strength and modulus for UACS laminates with bi-angled slits distribution and different widths are listed in Table 4-1. Dramatic increasing can be seen when the specimen width varies from 10 mm to 15 mm. These features are consistent with that reported in the previous experimental research [8] due to the influence of the stress singularity at the edges of the laminates. It is speculated that the ratio of the influence area of the stress singularity at the edge and the specimen width play an important role for the increase of the strength with the increasing of specimen width. Small ratio means that the influence of the edge stress singularity is weak, and consequently leads to high strength. The tensile strength value increases to nearly 500 MPa when the specimen width reaches 25 mm. Then the strength tends to reach a constant value when the specimen width increases beyond 25 mm. This fact indicates that the influence of the edge stress singularity becomes very weak. In contrast, the tensile modulus values of UACS laminate with bi-angled slits distribution display slight increase as the specimen width varies from 10 mm to 25 mm. This fact reveals that the width influence on the tensile modulus of UACS laminates is not as significant as on the tensile strength.

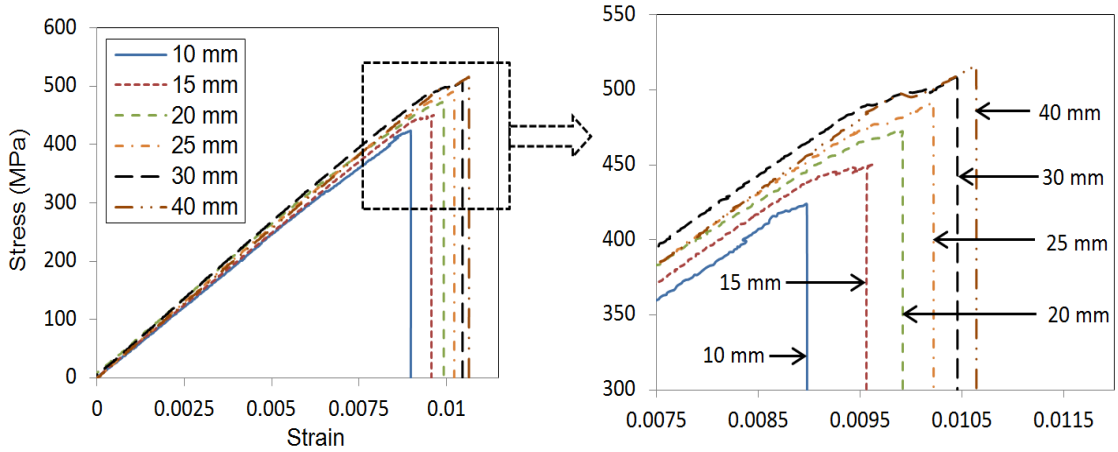

Figure 4-3: Typical stress-strain curves of bi-angled slit distribution UACS laminate with different width.

Table 4-1: Strength and longitudinal modulus of UACS laminate with bi-angled slits distribution and with different widths.

Specimen width (mm)	Strength (MPa)	Modulus (GPa)
10	399.29	47.93
15	457.37	49.61
20	483.34	49.66
25	499.64*	50.10*
30	501.65	50.07
40	506.09	49.94

* Tensile results of $[45/-45/0/90]_{2S}$ in Chapter 2

Typical images of fractured specimens of UACS laminates with bi-angled slits distribution are shown in Fig. 4-4. In the case of specimen with 10 mm in width, the failure mode of 0° plies is obvious a pull-out mode and no fiber breakage in 0° plies can be seen. Compared with the failure mode of 0° plies in the specimen with 10 mm in width, the images of the fractured specimens with 20 mm and 30 mm in width show a little different failure behavior. Many fibers in 0° plies are broken under tension and

relatively few pull-out failure modes are seen. These facts indicate that the fibers in 0° plies still can sustain the load even though delamination occurred when the specimen have relative large width, these failure behavior may be related to the nonlinear portion in the stress-strain curves. Large area of delamination and no fiber breakage result in relatively small nonlinear portion before final failure in the specimen with 10 mm in width. It is noted that similar effects of the specimen width on the tensile properties of the UACS laminates with discontinuous staggered angled slits and with continuous angled slits are obtained. For the simplicity, only the results of the UACS laminates with discontinuous bi-angled slits are discussed here and afterward.

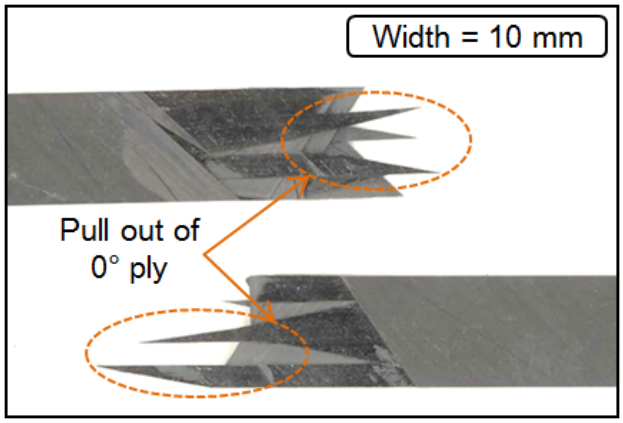

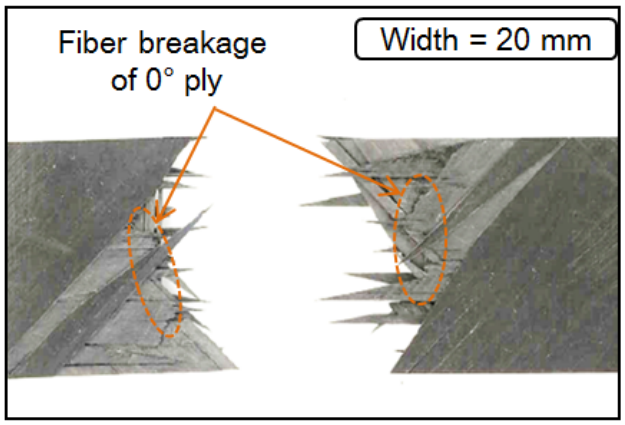

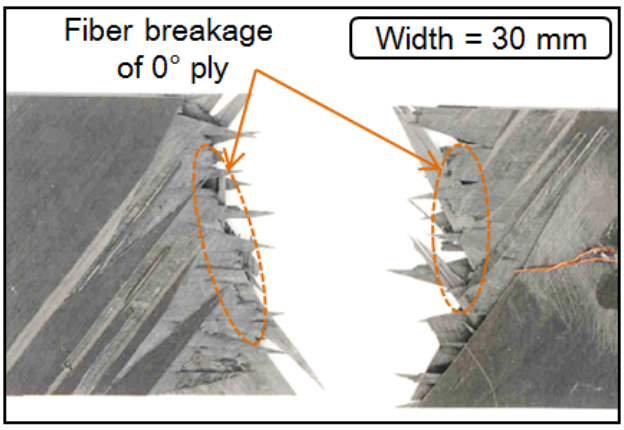

Figure 4-4: Typical images of fractured specimens of bi-angled slit distribution UACS laminates with different widths.

To further investigate the damage development in the UACS laminate, the cross-section 10 mm away from the fracture section of a specimen with the bi-angled slits and with 40 mm in width is polished by sand paper and the polished surface is observed using an optical microscope. Three representative locations A, B and C are observed in detail, as shown Fig. 4-5. Remarkable and penetrable delamination between 0° ply and adjacent -45° ply is observed near the free edge in location A. Location B presents the damage near the slit in 0° ply. It is seen that delamination occurs from the cross points of the slit and the interface and then extends from the slit area to both opposite directions simultaneously. The left side of the delamination between the 0° ply and adjacent -45° ply connects with the delamination shown in the Fig. 4-5A. However, the delamination does not extend a long distance. Similar phenomenon is observed at the location C. From the observation of at the three cross-section locations, it is supposed that large delamination easily initiates and extends near the edge of the specimen, but it is not so easy for the delamination to grow into the specimen along the width direction since the

stress concentration at the edge or at the slit tip is limited in a very small area. Therefore, if the specimen width is too small the ratio of the stress concentration area and the specimen width becomes relatively large, which means the influence of the stress concentration becomes significant.

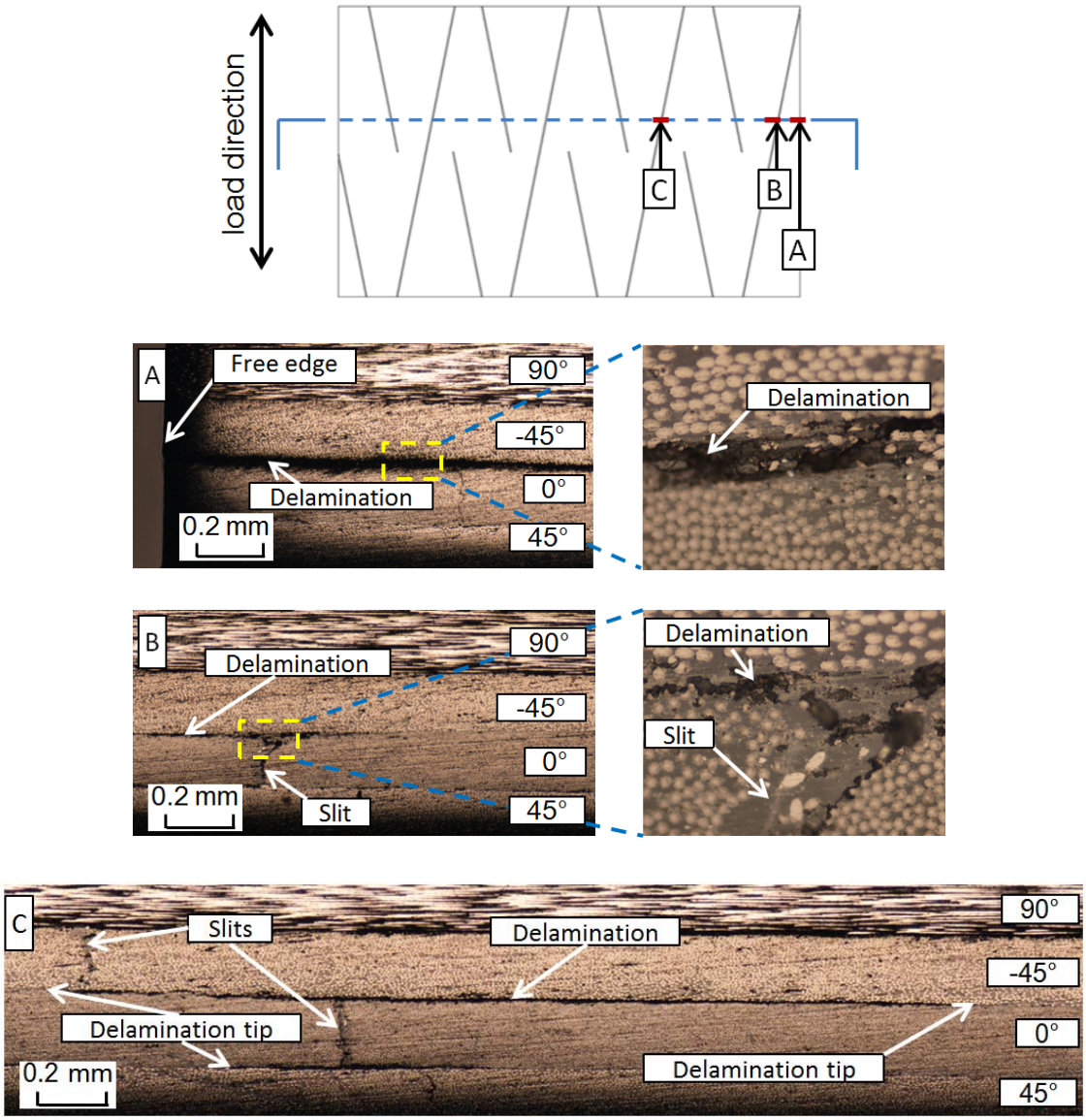

Figure 4-5: Cross-section images of a specimen with bi-angled slits and with 40 mm in width after tension.

4.3 Multiscale analysis of damage progression in UACS laminates with different widths

Significant effects of the specimen width on the tensile strength of the UACS laminates are revealed in the last subsection. In this subsection, a multiscale analysis is conducted to further investigate width effects in the damage progression of UACS laminates with different widths.

4.3.1 Multiscale FEM models

Multiscale FEM models for present analysis are made referring to the multiscale model created in subsection 3.2. A typical model with 15 mm in width and with bi-angled slits is shown in Fig. 4-6. The model represents the central region in the gauge length of the tensile specimens tested in the last subsection. The size of the model is 25 mm in length and 1.6 mm in thickness. Similar to the multiscale model developed in chapter 3, the model consists of top four microscopic plies and one macroscopic layer for the simulation of a quasi-isotropic UACS laminate [45/0/-45/90]s. The top four plies precisely model the slit distribution, the width of all the slits is 0.1 mm, and the length scale used for controlling the size of elements is 1 mm similar to the previous model used in subsection 3.2. The models for the specimens with other four widths (10 mm, 20 mm, 30 mm and 40 mm) are similar to the model shown in Fig. 4-6, except for different width. For the sake of convenience, the multiscale models for specimens with bi-angled slits and with 10 mm, 15 mm, 20 mm, 25 mm, 30 mm and 40 mm in width are named as B10, B15, B20, B25, B30 and B40 in short, respectively. The same material constants of CFRP and epoxy listed in Table 3-1 in Chapter 3 are used. Cohesive interface elements are inserted

into the interface 1 between 45° and 0° plies and the interface 2 between 0° and -45° plies to reveal the interlaminar damage in UACS laminates. The bilinear constitutive constants of the cohesive interface elements listed in Table 3-2 in Chapter 3 are used. The elastic constants of UACS laminas obtained from the homogenization analysis conducted in the Chapter 3 are used for the present macroscopic layer [90/-45/0/45].

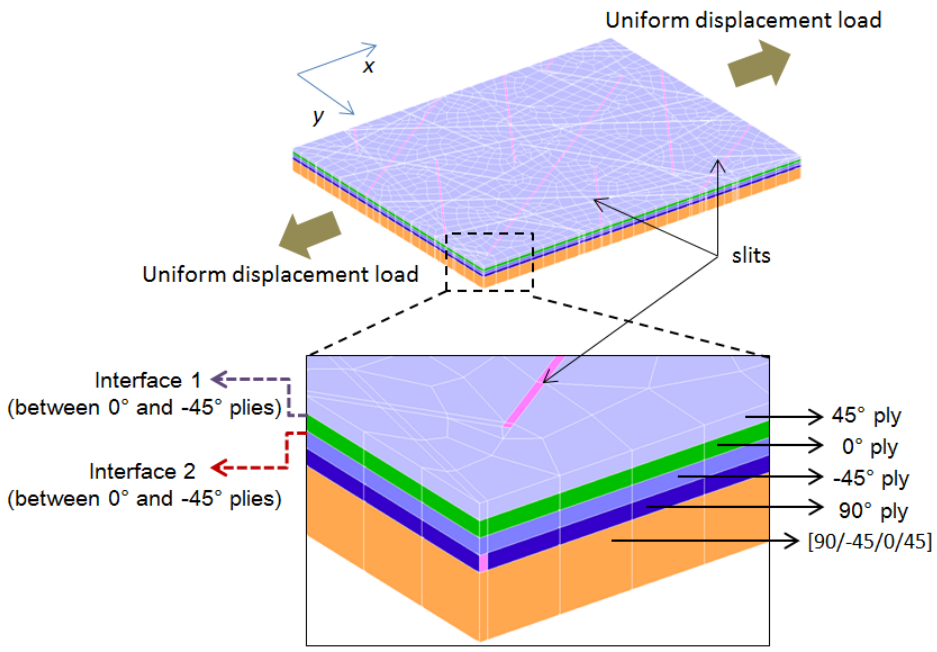

Figure 4-6: The multiscale FEM model of B15 for damage progression analysis.

Similar to the multiscale analysis, the interlaminar damage is expressed by the damage parameter *d*, and maximum stress criterion is employed to simulate the failure in CFRP and slits. Uniform incremental displacement loading is applied to the edges of the model, as depicted in Fig. 4-6, incremental loading steps and iterative schemes are adopted in the damage progression analysis. In the case of interface failure, the stiffness reduction is imposed following the bilinear rule. In the case of failure occurred in CRRP regions, the

corresponding components of the stiffness tensor of the element related to corresponding failure index are reduced to 1% of the original value after failure occurring. However, in the slit regions, the modulus is reduced to 1% of its original value after failure occurring because the slit region is considered to fill by isotropic epoxy resin. In all the models, eight-node solid elements are used for all the elements including the cohesive interface elements. The commercial FEM software of MSC.MARC 2010 is employed in the analysis.

4.3.2 Numerical results

Numerical results obtained from the damage progression analysis of UACS laminates with different widths are presented in Fig. 4-7 to Fig. 4-15, Table 4-2 and Table 4-3. It is noted that only the results related to the UACS laminate with bi-angled slits are presented here, except for Table 4-3, for the sake of simplicity because similar results are obtained for the UACS laminates with discontinuous staggered angled slits and with continuous angled slits. The variation of the tensile failure $FI1$ in the slits of 0° plies of models B10 to B40 is depicted in Fig. 4-7. The value of vertical axis denotes the maximum value of the index $FI1$ in the slits of 0° plies of each model corresponding to each incremental load step. The slit failure occurs under a relative low load less than 200 MPa in all the models. The $FI1$-stress curves for different widths display slight difference. These reveal that the failure in the slits of 0° plies is approximately independent of the laminate widths.

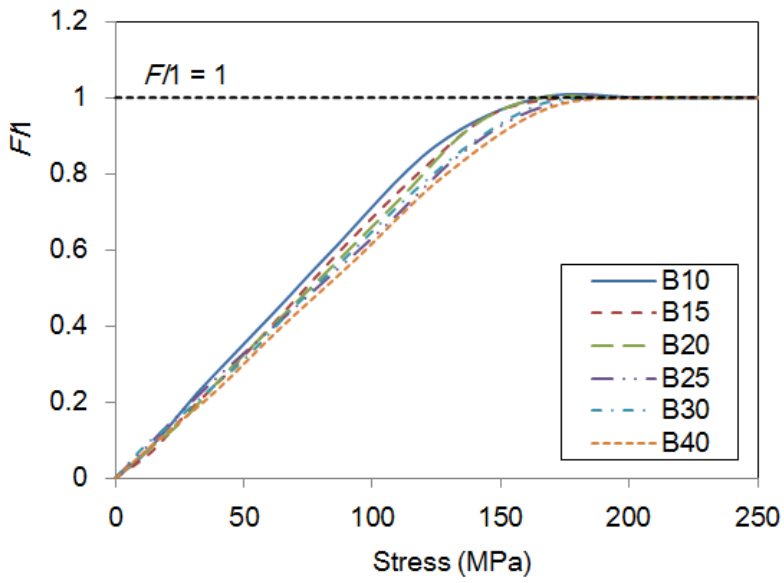

Figure 4-7: Variation of tensile failure index *FI*1 in the slits of the 0° plies of bi-angled slit distribution UACS laminates with different widths.

The critical stresses for various failure modes occurred in the UACS laminates with bi-angled slits are listed in Table 4-2 for various widths. In all cases, slit failure in 0° plies occurs at first under the relatively low stresses. Subsequently, matrix cracking occurs in 90° and ±45° plies as the tensile load increases. Then, delamination between 0° and its adjacent ±45° plies occurs when the stress is larger than 400 MPa. Fiber breakage is observed only in the models of B25, B30 and B40 at the stress level near their final strength. It is noted that the critical stress values for the occurrence of matrix cracking in 90° and ±45° plies are almost at the same level. This indicates that the slit failure in 0° plies and matrix cracking in 90° plies and ±45° plies are approximately independent of the specimen width. In contrast, the critical stress values for the delamination occurrence in the specimens with different widths are quite different, and high critical stress is

related to large specimen width. These numerical results are consistent with the experimental results described in subsection 4.2.

Table 4-2: Critical stresses for various failure modes occurrence in bi-angled slit distribution UACS laminates.

Critical loads for various failure modes	B10	B15	B20	B25	B30	B40
Slits failure in 0° plies (MPa) (*FI*1 = 1)	165.0	173.9	165.2	183.9	191.3	199.0
Matrix cracking in 90° plies (MPa) (*FI*2 = 1)	245.9	244.9	245.8	235.3	241.1	249.5
Matrix cracking in ±45° plies (MPa) (*FI*2 = 1)	316.3	320.7	326.3	311.3	318.9	330.4
Delamination occurs (MPa) (*d* = 1)	408.1	442.0	459.8	479.1	481.1	487.5
Fiber breakage in CFRP of 0° ply (MPa) (*FI*1 = 1)				509.4	511.6	513.1
Final fracture (Maximum load) (MPa)	417.3	466.3	496.9	509.4	523.7	526.7

Typical images of tensile failure index *FI*1 in the 0° ply of B20 at the stress level of 192.05 MPa is presented in Fig. 4-8. *FI*1 value in the slit regions shows apparently larger than the surrounding CFRP regions (lower than 0.4) due to the significant difference in longitudinal stiffness. It is mentioned that the *FI*1 value in the slit regions near the free edge is obvious larger than in other regions due to the stress concentration at the edge.

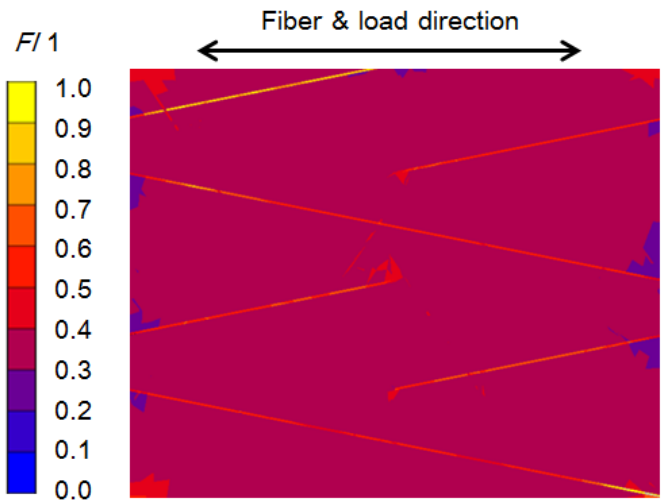

Figure 4-8: Typical images of tensile failure index *FI*1 in the 0° ply of B20 under the stress level of 192.05 MPa.

Typical stress-damage (*d*) curves of the interface 1 between the 45° and 0° plies of the model B10 to B40 are presented in Fig. 4-9. The vertical axis denotes the maximum value of the interface damage for each model at each incremental load step. It is seen that the values of the interfacial damage parameter *d* of all the models increase very slowly at relatively low stress level. However, after the stress increases beyond 350 MPa, the values of the damage parameter *d* in all the models increase rapidly. This is because that near this stress level, three kind of failure modes including slits failure in 0° plies, matrix cracking in 90° and ±45° plies have occurred, according to the critical stresses of failure occurrence listed in Table 4-2. In addition, the increasing rates of the interfacial damage for the cases of B10, B15 and B20 are obvious much larger than other three cases, which have intimate relation with the final failure stresses.

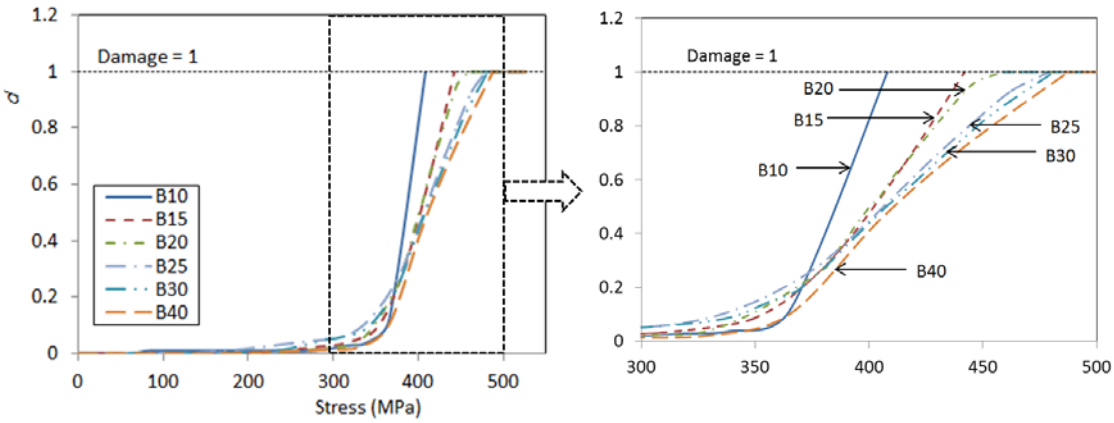

Figure 4-9: Typical stress-damage (*d*) curves of the interface 1 in various damage progression analysis models for UACS laminates with bi-angled slit distribution.

Images of interfacial damage of interface 1 at different load levels for models of B10, B20 and B40 are presented in Figure 4-10 for a comparison. In the case of B10, apparent delamination regions are observed near the slits which closed to the free edge when the tensile strain is 0.0086. No delamination occurrence is observed in the other discontinuous slits that are far away from the free edge. Similar phenomenon is displayed in the cases of B20 and B40. Large delamination occurs near the free edge and around the cross points of slits of adjacent plies. It is also noted that the strain levels for different cases are quite different due to the sizes effects on the interfacial damage of UACS laminates.

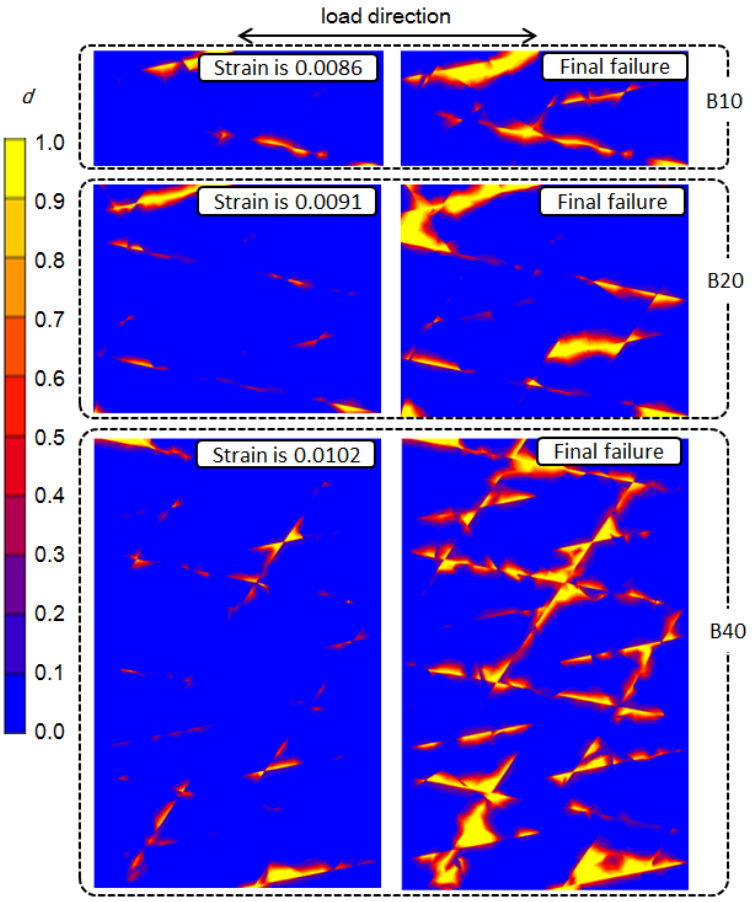

Figure 4-10: Comparison of damage images (*d*) for interface 1 in B10, B20 and B40 under different load levels.

In Fig. 4-11, the area of delamination calculated at each load level for the above three models are presented. The vertical axis denotes the percentage of the delamination area in the interface 1. In the case of B10, delamination occurs at the strain of 0.008 and the area of the delamination increases suddenly at the strain of 0.0085. The critical strain for the sudden increase of the delamination increases with the increase of the specimen width. In the case of B40, the delamination area has slight change before the strain of 0.01. Furthermore, the percentage of the areas of delamination over the whole interface area at the final failure are also quite different for the three cases, large percentage is seen for the

case of small specimen width. These facts are also consistent with the experimental results depicted in Fig. 4-4.

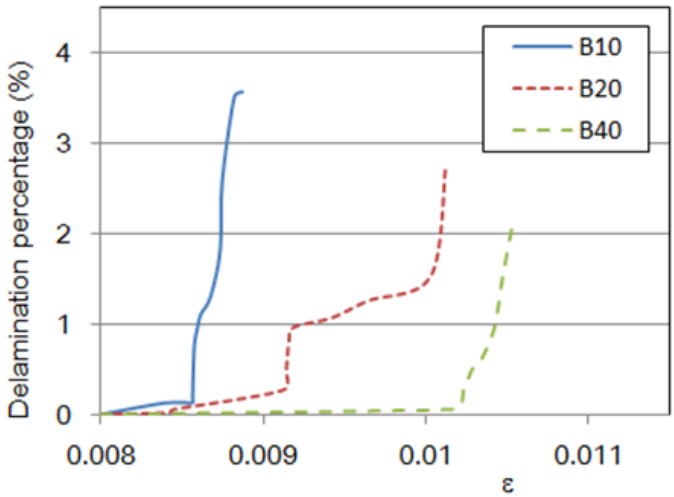

Figure 4-11: The strain-delamination proportion curves of the interface 1in B10, B20 and B40.

In order to visualize the damage progression at different locations of interface, typical strain- damage (*d*) curves of three representative elements in the interface 1 of model B40 is shown in Fig. 4-12. The locations of three representative elements named element A, B and C are shown in left graph of Fig. 4-12, the distances between the elements and the free edge are 2.5 mm, 12.5 mm and 22.5 mm, respectively. Damage value (*d*) of the related elements is the average value of its eight nodes at each incremental load step. Compared with element B and C, the damage value in element A is obviously larger at relatively low loads than other two elements. In contrast, the damage values in the element B and C suddenly increase after the load reaches a critical strain at a very high load level. This indicates that very high interlaminar stresses exist near the free edge of the UACS laminates under tension.

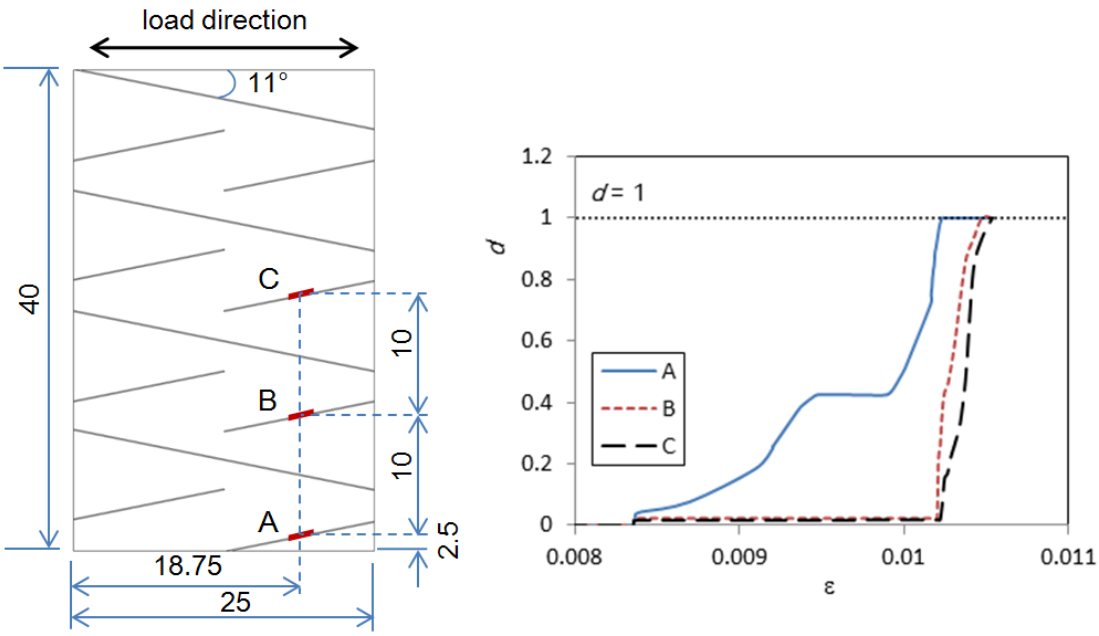

Figure 4-12: Typical strain-damage (*d*) curves of the representative elements in interface 1 of B40.

Fig. 4-13 presents the comparison of strain-delamination percentage curves of interface 1 between 45° and 0° plies and interface 2 between 0° and -45° plies in the model B40. Two curves show similar trend, except for the final delamination percentage at the failure strain. The reason for the different final delamination percentage is supposed to be that the interface 2 is relatively far away from the top surface of the laminate compared to interface 1, as shown in Fig. 4-6.

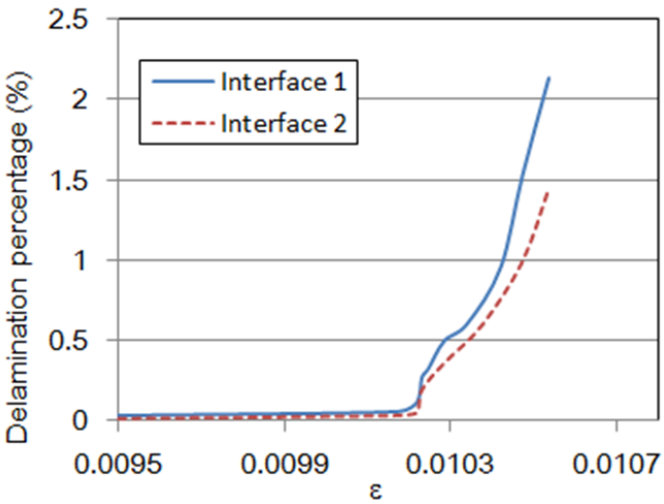

Figure 4-13: Comparison of strain-delamination proportion in interface 1 and interface 2 in B40.

Typical image of the failure index *FI*1 in the 0° ply of B40 at the stress level of 513.1 MPa is presented in Fig. 4-14 to investigate the fiber breakage occurrence. Very high value of *FI*1 is observed in the small regions around the slit ends of the 0° ply. The very high value of *FI*1 implicates that the fiber breakage may occur in these regions due to the high longitudinal stress. On the other hand, large area with small value in blue color is shown in Fig. 4-14, which indicates the relaxation of tensile stress due to the delamination occurrence around the slits.

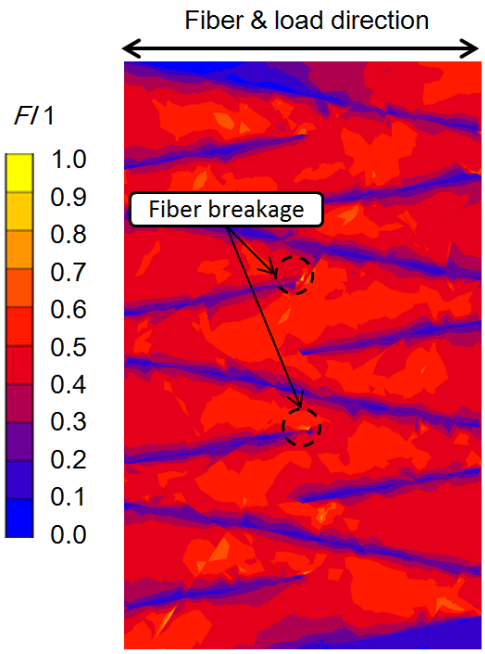

Figure 4-14: Typical images of the failure index *FI*1 in the 0° ply of B40 at the stress level of 513.1 MPa.

Typical stress-strain curves for all cases of B10 to B40 are summarized in Fig. 4-15. Linear behavior is seen at the relatively low stress for all cases. Nonlinear behavior is shown in B10 at first when the stress is beyond 300 MPa, the reason is that all matrix failure modes including slit cracking in 0° plies and matrix cracking in ±45° plies occurs after this load level according to Table 4-2. From the enlarged image, it is seen that the specimens with width larger than 25 mm can sustain further loads even though the delamination has occurred.

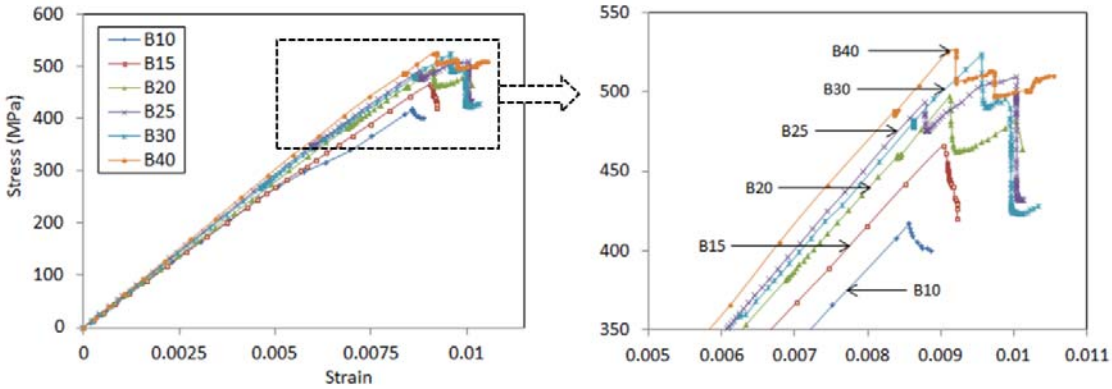

Figure 4-15: Typical stress-stain curves obtained from FEM analysis of B10 to B40.

Table 4-3 summarized the all results of strength obtained from experiment and FEM analysis for all kinds of specimens for a comparison. The errors between the numerical predictions and the experimental results are in the ranges of 1.9-6.2%. It is seen that numerical results agree well with the experimental values and the errors are in the reasonable ranges. Damage progression analysis results indicate that in all cases of UACS laminates with continuous, staggered and bi-angled slit distribution under tension, effects of specimen size on the strength of the all cases of laminates are significant. Specimens with different widths show different damage progression behavior and different final strength values.

Table 4-3: Results of the strength obtained from the multiscale analysis and experiments.

Width (mm)	10	15	20	25	30	40
continuous						
Experiment (MPa)	374.6	392.8	417.4	435.6*	441.1	443.3
FEM	391.4	417.0	437.6	451.3	466.1	469.1
Error (%)	4.5	6.2	4.8	3.6	5.7	5.8
Staggered						
Experiment (MPa)	391.3	438.1	462.1	478.8*	484.0	493.7
FEM	412.3	456.6	487.8	498.7	507.3	515.7
Error (%)	5.4	4.2	5.6	4.2	4.8	4.5
Bi-angled						
Experiment (MPa)	399.3	457.4	483.3	499.6*	501.7	506.1
FEM	417.3	466.3	496.9	509.4	523.7	526.7
Error (%)	4.5	1.9	2.8	2.0	4.4	4.1

* Tensile results of $[45/-45/0/90]_{2S}$ in Chapter 2

4.4 Summary

In this chapter, tensile experiment and damage progression analysis of the three kinds of UACS laminates with different widths of 10 mm, 15mm, 20 mm, 30 mm and 40 mm are conducted to investigate the effects of specimen width on the tensile properties of the UACS laminates. Based on the results of experiment and FEM analysis, the following conclusions are obtained.

1. Tensile experimental results indicate that the specimen width has significant influence on the tensile strength of UACS laminates. For all cases of UACS laminates, test strength increases with the specimen width varying from 10 mm to 40 mm. Compared with UACS laminate with continuous slit distribution, the increase ranges of

two kinds of UACS laminates with discontinuous slit distribution are relatively larger than that of UACS laminate with continuous slit distribution. In contrast, the effect of the specimen width on the tensile stiffness of the UACS laminates is not significant.

2. The failure modes are different for specimens with different widths and the breakage of many fibers in 0° plies are observed for specimens with large widths from the experimental and numerical results. On the other hand, no fiber breakage is seen for specimens with small widths and the delamination progression dominates the final failure.

3. Slits failure in 0° plies occurs at first at the relatively low stresses and then the matrix cracking occurs in the 90° and ±45° plies. These three failure modes are approximately independent of the specimen width. In contrast, the specimen width has significant influence on the delamination occurrence and progression, as well as the final strength for the all case of UACS laminates.

4. The stress concentration at the free edge plays a main role for the effects of the specimen width on the tensile properties of the laminates. Large delamination occurs near the free edge and around the cross points of the slits in the 0° ply and adjacent ±45° plies.

Bibliography

[1] Wisnom MR. Size effects in the testing of fibre-composite materials. *Composite Science and Technology,* 1999; 59(13): 1937-1957.

[2] Cunningham ME, Schoulz SV, Toth JM. Effect of end tab design on tension specimen stress concentrations. In: *Recent advances in composites in the United States and Japan,* 1985, *ASTM STP* 864: 253-262.

[3] Hojo M, Sawada Y, Miyairi H. Influence of clamping method on tensile properties of unidirectional CFRP in 0° and 90° directions- round robin activity for international standardization in Japan. *Composites,* 1994; 25(8): 786-796.

[4] Wisnom MR, Maheri MR. Tensile strength of unidirectional carbon fibre-epoxy from tapered specimens. In: *Second European conference on composites testing and standardization*, 1994; Hamburg: 239-247.

[5] Jackson KE, Kellas S. Effect of specimen size on the tensile strength of geometrically scaled $[+\theta_n/\text{minus}\theta_n/90_{2n}]_s$ composite laminates. In: *US Army Symposium on Solid Mechanics,* 1993; Plymouth MA, August.

[6] Jackson KE, Kellas S, Morton J. Scale effects in the response and failure of fiber reinforce composite laminates loaded in tension and in flexure. *Journal of Composite Materials,* 1992; 26(18): 2674–2705.

[7] Johnson DP, Morton J, Kellas S, Jackson K. Scaling effects in sublaminate-level scaled composite laminates. *AIAA J,* 1998; 36: 441-447.

[8] Wisnom MR, Khan B, Hallett SR. Size effects in unnotched tensile strength of unidirectional and quasi-isotropic carbon/epoxy composites. *Composite Structures,*

2008; 84(1): 21-28.

[9] Wisnom MR, Atkinson JW, Jones MI. Reduction in compressive strain to failure with increasing specimen size in pin-ended buckling tests. *Composites Science and Technology,* 1997; 57(9-10): 1303-1308.

[10] Hallett SR, Jiang WG, Khan B, Wisnom MR. Modelling the interaction between matrix cracks and delamination damage in scaled quasi-isotropic specimens. *Composites Science and Technology*, 2008; 68(1): 80-89.

[11] Wisnom MR, Hallett SR. Scaling effects in notched composites. *Journal of Composite Materials* 2010; 42(2): 195–210.

[12] Pipes RB, Pagano NJ. Interlaminar stresses in composite laminates under uniform axial tension. *Journal of Composite Materials*, 1970; 4: 538–548.

[13] Berbinau PJ, Wolff EG. Analytical model for prediction of micro buckling initiation in composite laminates. In: *The 11th International Conference on Composite Materials,* 1997; Gold Coast, Australia: 4289-4299.

[14] O'Brien TK. Characterisation of delamination onset and growth in a composite laminate. In: *Damage in Composite Materials ASTM STP* 775, 1982: 140-167.

CHAPTER 5

Conclusions and future works

This chapter summarizes the main results of this dissertation and predicts the main research topics may concern to this study in future.

5.1 Conclusions

UACS composite is a new type of short fiber reinforced polymer by introducing regular slits into the prepreg before the fabrication of laminates. Existing UACS composites have superior flowability but relatively low tensile strength compared to conventional CFRP. In this study, two kinds of newly designed UACS laminates with enhanced mechanical properties are developed. Tensile properties, flowability, and the size effects in the tensile properties of newly designed UACS laminates are investigated by experiment and numerical analysis.

Based on these works, following conclusions are obtained:

1. Newly designed UACS laminates with staggered slits and bi-angled slits enhance the tensile strength by about 10% and 15%, respectively, compared to the existing UACS laminate with continuous angled slits. In addition, newly designed UACS laminates have better flowability than the existing UACS laminate with continuous angled slits. The UACS laminate with discontinuous bi-angled slits appears to have the best tensile properties and flowability.

2. The multiscale analysis model developed in this study is valid for the damage progression analysis of UACS laminates. Numerical results are in good agreement with those obtained from experiments. Discontinuous and non-uniform slits play a positive role in suppressing the delamination progression in the outside regions around the ends of discontinuous slits compared to the UACS laminates with continuous slit distribution.

3. The results obtained from the tensile experiment and FEM analysis for UACS laminates with different specimen width indicate that the specimen width has significant influence on the tensile strength but less influence on the tensile stiffness of the laminates.

Stress concentration at the free edge plays a main role in the effects of the specimen width on the delamination progression and the tensile strength of the UACS laminates.

5.2 Future work

This study investigated the tensile properties of UACS with different patterns slit distribution, however, other important mechanical properties such as compression, bending, fatigue and impact have not been studied. Further experimental research and numerical analysis are necessary for the development of practically useful UACS laminates in the future.

In addition, the flowability of UACS laminas with newly designed slit patterns was investigated in the form of plate, further study on the flowability of the UACS laminates in the fabrication of complex structural components is also necessary in the future.

LIST OF FIGURES

Figure 1-1: Overview of material application in the Boeing 787 and the Airbus A380.... 3

Figure 1-2: Window frame of the Boeing 787 [28]. 5

Figure 1-3: Schematic of the first UACS created by introducing slits in arrayed continuous fibers of prepreg. 7

Figure 1-4: Comparison of modulus and strength between SMC, the first UACS and conventional CFRP. 8

Figure 1-5: Comparison of cross-sections and fractured coupons of SMC, the first UACS and conventional CFRP [29]. 9

Figure 1-6: Compression moldings of a quasi-isotropic UACS stack into a flat plate laminate. 10

Figure 1-7: A T-shaped rib structure made from quasi-isotropic stacks of conventional prepreg (left) and the first UACS prepreg (right) [29]. 11

Figure 1-8: Comparison of tensile modulus and strength of quasi-isotropic laminates including different toughened interlaminar layers. 14

Figure 1-9: Schematic diagram of UACS with interlaminar toughened layers only around the slits. 15

Figure 1-10: Comparison of tensile modulus and strength of quasi-isotropic laminates with different areas of toughened layers. 16

Figure 1-11: Schematic diagram of UACS by introducing continuous angled slits in prepreg. 17

Figure 1-12: Schematic diagram of stress distribution around an continuous angled slit in the 0° ply..... 18

Figure 1-13: Relation between tensile strength of quasi-isotropic UACS laminates and the slit angle. 19

Figure 2-1: Schematic diagram of cutting procedures for fabricating a bi-angled slit pattern UACS lamina. 30

Figure 2-2: Image of cutting process of slits by using a paper cutter. 30

Figure 2-3: Newly designed discontinuous angled slit patterns and the existing continuous angled slit pattern. 32

Figure 2-4: Slits distribution in staggered and bi-angled pattern UACS plies when L_x = 10 mm. 33

Figure 2-5: Schematic of stacking a laminate by UACS plies with discontinuous bi-angled slits. 34

Figure 2-6: Photograph of the autoclave used for curing the UACS laminates. 35

Figure 2-7: Cure cycle recommended by the manufacture of the CFRP prepreg..... 36

Figure 2-8: Typical optical micrograph of slits cut using a paper cutter. 37

Figure 2-9: Typical images of slits in a cured UACS laminate with continuous angled slits. 37

Figure 2-10: Geometry of the specimens for tensile test. 38

Figure 2-11: MTS 810 material-testing system used in the tensile tests of UACS laminates. 40

Figure 2-12: Typical stress-strain curves of cured UACS laminate with various slit patterns. 41

Figure 2-13: Tensile modulus of various quasi-isotropic laminates. 42

Figure 2-14: Tensile strength of various quasi-isotropic laminates. 43

Figure 2-15: Typical images of fractured specimens of various quasi-isotropic laminates. 44

Figure 2-16: Cross-section images of continuous slit pattern UACS laminate at the load level of 90% of the laminate strength. 45

Figure 2-17: Cross-section images of various UACS laminates after tensile test at the load level of 95% of the laminate strength. 46

Figure 2-18: Schematic of damage progress for UACS laminates under tension. 47

Figure 2-19: Slits distributions of 0° plies and adjacent 45° plies in various UACS laminates. 48

Figure 2-20: Influence of slit length on the tensile properties of laminates with two new slit patterns. 49

Figure 2-21: Stacking schematic of hybrid laminate (first and third plies: glass-fiber plies; second ply: bi-angled slit pattern UACS ply). 51

Figure 2-22: Photograph of mini hot-pressing equipment used in flowability test of UACS laminas. 52

Figure 2-23: Images of three [90/0/90] hybrid laminates after cure. 54

Figure 3-1: A multiscale FEM model for the UACS laminate with bi-angled slits. 60

Figure 3-2: Illustration of the distribution of slits in the top four plies of the multiscale model for the UACS laminates. 62

Figure 3-3: Illustration of an elasticity problem of a material with periodic microstructures. 64

Figure 3-4: A rectangular parallelepiped unit cell. 68

Figure 3-5: FEM meshes of three representative volume cells for the three kinds of UACS laminas in progressive damage analysis..... 75

Figure 3-6: FEM meshes of UACS laminate with bi-angled slit distribution in different length scales. 78

Figure 3-7: Illustration of eight-node cohesive elements. 80

Figure 3-8: Three standard traction/displacement mode: Bilinear (left), Exponential (middle), and linear exponential (right) 81

Figure 3-9: Characteristics of constitutive relations (Bilinear). 82

Figure 3-10: Flowchart of the multiscale FEM analysis..... 86

Figure 3-11: Longitudinal modulus of various quasi-isotropic laminates without or with slits obtained from homogenization analysis and the previous experimental results. 87

Figure 3-12: Influence of mesh size on the calculation results..... 89

Figure 3-13: tensile strength results obtained from symmetrical and asymmetrical models of UACS laminate with bi-angled slit distribution..... 90

Figure 3-14: Load-tensile damage (*FI*1) curves of the slits in 0° plies of the three kinds of UACS laminates..... 92

Figure 3-15: Tensile damage images of the slits in 0° plies of the three kinds of UACS laminates at 16.2 kN..... 92

Figure 3-16: Variation of stress distribution in a typical slit in 0° ply of the UACS laminate with bi-angled slit distribution due to the reduction of stiffness after the tensile failure occurs in the slit.. 93

Figure 3-17: Typical load-damage (*d*) curves of the interface 1 between 45°and 0° plies of the three kinds of UACS laminates. 94

Figure 3-18: Typical damage (*d*) images in the interface 1 of the UACS laminate with bi-angled slit distribution at 34.3 kN. 96

Figure 3-19: Typical images of delamination growth in the interface 1 of the three kinds of UACS laminates with the increase of the load. 96

Figure 3-20: Typical images of tensile damage parameter (*FI*1) in 0° ply for the three kinds of UACS laminates at or near their maximum loads. 97

Figure 3-21: Typical stress-strain curves obtained from FEM analysis and the previous experiments. 98

Figure 3-22: Comparison of experimental tensile strength with damage progression analysis for various UACS quasi-isotropic laminates. 99

Figure 3-23: Comparison of experimental final strain strength with damage progression analysis for various UACS quasi-isotropic laminates. 100

Figure 4-1: Schematic of tensile specimens with different widths. 109

Figure 4-2: Tensile strength of UACS laminates with different widths. 110

Figure 4-3: Typical stress-strain curves of bi-angled slit distribution UACS laminate with different width. 112

Figure 4-4: Typical images of fractured specimens of bi-angled slit distribution UACS laminates with different widths. 114

Figure 4-5: Cross-section images of a specimen with bi-angled slits and with 40 mm in width after tension. 115

Figure 4-6: The multiscale FEM model of B15 for damage progression analysis. 117

Figure 4-7: Variation of tensile failure index *FI*1 in the slits of the 0° plies of bi-angled slit distribution UACS laminates with different widths. 119

Figure 4-8: Typical images of tensile failure index *FI*1 in the 0° ply of B20 under the stress level of 192.05 MPa. 121

Figure 4-9: Typical stress-damage (*d*) curves of the interface 1 in various damage progression analysis models for UACS laminates with bi-angled slit distribution. 122

Figure 4-10: Comparison of damage images (*d*) for interface 1 in B10, B20 and B40 under different load levels. 123

Figure 4-11: The strain-delamination proportion curves of the interface 1in B10, B20 and B40. 124

Figure 4-12: Typical strain-damage (*d*) curves of the representative elements in interface 1 of B40..... 125

Figure 4-13: Comparison of strain-delamination proportion in interface 1 and interface 2 in B40..... 126

Figure 4-14: Typical images of the failure index *FI*1 in the 0° ply of B40 at the stress level of 513.1 MPa. 127

Figure 4-15: Typical stress-stain curves obtained from FEM analysis of B10 to B40.. 128

LIST OF TABLES

Table 2-1: Specimens used for tensile tests. 39

Table 3-1: Material properties of the CFRP and the epoxy resin. 61

Table 3-2: Material properties of the cohesive element..... 84

Table 3-3: Critical loads for various failure modes occurring in the three kinds of UACS laminates..... 91

Table 3-4: Results of the strength and failure strain of the three kinds of UACS laminates obtained from the multiscale FEM analysis and previous experiments. 99

Table 4-1: Strength and longitudinal modulus of UACS laminate with bi-angled slits distribution and with different widths..... 112

Table 4-2: Critical stresses for various failure modes occurrence in bi-angled slit distribution UACS laminates. 120

Table 4-3: Results of the strength obtained from the multiscale analysis and experiments. 129

LIST OF PUBLICATIONS

This dissertation is written based on the following publications:

[1] Hang Li, Wen-Xue Wang, Yoshihiro Takao, Terutake Matsubara. New designs of unidirectionally arrayed chopped strands by introducing discontinuous angled slits into prepreg. *Composites Part A: Applied Science and Manufacturing*, 2013, 45(2): 127-133.

[2] Hang Li, Wen-Xue Wang, Terutake Matsubara. Multiscale analysis of damage progression in newly designed UACS laminates. *Composites Part A: Applied Science and Manufacturing*, 2014, 57(2): 108-117.

[3] Hang Li, Wen-Xue Wang, Terutake Matsubara. Damage progression in unidirectionally arrayed chopped strands laminates with different slit patterns under tension. *Advanced Materials Research*, 2013, 704: 307-312.

[4] Hang Li, Wen-Xue Wang, Yoshihiro Takao, Terutake Matsubara. Effects of slit patterns on the tensile properties of unidirectionally arrayed chopped strands composites. *Materials Science Forum*, 2013, 750: 208-211.

[5] Hang Li, Wen-Xue Wang, Yoshihiro Takao, Terutake Matsubara. Mechanical properties of unidirectionally arrayed chopped strands (UACS) with different slit patterns. *Proceedings of the 18th International Conference on Composite Materials (ICCM18),* Jeju, Korea, 2011.

[6] Hang Li, Wen-Xue Wang, Terutake Matsubara. Damage progress in newly designed UACS laminates. *Proceedings of the 9th Japan-Korea-Joint Conference on Composite Materials (JK9)*. Kagoshima, Japan, 2013.

[7] Wen-Xue Wang, Hang Li, Terutake Matsubara. New unidirectionally arrayed chopped strands composites by introducing discontinuous angled slits into prepreg. *Proceedings of the 15th European Conference on Composite Materials (ECCM15)*. Venice, Italy, 2012.

ACKNOWLEDGEMENTS

The present study was carried out at Kyushu University during the years 2010-2013. I would like to express my gratitude to all those who helped me during the research and writing of this dissertation.

My deepest gratitude goes first and foremost to my supervisor, Professor Wen-Xue Wang, not only for accepting me as a doctor candidate to study at Kyushu University, but also for his constant encouragement and inexhaustible instruction from life details to my work. His wide knowledge and energy have injected tremendous value to the study, and without his consistent and illuminating instruction, this dissertation could not have reached its present form.

My warmest gratitude should be given to Professor Yoshihiro Takao, for his insightful advice and generous guidance throughout my study in Japan. I also would like to give my truly thanks to Mr. Terutake Matsubara, for his technical supports to the experiment on present study and kindly help during these years in Japan. My grateful heart extends to the other members of our laboratory as well, for their cooperation to my study and friendship to my life.

My great gratitude also goes to the committee members of my dissertation for helpful suggestions and commendations during the reviewing.

My acknowledgement with appreciation is to go to China Scholarship Council for the financial support and to the Northwestern Polytechnical University for providing me such an opportunity to study in Japan.

My last gratitude would go to my beloved family for their loving considerations and great confidence in me all through these years.